1627

Institut de physique
Université de Neuchâtel

Quantum cascade structures based on photon-assisted tunneling transitions in strong magnetic fields

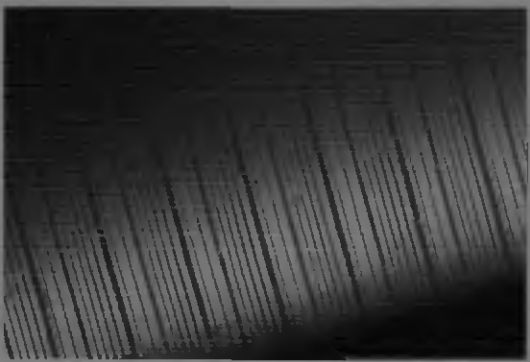

THESE

présentée à la Faculté des Sciences de l'Université de Neuchâtel
pour obtenir le grade de docteur ès sciences

par

Stéphane Blaser

Neuchâtel, février 2002

Institut de physique
Université de Neuchâtel

Quantum cascade structures based on photon-assisted tunneling transitions in strong magnetic fields

THESE

présentée à la Faculté des Sciences de l'Université de Neuchâtel
pour obtenir le grade de docteur ès sciences

par

Stéphane Blaser

Neuchâtel, février 2002

IMPRIMATUR POUR LA THESE

Quantum cascade structures based on photon-assisted tunneling transitions in strong magnetic fields

de M. Stéphane Blaser

UNIVERSITE DE NEUCHATEL

FACULTE DES SCIENCES

La Faculté des sciences de l'Université de Neuchâtel sur le rapport des membres du jury,

MM. J. Faist (directeur de thèse), P. Martinoli,
R. Houdré (EPF Lausanne) et
U. Gennser (Paris)

autorise l'impression de la présente thèse.

Neuchâtel, le 17 avril 2002

Le doyen:

F. Zwahlen

A ma maman
et
à mon papa

Abstract

This work consists of a study on quantum cascade lasers under the influence of strong magnetic fields. In particular, we studied structures based on the so-called photon-assisted tunneling (or diagonal) transition. These intersubband lasers are optical sources emitting in the mid-infrared (between 3 and 25 μm), and, as recently demonstrated, in the far-infrared (about 70 μm). Both experimental and theoretical aspects are investigated in this thesis, leading to new results.

Quantum cascade lasers differ in fundamental ways from semiconductor diode lasers such as those being used in CD players: (i) the electronic transitions occur between subbands involving only one type of carriers, the electrons; (ii) they use a multistage cascaded structure allowing each electron to generate many photons; (iii) their emission wavelength is not an intrinsic property of the material used, but can be tailored by changing the thicknesses of the different epitaxial layers. Due to their various particularities, these lasers have very interesting applications. As most of molecular gases have their fundamental vibrational modes in the mid-infrared, the quantum cascade lasers are particularly useful for gas sensing. Since the atmosphere has two transparent regions just at the wavelengths where the quantum cascade lasers emit efficiently, they have also important applications for free-space optical data transmission (telecom).

From a physical point of view, there are still many intersting fields to explore. As the photon-assisted tunneling transition is sort of a two-level system, a model is derived for the injection and extraction processes of the electrons. In particular, the transport measurements and the behaviour of the threshold current as a function of the temperature are computed and compared to the experiments. This work alllowed to deduce an escape tunneling time which

lead to the development of new lasers with very high performance.

Photon-assisted tunneling transitions were also studied in the far-infrared with the demonstration of electroluminescence from these structures.

The simulation of a quantum box laser by applying a strong magnetic field on these structures is also an important subject of this work. Indeed, by applying a magnetic field perpendicularly to the layers, the quantum-mechanical dimensionality decreases. In the mid-infrared the lifetime is controlled by optical phonon emission. The quantization of the system into Landau levels by the application of a magnetic field will quench the optical phonon emission, leading to a performance increase. In the far-infared, where we can reach a point where the intersubband transition energy is smaller than the cyclotron energy, luminescence intensity enhancement and lifetime increase were observed. These measurements in strong magnetic fields were performed in a cryostat containing a superconducting coil allowing to reach magnetic fields on the order of *14* Tesla (i.e. *100* larger than the magnetic field of a permanent magnet).

Résumé

Ce travail consiste en une étude des lasers à cascade quantiques sous l'effet de champs magnétiques intenses. Un accent a été particulièrement mis sur les structures basées sur une transition diagonale. Ces lasers intersousbandes sont des sources optiques qui émettent dans l'infrarouge moyen (entre 3 et 25 μm), ainsi que, depuis récemment, dans l'infrarouge lointain (autour de 70 μm). Tant les aspects théoriques que les aspects expérimentaux tournant autour de ces lasers sont abordés dans cette thèse et mènent à de nouveaux résultats.

Les lasers à cascade quantiques diffèrent de manière fondamentale des diodes lasers semiconductrices telles que celles se trouvant dans les lecteurs de CD: (i) les transitions électroniques ont lieu entre sousbandes impliquant un seul type de porteur, les électrons; (ii) ils utilisent une structure en cascade permettant à chaque électron d'émettre plusieurs photons; (iii) leur longueur d'onde d'émission n'est pas une propriété intrinsèque des matériaux utilisés, mais peut être fixée en choisissant judicieusement l'épaisseur des différentes couches épitaxiales. Par leur particularités diverses, ces lasers ont de très intéressantes applications. Comme la plupart des gaz molculaires ont leurs modes vibrationnels fondamentaux dans le moyen infrarouge, les lasers à cascade quantiques sont donc particulièrement utiles pour l'analyse de gaz. L'atmosphère ayant deux fenêtres de transparence dans ces longeurs d'onde, les lasers à cascade quantiques ont également d'importantes applications dans le domaine des télécommunications pour les transmissions optiques de données dans l'air sans avoir à recourir aux fibres optiques.

Du point de vue physique, il reste encore de nombreux domaines à explorer. Comme la transition diagonale est une sorte de système à deux niveaux, un modèle est dérivé pour les processus d'injection et d'extraction des électrons. En particulier les mesures de transport et

le comportement du courant de seuil en fonction de la température sont calculés et comparés avec les expériences. Ce travail a permis de déduire un temps d'effet-tunnel qui a conduit au développement de nouveaux lasers qui fonctionnent avec de très bonnes performances. Une telle transition diagonale a également été étudiée dans l'infrarouge lointain par la dmonstration de l'électroluminescence sortant de ces échantillons.

La simulation d'un laser à boîte quantique par l'application d'un champ magnétique intense sur ces structures est également un sujet important de ce travail. En effet, en appliquant un champ magnétique perpendiculairement aux couches, la dimensionnalité quantique diminue. Dans l'infrarouge moyen, le temps de vie est contrôlé par l'émission de phonons optiques. La quantification du système en niveaux de Landau par l'application d'un champ magnétique va diminuer l'émission de ces phonons optiques, augmentant ainsi les performances. Dans l'infrarouge lointain, où le cas où l'énergie de transition intersousbande est plus petite que l'énergie cyclotron peut être atteint, une augmentation de l'intensité lumineuse et une augmentation du temps de vie ont été observés. Ces mesures en champs magnétiques intenses ont été réalisées dans un cryostat contenant une bobine supraconductrice permettant d'obtenir des champs de l'ordre de 14 Tesla (100 fois plus grands que le champ magnétique d'un aimant permanent).

Contents

Abstract i

Résumé iii

List of figures ix

List of tables xi

1 Introduction 1
- 1.1 General introduction 1
- 1.2 Other infrared sources 4
- 1.3 Applications of quantum cascade lasers 6
  - 1.3.1 Gas sensing 6
  - 1.3.2 Telecommunications 7
  - 1.3.3 Terahertz sources 8
- 1.4 Scope and organization of this thesis 8

2 Theory 11
- 2.1 Introduction 11
- 2.2 Intersubband versus interband transitions 11
- 2.3 Superlattice heterostructures 14
- 2.4 Kazarinov and Suris proposal 15
- 2.5 Quantum cascade lasers 17
  - 2.5.1 Cascading scheme 17
  - 2.5.2 Active and injection regions, doping 17
  - 2.5.3 Lifetimes 20
- 2.6 Photon-assisted tunneling transition 23
- 2.7 Magnetic field 26
  - 2.7.1 Perpendicular magnetic field 29
  - 2.7.2 Parallel magnetic field 31

3 Experimental setup and sample fabrication 35
- 3.1 Magnetic field cryostat 35
- 3.2 Far-infrared insert 38

3.3 Hall probe 40
3.4 Growth 42
3.5 Processing 43
3.5.1 Mid-infrared structures 43
3.5.2 Far-infrared or terahertz structures 46

4 Mid-infrared quantum cascade lasers **49**
4.1 Photon-assisted tunneling transition-based QCL 49
4.1.1 Laser design and characterization 50
4.1.2 Rate equations 52
4.1.3 Lifetime ratio and condition for lasing 54
4.1.4 Comparison with experiment 56
4.1.5 Continuous-wave and spectral analysis 61
4.1.6 Waveguide losses 63
4.1.7 Electroluminescence and tuning 65
4.1.8 Conclusion 68
4.2 Measurements on a superlattice 71
4.2.1 Electroluminescence in a superlattice 72
4.2.2 Measuring gain in a superlattice 74
4.3 Superlattice in magnetic field 78
4.3.1 Motivation: superlattice laser 78
4.3.2 Magnetic field electroluminescence of a superlattice 79
4.4 Quantum cascade lasers in parallel magnetic field 80
4.4.1 Luminescence dependence of diagonal-based QC lasers 80
4.4.2 Dependence of the threshold current 84
4.5 Quantum cascade lasers in perpendicular magnetic field 85

5 Far-infrared quantum cascade structures **91**
5.1 Motivation for the magnetic field measurements 91
5.2 Vertical transition-based structures 94
5.2.1 Structures 94
5.2.2 Electroluminescence spectra in magnetic field 96
5.3 Superlattice structure 100
5.4 Diagonal transition-based structures 105
5.4.1 Three-quantum well diagonal structure 105
Optical measurements 106
Lifetime with B=0 108
Magneto-transport measurements 110
Intersubband Landau resonances 112
Comparison spectra-transport measurements 114
5.4.2 Five-quantum well diagonal structure 115
Structure 116
Electroluminescence spectra 116

6 Conclusions **121**

Acknowledgements **123**

Bibliography **125**

Appendix **139**

A Samples parameters **139**
A.1 Mid-infrared samples 139
A.2 Far-infrared samples 141

B Electronic states in quantum heterostructures **143**
B.1 Band structure calculations 143
B.2 Oscillator strength 145

C Population inversion engineering **147**
C.1 Character of the transition 147
C.2 Optical phonon resonance-based population inversion 149
C.3 Other lasing schemes 150

D Properties of the InSb detector **153**

Published work **155**

List of Figures

1.1 Progress in pulsed and continuous-wave lasing operation of QCL 2

2.1 Interband versus intersubband transitions 12
2.2 Kazarinov and Suris's superlattice 15
2.3 Cascade principle, active and injection regions 18
2.4 Intersubband relaxations in the far-infrared 22
2.5 Three quantum well and photon-assisted tunneling active regions 24
2.6 Principle of laser action in a diagonal transition 25
2.7 Magnetic field configuration 27
2.8 Dispersion relation in perpendicular magnetic field, Landau levels 30
2.9 Dispersion relation in parallel magnetic field, k-shift 32

3.1 Sample holder and lens mount for mid-infrared measurements 36
3.2 Magnetic cryostat with far-infrared insert 37
3.3 Photo of the InSb detector-mount 38
3.4 FIR electroluminescence setup 39
3.5 Hall measurements and shift in energy 41
3.6 TEM image of a QCL active region 43
3.7 Schematic drawings of laser stripe and mesa 45

4.1 Energy band diagram of laser S1548 51
4.2 L-I curves in pulsed mode of S1548 52
4.3 V-I and L-I curves from the model 55
4.4 Lower state lifetime vs. threshold current 57
4.5 Comparison of the V-I curves between model and experiment 59
4.6 Peak net modal gain derived by the model 60
4.7 Comparison of the threshold current density between model and experiment 60
4.8 L-I curves in continuous-wave of laser S1548 61
4.9 Fabry-Pérot spectrum for linewidth measurement 62
4.10 Peak net modal gain (Hakki-Paoli) measurements 64
4.11 Electroluminescence spectra of structure S1548 66
4.12 Tuning of laser S1548 67
4.13 Bound-to-continuum and double optical phonon resonance active regions 68
4.14 Energy band diagram of laser S2007 69
4.15 L-I and V-I curves in pulsed mode of laser S2007 70
4.16 Peak net modal gain derived by the model for laser S2007 71
4.17 Electroluminescence spectra of a superlattice 72

4.18 Stark-shift of the diagonal (interwell) transition in a superlattice 73
4.19 Schematic drawing of a laser stripe with the polished 45° angle facet 75
4.20 Experimental and theoretical luminescence from both the facet and the 45° 77
4.21 Dispersion relation of a superlattice laser in parallel magnetic field 78
4.22 Electroluminescence of a superlattice in parallel magnetic field 79
4.23 Luminescence spectra in parallel magnetic field of structure S1548 81
4.24 Peak integral vs. applied parallel magnetic field for structures S1548 and S1672 . . . 82
4.25 Luminescence spectra in parallel magnetic field of structure S1672 82
4.26 Theoretical luminescence in parallel magnetic field with disorder 84
4.27 Threshold current as a function of parallel magnetic field for various QCLs 85
4.28 Schematic drawing of a quantum box laser 86
4.29 $I_{th}(B)$ and $L(B)$ for the laser based on an anticrossed transition at 10 μm 88
4.30 $I_{th}(B)$ and $L(B)$ for the laser based on a diagonal transition at 6 μm 89
4.31 $I_{th}(B)$ and $L(B)$ for the laser S1548 based on a diagonal transition at 10 μm 90

5.1 Dispersion relations in a perpendicular magnetic field in the FIR 92
5.2 FIR vertical transition-based structures energy band diagrams 95
5.3 Electroluminescence spectra of both vertical transition-based structures 96
5.4 Light intensity and current (voltage) as a function of the magnetic field 98
5.5 Intersubband and cyclotron transition energies 99
5.6 Energy band diagram of the FIR-superlattice structure 100
5.7 Optical spectra of the FIR-superlattice 101
5.8 Current vs. magnetic field curves of the FIR-superlattice 102
5.9 Transition energies vs. voltage and active region of the FIR-superlattice 104
5.10 Energy band diagram of the diagonal transition-based structure S1443 106
5.11 Luminescence spectra 107
5.12 Transition energy vs. voltage 108
5.13 Light intensity and bias vs. current 109
5.14 Voltage vs. current as a function of the magnetic field 110
5.15 Lifetime vs. applied magnetic field 111
5.16 (B_p,V_p) points for S1443 112
5.17 (B_p,V_p) points for S1351 113
5.18 Comparison of V-I curves between five- and three-quantum well based structures . . 115
5.19 Energy band diagram of the five-well diagonal transition-based structure A2429 . . . 116
5.20 Electroluminescence spectra of the five-quantum well structure 117
5.21 I-B curves of the five-quantum well structure 118
5.22 Transition energies deduced from magneto-transport, spectra and calculations 119

C.1 Character of the vertical, anticrossed and diagonal transitions 148
C.2 Dispersion relation of a three-level structure 149
C.3 Three quantum well and two quantum well active regions 150
C.4 Other active regions 151

D.1 V-I curves of the InSb detector vs. magnetic field 154
D.2 Terahertz laser spectrum using the InSb detector 154

List of Tables

3.1 Waveguide layer structure 44

5.1 Identified intersubband Landau resonances by the results of linear fit 113

A.1 Layer sequence of the GaAs/AlGaAs mid-infrared sample 139
A.2 Layer sequence of InGaAs/InAlAs mid-infrared samples 140
A.3 Layer sequence of GaAs/AlGaAs far-infrared samples 141
A.4 Layer sequence of the InGaAs/InAlAs far-infrared sample 141

Chapter 1

Introduction

1.1 General introduction

The demonstration of the first intersubband lasers in the InGaAs/InAlAs material system, called the quantum cascade lasers (QCL), at AT&T Bell Laboratories in 1994 [1] represented a major breakthrough for mid-infrared (MIR) optical sources (from $\sim 3\mu m$ up to $\sim 25\mu m$). The quantum cascade laser differs in fundamental ways from semiconductor diode lasers: (i) it relies on electronic transitions between subbands involving only one type of carriers, the electrons; (ii) it uses a multistage cascaded structure allowing each electron to generate many photons; (iii) the non-radiative scattering lifetimes are determined by optical phonon emission and lie in the ps range. All these points will be discussed in detail in the following chapters.

As the matter of fact, the QCLs have shown room-temperature operation virtually across the whole mid-infrared region from 3.5 μm (using strain compensated InGaAs/InAlAs [2]) up to 16 μm (using InGaAs/InAlAs materials on InP [3]). The emission wavelength was even pushed up to 24 μm in a chirped superlattice at cryogenic temperatures [4].

The achievement of such a laser was possible because of the capabilities of quantum engineering of electronic energy states and wavefunctions using ultrathin layers of semiconductor compounds with different compositions [5]. Experimentally, the advent of the molecular beam epitaxy (MBE) allowed the growth of III-V heterostructures with sharp interfaces and excellent compositional control [6].

After the first achievement of lasing operation in QCL, the performances of these lasers kept on improving. The first room-temperature operation was performed in 1996 at Bell Laboratories [7]. The highest operating temperature of single mode QC lasers of 150 °C was achieved in 2001 at Neuchâtel University, while the record high temperature of 200°C was reached recently by the group of G. Abstreiter in Munich using the same active region design and high-reflection coating on both facets [8]. The application of the QC technology was also achieved using other material system such as GaAs/AlGaAs, in which laser demonstration was obtained in 1998 [9] and room-temperature pulsed operation was reached in 2001 [10].

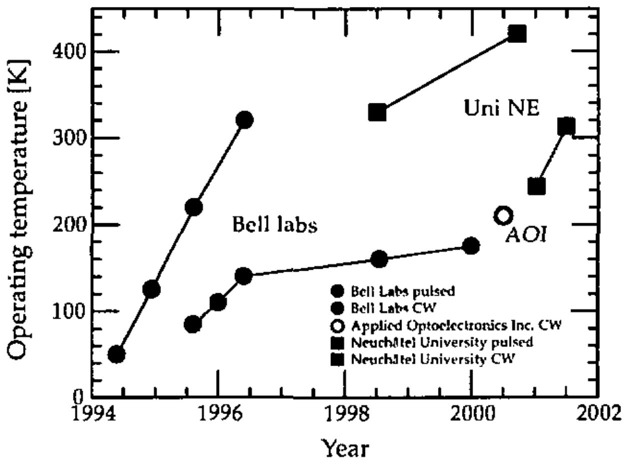

Figure 1.1: Operating temperature of quantum cascade lasers during the last years showing the progress achieved in pulsed and continuous-wave lasing operation.

Another important milestone for commercial applications is room-temperature operation in continuous-wave, which was recently achieved at Neuchâtel University [11]. The progress in operating temperature of quantum cascade lasers during the last years are shown in Fig. 1.1 for pulsed and continuous-wave operation. The research groups responsible for the different results are also indicated. In the mid-infrared range, the quantum cascade lasers are the best performing semiconductor lasers and are more powerful than competing interband laser diodes in both pulsed and continuous-wave operation.

It would be desirable to use the technology of the quantum cascade lasers in the far-infrared (FIR), or terahertz, range (for photon energies smaller than the optical phonon energy, i.e. $\lambda > 34\mu$m), where the lack of convenient sources is especially obvious. Intersubband electroluminescence was observed at Neuchâtel University in a vertical transition-based quantum cascade structure at $\lambda = 88\mu$m in GaAs/AlGaAs material system in 1998 [12], but with very low power. However, in the frame of an european project collaboration (WANTED), Köhler *et al.* [13] and our group in Neuchâtel [14] succeeded very recently in the realization of lasing operation in a chirped superlattice at $\lambda \sim 70\mu$m. This is a important step showing that the quantum cascade technology allows realization of laser sources in the complete infrared range, in the mid- as well as in the far-infrared.

A long-standing wish for microelectronics technology has been the integration of semiconductor lasers onto a silicon chip. Unfortunately, the indirect band gap of the group IV materials (in particular Si) is a hindrance to Si-based active optical components, implying that radiative transitions must be accompanied by a large momentum transfer. Using the quantum cascade technology, these problems can be circumvented, since transitions occur between subbands: the transitions occur without momentum transfer and the nature of the band gap is irrelevant. Electroluminescence in the 10 μm-range, with a narrow linewidth, was first demonstrated in the Si/SiGe material system by using the QC concept in 2000 [15]. Compared to the III-V QC lasers, the SiGe material system needs to work in the valence band with coupled heavy and light holes. This result constitutes a step towards establishing the feasibility of Si/SiGe-based QC lasers.

Thanks to an increasing interest in their applications, several groups are nowadays involved in the development of quantum cascade lasers. The main players include Bell Labs, Northwestern University, Shanghai Institute of Metallurgy for the InGaAs/InAlAs material system and Thales, TU-Vienna, University of Sheffield, University of Glasgow, Cavendish Laboratory at Cambridge for the GaAs/AlGaAs material system. University of Neuchâtel and the Walter Schottky Institute Munich are working with both material systems. The terahertz region is investigated by TU-Vienna, Bell Labs, Cavendish Laboratory at Cambridge, Quantum Institute at the University of California Santa Barbara, MIT at Cambridge (USA), the physics lab of the Scuola Normale Superiore in Pisa and University of Neuchâtel.

1.2 Other infrared sources

In the nineties, several types of mid- and far-infrared sources have emerged aside the achievement of the QCLs. The research in these fields has attracted numerous groups, for these lasers have potential applications in a wide range of applications from fiber-optics / free-space telecommunications, molecular spectroscopy, gas sensing as well as medical diagnostics. In this section, we present some of these other infrared sources.

A common mid-infrared laser is certainly the CO_2 laser, which operates around 10 μm. It is highly efficient and can produce 100 W in continuous-wave operation. Nevertheless, its relatively narrow spectral emission range (from 9.2 to 10.8 μm) and the discrete spectrum limit its application for gas spectroscopy. A different mid-infrared technology, which is used in some applications, is based on interband lead-salt diode lasers which have been demonstrated in a wide spectral range roughly from 3 to 30 μm. These lasers operate at room-temperature (with very low power) in pulsed mode approximatively up to 5 μm, but necessitate cryocoolers at longer wavelengths. In practical systems, these devices operate at low temperatures, and have low power. For a recent review on lead-salt lasers, see for example [16]. For emission between 1.9 and 3 μm, antimonide-based QW lasers have also demonstrated good performances, including continuous-wave operation at room-temperature at $\lambda \sim 2\mu$m [17].

The cascading scheme of the QC lasers (see Sec. 2.5) was also used in another type of semiconductor laser, namely the interband cascade (IC) laser, proposed by R. Q. Yang in 1995 [18]. This laser is based on optical transitions between the conduction and valence band in type-II quantum well structures, such that the fast non-radiative optical phonon scattering in intersubband QC lasers can be circumvented while retaining the advantages of cascaded injection and wavelength tailoring. Such a laser is based on InAs/(In)GaSb/(In)AlSb type-

II material system for the active region and comprises an injection region consisting of a digitally graded InAs/AlSb superlattice. Following the observation of mid-IR (3.6 - 3.8 μm) electroluminescence in these structures [19], the first type-II IC laser was demonstrated in 1997 [20]. The performances of such lasers are characterized by very low threshold currents (even in continuous-wave less than 100 A/cm^2 at nitrogen temperature), an output power exceeding 4 W/facet at 80 K, a peak power efficiency exceeding 9 % [21], and a slope efficiency of more than 780 mW/A, corresponding to a differential external quantum efficiency of 480 % [22]. However, the maximum operating temperature is still only 250 K in pulsed mode and 130 K in continuous-wave [21].

An alternate type of unipolar semiconductor laser relying on intersubband emission is the so-called quantum fountain (QF) laser which emits at $\lambda \sim 14.5 - 15.5 \mu$m based on optical excitation [23, 24], instead of electrical pumping. Here, the active region consists of periods of two GaAs/AlGaAs-coupled quantum wells exhibiting three bound electron states. The electrons are optically excited from the $n = 1$ ground state to the $n = 3$ upper state by a CO_2 laser. Although their operation imposes an external pumping source, QF lasers offer the advantages of a simplified design and of less stringent material requirements as compared to QC lasers. With no current flow, doping of the cladding layers and metal contacts are not necessary, which results in low internal losses at long wavelengths due to free-carrier absorption.

There are even fewer far-infrared sources available than mid-infrared sources. One is the free electron laser (FEL) which can generate tunable, coherent, high power radiation over a large part of the electro-magnetic spectrum. The FEL's operating characteristics are primarily determined by the type of accelerator that generates its electron beam. For example the FIR-FEL of the University of California in Santa Barbara can be tuned between 63 and 338 μm. The FEL is a device that converts the kinetic energy of free (unbound) electrons to electromagnetic radiation. Its main disadvantage is its huge size: it occupies an entire building.

Another alternative to achieve far-infrared sources is to take advantage of intersubband transitions in semiconductors. By using transitions between Landau levels if a magnetic field is applied (as discussed in this thesis, but applied to quantum cascade structures) in bulk semiconductors, p-Ge lasers have been demonstrated more than a decade ago [25]. These lasers rely on crossed electric and magnetic fields as well as intersubband scattering between light- and and heavy-hole subbands or light-hole cyclotron resonances [26] to create an inverted hot hole distribution in the valence band of weakly p-doped Ge. They can be operated at wavelengths between 70 and 300 μm and are tunable by changing either the magnetic field or the electric field. Unfortunately, they require temperatures below 10 K and a magnetic field of a few Tesla for operation and do not have continuous-wave operation.

1.3 Applications of quantum cascade lasers

1.3.1 Gas sensing

Most molecular gases have their fundamental vibrational modes in the mid-infrared region spanning approximately from 3 to 15 μm. These vibrational lines are very strong, allowing very sensitive chemical detection to be performed, with sensitivities down to below part per billion. Quantum cascade lasers are particularly useful for such gas sensing applications and in particular in the two so-called atmospheric windows lying between approximately 3-5 μm and 8-12 μm. The high transparency of the atmosphere in these two windows allows precise remote sensing and detection.

One of the detection techniques for gas-sensing is photoacoustic spectroscopy [27, 28]. In this technique, the optical beam of the laser is periodically amplitude modulated before illuminating the cell containing the absorbing chemical. Through periodic absorption, the gas in the photoacoustic cell expands periodically; this creates an acoustic wave which is detected by a conventional microphone. The signal can be greatly increased when working at a resonance frequency of the photoacoustic cell. The two very important advantages of photoacoustic detection are: i) it gives a positive signal (i.e. there is a signal only if the gas is present) and ii) it does not require a cooled mid-IR detector. The ultimate sensitivity is usually limited by the optical power of the source.

Another detection technique is a direct absorption measurement. The change in intensity of a beam is recorded as the latter crosses a sampling cell containing the chemical to be detected. This measurement technique has the advantage of simplicity [29, 30]. A more sophisticated version of this technique is the frequency modulation technique (TILDAS). The frequency of the laser is modulated sinusoidally so as to be periodically in and out of the absorption peak of the chemical. The absorption in the cell will convert this FM modulation into an AM modulation which is then detected usually by a lock-in technique. The main advantage of the TILDAS technique is its sensitivity. First of all, under good modulation conditions, an AC signal on the detector is present only if there is absorption in the chemical cell. Secondly, this signal discriminates efficiently against slowly varying absorption backgrounds. For this reason, this technique usually works well for narrow absorption lines, requiring also a monomode emission from the laser itself. This technique has already been successfully applied with distributed feedback QC lasers (DFB-QCL) [31].
Another ultrahigh-sensitivity trace-gas analysis is cavity ringdown spectroscopy, which is based on detecting the rate of decay of light exiting a high-finesse optical resonator. The application of this technique with ammonia was recently demonstrated by using a continuous-wave DFB QC laser [32].

1.3.2 Telecommunications

Further important applications for high performance quantum cascade lasers are in the field of free-space optical data transmission [33]. In contrast to fiber optical telecommunications, this technique has the advantage of not requiring additional cables to be buried in the ground. Such a fast free-space optical data link could be particularly convenient in urban areas. QC lasers in the atmospheric windows around 5 and 10 μm are very suitable for such applications. Moreover, the fast internal lifetimes of the devices should allow modulation at frequencies of several hundreds of gigahertz and possibly up to ~ 1 THz assuming negligible parasitics [33, 34]. This modulation bandwidth is more than one order of magnitude greater than that of the fastest diode lasers. Recently, Martini *et al.* published results of an optical data link using a high-speed modulated, liquid nitrogen-cooled QC laser over a distance of

70 m under laboratory conditions [35]. They also succeeded in transmitting a video image via a common TV channel frequency. We demonstrated an optical data link between two different buildings separated by ~ 350 m and using a Peltier-cooled QC laser as well as a room-temperature HgCdTe detector, taking full advantage of the existing technology [36]. The shortest transmitted pulses measured 1.5 ns in duration and the highest transmitted modulation frequency was 330 MHz. We could also test the link under foggy conditions (with a visibility range of below 100 m) and the signal dropped to ~ 80 % of its initial value, which proves that atmospheric transmission at a wavelength around 10 μm is not adversely affected by humidity. We also used the QC laser to optically transmit data between two computers over a distance of 10 m between two optical tables. In such a configuration we achieved a data rate of 115 kbit/s using the serial port of the computers. When the laser power was decreased, the link still worked successfully down to a measured signal-to-noise ratio of 3.

1.3.3 Terahertz sources

There are many possible applications for compact, convenient solid-state sources such as far-infrared quantum cascade lasers operating at terahertz frequencies. Areas of special interest include wireless communications for local areas, space-based communications, medical imaging, gas or plastic components spectrometry or even security screening.

1.4 Scope and organization of this thesis

As shown, there are many applications using quantum cascade lasers. Hence, improving their performance remains a continuous challenge. From a physical point of view, there are still many interesting fields to explore. This thesis is mainly devoted to the so-called photon-assisted tunneling transition which is at the base of one of the various existing active regions which have shown lasing operation in the mid-infrared, but which reaches threshold by oscillator strength tuning. Such a transition allows therefore by its first-order Stark-shift a wide tunability range. The population inversion solely relies on tunneling. As such, it can also be used in the far-infrared or with non-polar materials (as for example Si-Ge alloys) where resonant optical phonon scattering cannot be implemented. As the photon-assisted tunneling transition is sort of a two-level system, it is a "model system" which allows to model the injection and extraction processes. In particular, the transport (voltage vs. current) characteristics, as well as the threshold current as a function of the temperature, can be computed and compared to the experiments. Taking into account a finite non-zero lower state lifetime, we were able to deduce an escape tunneling time which is much longer than thought up to now. The understanding of this effect allowed the realization of new active regions which have performed extremely well. We have also investigated such photon-assisted tunneling transitions in the far-infrared with the demonstration of electroluminescence from these structures.

An other important subject investigated during this work is the simulation of a quantum box laser. By applying a strong magnetic field perpendicularly to the layers, the quantum-mechanical dimensionality can be decreased. In the mid-infrared, the lifetime of the upper state is controlled by optical phonon emission. The application of a magnetic field is expected to quantize the system into Landau levels and to quench optical phonon emission, leading to a performance increase. In the far-infrared, where we can reach the point where the intersubband transition energy is smaller than the cyclotron energy, luminescence intensity enhancement and lifetime increase were observed.

This thesis is organized as follows. We start in Chapter 2 with a few theoretical aspects concerning the quantum cascade laser by presenting the main fundamental characteristics of these lasers. We will focus on the photon-assisted tunneling transition-based design. The effects of a magnetic field applied either perpendicularly or parallel to the layers are discussed theoretically. The experimental setup for mid-infrared and far-infrared measurements is described in Chapter 3, as well as the growth and processing techniques. The results concerning mid-infrared quantum cascade lasers are presented in Chapter 4, in particular measurements performed on lasers based on photon-assisted tunneling transition, including the modeling of this type of laser. Measurements performed on a superlattice with mid-infrared electroluminescence will be presented as well as measurements in parallel magnetic field. The last parts of this chapter are devoted to the investigations of the effects of parallel and perpendicular magnetic fields on various quantum cascade lasers. Chapter 5 addresses experimental measurements performed on far-infrared quantum cascade structures based on vertical as well as diagonal (photon-assisted tunneling) transitions. Chapter 6 will summarize the main results obtained in this work and suggest some future possibilities of investigations. Finally, a review of the parameters of the samples measured during this thesis is presented in Appendix A, the band-structure calculations in Appendix B, the population inversion engineering of the laser transition with a review of working devices using different designs in Appendix C, and the properties of the InSb detector used during far-infrared electroluminescence measurements in Appendix D.

Chapter 2

Theory

2.1 Introduction

This chapter summarizes a few theoretical aspects necessary for the understanding of the experimental work performed along this thesis. It begins with the discussion of one important feature of the quantum cascade laser, the intersubband transitions, followed by an introduction to superlattice heterostructures. The first proposal of intersubband emitters of Kazarinov and Suris is then presented. The next section, devoted to the quantum cascade laser itself, presents the theoretical framework concerning laser operation as well as the cascading scheme, the design philosophy and the lifetimes involved in intersubband transitions. The photon-assisted tunneling transition-based design is then described in detail. In the last section of the chapter, the effects of a magnetic field applied on the structures both perpendicular to the layers as well as parallel to the layers are discussed.

2.2 Intersubband versus interband transitions

In solid-state and gas lasers, the optical transitions occur between two discrete energy levels, the population inversion being achieved by optical or electrical pumping. For example the ruby ($\lambda = 0.6943\mu$m) or He-Ne ($\lambda = 0.63\mu$m) lasers emit in the red and the argon laser principally in the blue and green (between 0.488 μm et 0.514 μm). In contrast, conventional semiconductor diodes lasers, including quantum well lasers, rely on transitions between energy bands. The lasers used in CD, DVD or for telecommunications belong to this category. These so-called interband transitions occur then between energy bands in which conduction band electrons and valence band holes, injected into the active layer through a forward-biased $p-n$ junction, recombine radiatively across the band gap. The band gap essentially determines the emission wavelength, as shown in Fig. 2.1 a). In addition, the gain spectrum is quite broad due to the fact that the electron and hole populations are broadly distributed in the conduction and valence bands according to the Fermi's statistics. This gain is limited for these interband transitions by the joint density of states and saturates when the electron and hole quasi-Fermi levels are well within the conduction and valence bands, respectively. The resulting radiative lifetime is relatively long: about 1 ns.

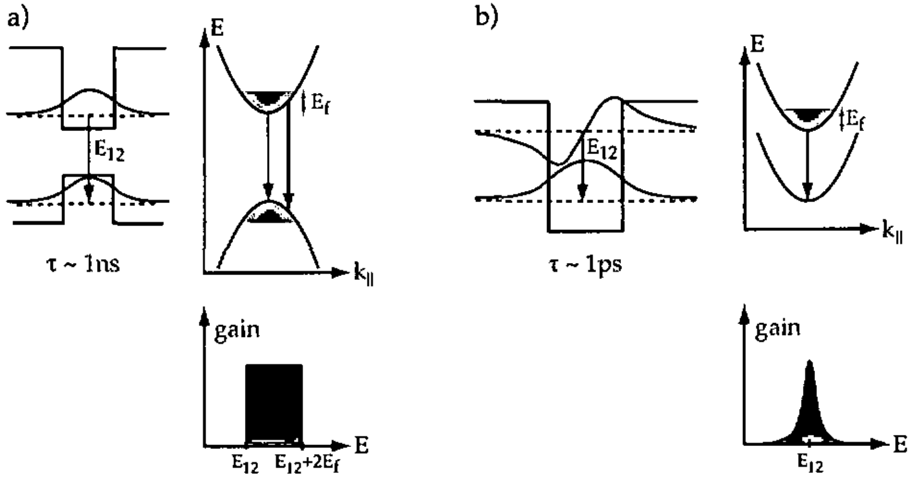

Figure 2.1: Real space band diagram, dispersion of the electronic subbands in k-space and joint density of state for a) interband and b) intersubband transitions.

The device studied during this thesis is a real new semiconductor light emitter. Indeed the unipolar intersubband laser or quantum cascade laser differs in many fundamental ways from conventional diode lasers. The main feature of the quantum cascade laser is its unipolarity:

it relies on only one type of carriers, the electrons. The unipolarity is relied to the nature of the optical transitions that occur here between conduction band states (subbands) arising from size quantization in a semiconductor heterostructure. These transitions are called intersubband transitions. As shown in Fig. 2.1 b), the initial and final states of the intersubband transitions are both in the conduction band and therefore have the same curvature in the reciprocal space, i.e. if one neglects the non-parabolicity, the joint density of states is very sharp like for atomic transitions (Fig. 2.1 b) bottom). In contrast to interband transitions, the gain linewidth is now indirectly dependent on temperature through collision processes and many body effects. Moreover, the intersubband gain is only limited by the amount of current one is able to drive in the structure to sustain population inversion. The intersubband devices are also less sensitive to the temperature than interband devices. The dominant intersubband scattering mechanism is optical phonon emission (for a subband spacing larger than the optical phonon energy) which leads to a very short intersubband lifetime, typically 1 ps.

The emission wavelength of a quantum cascade laser is not an intrinsic property of the semiconductors used, as in conventional semiconductor diode lasers, but can be tailored by changing the thicknesses of the different epitaxial layers. Using for example the InGaAs/InAlAs material system, it can be tuned over a wide range of wavelength: between $\lambda \sim 3.4\mu m$ [2] and $\lambda \sim 24\mu m$ [4]. Moreover the population inversion is not caused by some intrinsic physical property of the system, but must be designed by a suitable engineering of the wavefunctions. Ultimately, the largest photon energy is fixed by the conduction band discontinuity which is $\Delta E_c = 0.52$ eV in $In_{0.53}Ga_{0.47}As/In_{0.52}Al_{0.48}As$ lattice matched material system, but is only $\Delta E_c = 0.295$ eV in $GaAs/Al_{0.33}Ga_{0.67}As$ material system. On the long wavelength side, there are no fundamental limits preventing the fabrication of quantum cascade devices emitting in the far-infrared (or terahertz region). Until now terahertz lasing operation was only demonstrated in a chirped superlattice. Between these two wavelength ranges, there is a region where light cannot propagate, called *Reststrahlenband*, because the material is dispersive and heavily absorbing due to the interaction of the light with the optical phonons of the material (for InGaAs, this region takes place around 30 - 60 μm).

2.3 Superlattice heterostructures

In 1970, Esaki and Tsu considered theoretically a one-dimensional periodic potential, consisting of a periodic sequence of the same quantum well-barrier system, which they called superlattice, in monocrystalline semiconductors [37]. The superlattice, in term of multi-layers structure, is one of the basic concepts of the quantum cascade laser. It was the first proposal of quantum confinement with an heterostructure and opened new areas of investigation in the field of semiconductor physics. If no electric field is applied to the superlattice, the electron wavefunctions along the growth direction are described by delocalized Bloch functions. The formation of energy-bands and -gaps occurs in the same way as in a crystal. However, due to the larger period, the energy bands are much smaller (meV instead of eV) and therefore called minibands. The idea of Esaki and Tsu was to create minibands whose width can be changed by changing the thicknesses of the wells.

In the low field regime, defined by $eFd \leq \Delta$, where eFd is the field drop per period, Δ the miniband width, e the electron charge, F the external electric field and d the SL period, the miniband picture [37, 38] is employed theoretically to investigate the properties of the SL. At higher fields the semi-classical model has to be replaced by a quantum mechanical description. The miniband then splits into the Wannier-Stark (WS) ladder[39], that consists of a series of stationary states, each extending over a few periods and separated in energy by eFd. With increasing field the WS states localize until they are finally confined to single wells and resemble the quantum well ground states.

In a homogeneously biased SL, the current continuity requires the ground states in each well to be equally populated. Thus, no population inversion and, therefore, no net gain is expected from a diagonal interwell transition between adjacent ground states in a first approximation, i.e. without taking into account the Bloch gain. The original proposal of optical gain via photon-assisted tunneling for a strongly biased SL in which the ground state is lifted above the first excited of the adjacent well has been given by Kazarinov *et al.* [40, 41] as discussed in the next section.

2.4 Kazarinov and Suris proposal

In the early seventies Kazarinov and Suris predicted amplification of light in a strongly biased superlattice[40, 41]. This theoretical treatment based on a detailed density matrix analysis marks the basic idea of unipolar lasers based on intersubband transitions in semiconductor heterostructures.

If the electric field F applied to the superlattice satisfies $eFd > E_2 - E_1$, where d is the superlattice period and E_1 and E_2 are the energies of the ground state and the first excited state respectively, the ground state level in the n-th well is lifted above the first excited state level in the $(n+1)$-th well. In this situation (see Fig. 2.4) amplification may occur due to the possibility of tunneling of electrons from the ground state in the n-th well to the excited state in the $(n+1)$-th well accompanied by the simultaneous emission of a photon of energy $\varepsilon = eFd - (E_2 - E_1)$. Following non-radiative transitions from the excited to the ground state within one well the electrons are "recycled" for another photon-assisted tunneling process.

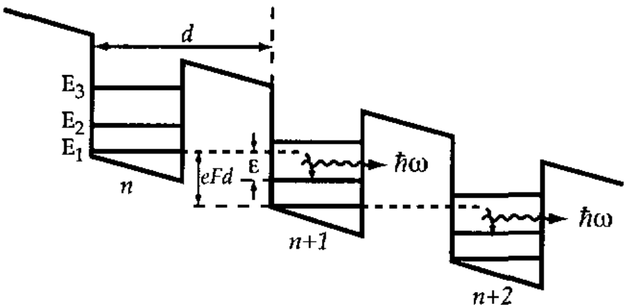

Figure 2.2: Schematic representation of the superlattice proposed by Kazarinov and Suris for far-infrared emission. The photon should be emitted during an interwell or diagonal photon-assisted tunneling transition between the ground state of the n-th well and the first excited state of the adjacent $(n+1)$-th well.

This sequence of photon-assisted tunneling processes leads to amplification, provided the initial ground state is more populated than the final excited state of the adjacent well.

Population inversion is maintained if the lifetime of the ground state exceeds the lifetime of the excited state. The expected relatively long non-radiative lifetime of the ground state associated with a "diagonal" transition into the adjacent well compared to the short intrawell lifetime of the excited state favors this condition.

However, the simple picture neglects that electrical transport in superlattices inherently features negative differential resistance (NDR)[37, 42, 43], which leads to the formation of electric field domains and renders the structure non-stable. Regions of NDR occur whenever the structure is biased beyond current peaks due to resonant tunneling between states of adjacent wells. The point of operation of the Kazarinov and Suris proposal lies precisely in the NDR. This effect prevents to sustain a high current simultaneously with a correct alignment between the confined states. Nevertheless, this seminal work was on the basis of the large number of proposals for intersubband lasers.

Following the proposal of Kazarinov and Suris, an intense research in the field of intersubband physics started, particularly after the first observation of intersubband emission in a two-dimensional electron gas formed at the Si-SiO_2 interface in silicon metal-oxide-semiconductor field-effect transistors (MOSFET) by Gornik and Tsui [44]. The first intersubband absorption in a GaAs-AlGaAs multi-quantum well was performed by West and Eglash in 1985 [45]. Experimental implementation of the proposal of Kazarinov and Suris led to the observation of spontaneous far-infrared intersubband luminescence from a GaAs-AlGaAs superlattice excited by sequential resonant tunneling by M. Helm in 1989 [46]. Diagonal (interwell) and vertical (intrawell) emissions in the mid-infrared has been reported by Scamarcio *et al.* [47] in a doped InGaAs/InAlAs superlattice.

Many theoretical proposals followed dealing with structures with resonant tunneling injection from the ground state of a quantum well into the first excited state of an adjacent quantum well [48, 49, 50], into a superlattice miniband [51] or into above-barrier quasi bound states [52]; the laser action should occur between the latter and the ground state, repeated through many wells. So far, it turned out to be too difficult to achieve population inversion using such tunneling schemes.

2.5 Quantum cascade lasers

2.5.1 Cascading scheme

Another fundamental feature of the intersubband quantum cascade laser is its multistage cascade scheme (electron recycling), where electrons are recycled from period to period, contributing each time to the gain and photon emission, as shown schematically in Fig. 2.3 a). In a ideal case, each electron injected above threshold will generate the same number of photons N as the number of period N, leading to a differential efficiency and then also optical power proportional to N. Gmachl *et al.* [53] have made modeling and an experimental study of the cascading behavior of quantum cascade lasers as a function of the number of stacked active regions (periods), including the first non-cascading (with only one active region) intersubband laser [54]. In particular, they confirmed the cascading scheme manifested in a differential slope efficiency effectively proportional to N.

2.5.2 Active and injection regions, doping

Figure 2.3 b) shows schematically one stage or period of a quantum cascade structure, which consists of an active region followed by a relaxation-injection region. The active region is the region where population inversion and gain takes place. It comprises usually an energy ladder of three states engineered in such a manner to maintain the population inversion between the two highest energy states. Assuming a simplified model without non-parabolicity (atomic picture) and a 100 % injection efficiency in the $n = 3$ state, the population inversion condition is $\tau_{32} > \tau_2$, where τ_{32}^{-1} is the non-radiative scattering rate from level 3 to level 2 and τ_2^{-1} is the total scattering rate out of level 2. The non-radiative channel 3-1 is usually not negligible and, therefore, this condition on the lifetime is less stringent than the condition $\tau_3 > \tau_2$ between the total lifetimes of states $n = 3$ and $n = 2$. Moreover, the lifetime τ_2 is principally determined by the scattering rate τ_{21}^{-1} to the lower subband $n = 1$. This ladder of states can be obtained in a variety of multi-quantum well structures (see Appendix C).

The relaxation-injection region is the section of the period where the electrons cool down

($T_e \sim T_l$, where T_e and T_l are the electronic temperature and the temperature of the lattice respectively) and are reinjected in the next period (see Fig 2.3 b). The structure must also be doped to overcome the breaking into different electric field domains observed in undoped superlattices (as in the proposal of Kazarinov and Suris [40, 41]).

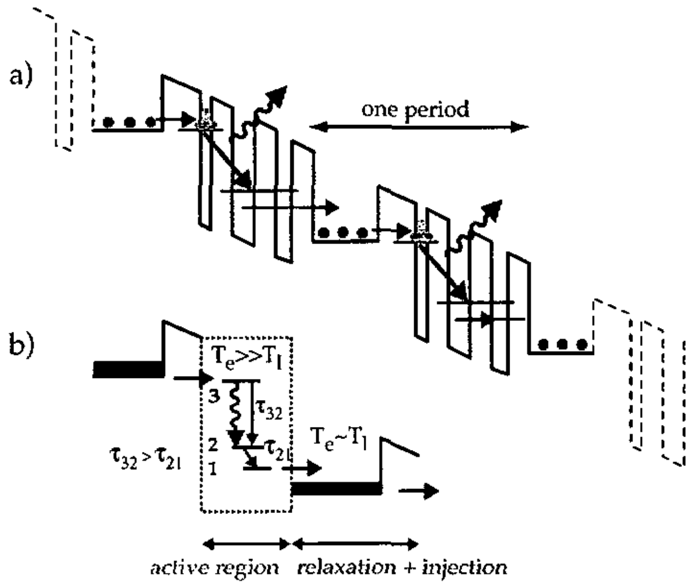

Figure 2.3: a) Principle of cascading: an electron cascades down emitting photons at each step. b) Quantum cascade design philosophy: each repeated period consists of an active (gain) region followed by a relaxation/injection region.

To obtain a laser structure, we need a homogenous and stable electric field distribution in the structure. Therefore by doping the structure, the integrated negative charge is always compensated by the fixed positive donors number even in the situation of strong injection to prevent space-charge formation. Moreover, the operating point of the laser must be a stable point of the current-voltage characteristic to prevent the breakdown of the active region into different field domains. Faist *et al.* have shown that electroluminescence spectra of intersubband transitions exhibit a band tail effect due to impurity disorder if the dopants are located in the active region [55]. Removing these dopants of the active region strongly reduces the electroluminescence linewidth. That is why the relaxation-injection region is doped. Experimentally, this doped region is restricted to the center of the injection region in order to have a modulation doping of the ground state of this injector, reducing the scattering and thus enhancing the injection efficiency.

The eigenvalues and the squared moduli of the wavefunctions, as well as the optical phonon emission lifetime, are computed numerically. This allows to optimize the different parameters as wells and barriers thicknesses or injector and active regions designs. The method of computation of these electronic states in quantum cascade structures is presented in Appendix B. To take into account the doping, we use a self-consistent approach. The total Hamiltonian is given by

$$H = -\frac{\hbar^2}{2m^*}\nabla^2 + V_{QC}(z) + V_H(z) \quad , \tag{2.5.1}$$

where $V_{QC}(z)$ is the confinement potential due to the quantum wells and $V_H(z)$ the Coulomb potential of screened impurities and electrons.

The charge density can be calculated by

$$q(z) = eN_D(z) - e\sum_i n_i|\phi_i(z)|^2 \quad , \tag{2.5.2}$$

where N_D is the doping profile of ionized dopants, $\phi_i(z)$ the probability density and n_i is the number of electrons per unit area in the i-subband. The Fermi energy E_F (calculated from the charge conservation condition) is obtained from

$$\sum_i n_i = \sum_i \int \rho_i(E)f(E)dE \quad \text{(electrons)} \tag{2.5.3}$$

$$= \int N_D(z)dz = n_s \quad \text{(impurities)} \tag{2.5.4}$$

where $\rho_i(E) = \frac{m_i^*}{\pi\hbar^2}\theta(E - E_i)$ is the density of states of the i-subband, $\theta(E - E_i)$ is the Heavyside function, $f(E) = \frac{1}{1+exp\left(\frac{E-E_F}{kT}\right)}$ is the Fermi distribution function, and n_s is the total areal electron concentration, which is equal to the impurities concentration. Inserting the charge density of Equ. 2.5.2 into Poisson's equation $\varepsilon\varepsilon_0\nabla_z^2\phi(z) = -q(z)$, one obtains

$$\frac{\partial^2\phi}{\partial z^2} = \frac{e}{\varepsilon\varepsilon_0}\left[\sum_i n_i|\phi_i(z)|^2 - N_D(z)\right] \quad . \tag{2.5.5}$$

The calculated new space charge potential $V_H(z) = e\phi(z)$ can be inserted in the Hamiltonian for the next iteration. Equation (2.5.5) and the Schrödinger equation must be solved iteratively. Both are coupled via space charge distribution of the electrons.

The electronic sheet carrier density per period n_s induced by the doping can be measured by capacitive measurements. In fact the doping can not be measured on samples based on InGaAs/InAlAs material system, because the Schottky barrier height on n-InGaAs is too low (~ 0.2 eV). But the barrier height is about 0.9 eV for GaAs/AlGaAs material system allowing C-V measurements. To create the Schottky barrier, the samples are etched to remove the highly doped top contacts layers above the active region and Ti/Au contacts are evaporated on it. The dependence of the capacity C on bias allows to determine the sheet density. Indeed the differential capacity can be written [56] as $C(V) = \frac{dQ}{dV} = \left(\frac{\varepsilon\varepsilon_0 e N_d}{2}\right)^{1/2} \cdot V^{-1/2}$. So the average density N_d as a function of the depletion length W is $N_d(W) = \frac{2}{\varepsilon\varepsilon_0 e}\frac{dV}{d(\frac{1}{C^2})}$, where ε is the dielectric constant and ε_0 the vacuum permittivity.

2.5.3 Lifetimes

As the population inversion between subbands in quantum cascade lasers does not come from an intrinsic property of the material but from quantum engineering, it is important to know and design the different scattering times involved in intersubband transitions. The dominant non-radiative scattering mechanism involved in intersubband transitions of more than an optical phonon energy (i.e. > 30 meV) is the emission of optical phonons. This process is very efficient and always allowed, so it gives lifetimes of the order of a picosecond. In comparison, the acoustical-phonon emission remains more than several hundred times less efficient at $T = 0$ K than the optical-phonon emission [57].

The computation of the optical phonon emission rate is thus important for the design of the structures. The lifetime τ_{if} of the heterostructure eigenstate is computed following Ferreira and Bastard [57] using the Fermi golden rule and the electron-phonon Hamiltonian, which contains the electron-optical phonon interaction (Frölich) term (earlier calculations were first described by Price [58, 59]). They showed that the non-radiative scattering rate from an initial state i to all final states f due to longitudinal-optical-phonon emission at $T = 0$ K is equal to

$$\frac{1}{\tau_{if}} = \frac{m^* e^2 \omega_{LO}}{2\hbar^2 \varepsilon_p} \int dz \int dz' \phi_i(z)\phi_f(z) e^{-q_{if}(z-z')} \phi_i(z')\phi_f(z') \tag{2.5.6}$$

where

$$q_{if} = \sqrt{\frac{2m^*(E_{if} - \hbar\omega_{LO})}{\hbar^2}} \tag{2.5.7}$$

is the momentum exchanged in the transition and $\varepsilon_p^{-1} = \varepsilon_\infty^{-1} - \varepsilon_s^{-1}$, where ε_∞ and ε_s are the high-frequency and static relative permittivity of the material. For GaAs, $\varepsilon_p = 70\varepsilon_0$ ($\varepsilon_\infty = 10.9\varepsilon_0$ and $\varepsilon_s = 12.91\varepsilon_0$) and for $In_{0.53}Ga_{0.47}As$, $\varepsilon_p = 72.2\varepsilon_0$ ($\varepsilon_\infty = 11.09\varepsilon_0$ and $\varepsilon_s = 13.1\varepsilon_0$) [60].

The transition rate for phonon emission at $T \neq 0$ is obtained by multiplying the zero-temperature result (Eq. 2.5.6) by $(1 + n)$, where n is the thermal population of optical phonons, according to the Bose-Einstein factor for stimulated absorption and emission of optical phonons

$$n = \frac{1}{e^{\frac{\hbar\omega_{LO}}{kT}} - 1} \quad . \tag{2.5.8}$$

The optical phonon-limited electron lifetime decreases then with increasing temperature; a property which is inherent to phonons in a single crystal. The performances of the quantum cascade laser (threshold current increase, slope efficiency decrease) are then strongly influenced by this property.

One of the most important consequences of these calculations is that the optical phonon emission becomes more efficient ($\tau \sim 0.25$ ps) if the subband spacing is equal to the optical phonon energy. This effect is used in the design of several structures to allow a fast electron escape from the lower state of the transition. The lifetime is also proportional to the overlap between the wave functions of the states involved in the transition (value of the integral in Equ. 2.5.6). That means that the lifetime of a vertical transition is of the order of 2 ps and could be more than 20 ps for a diagonal transition (see Appendix C), in which this overlap is smaller.

The physics of intersubband transitions in the far-infrared, when the energy between the two subbands is smaller then the optical phonon energy, is very different from the mid-infrared, because the scattering mechanisms are not anymore dominated by optical phonons emission. The Fig. 2.4 sketchs the relevant scattering processes for intersubband relaxation in this situation [61].

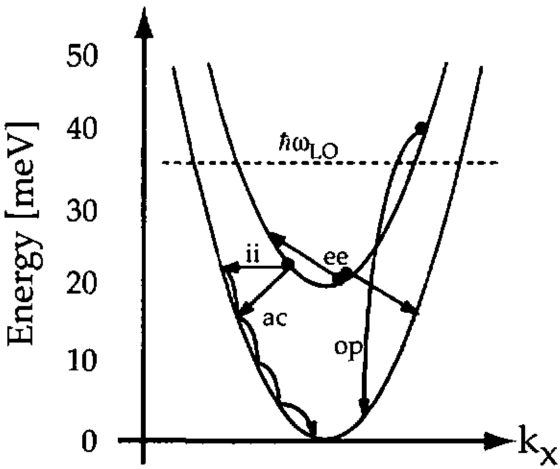

Figure 2.4: Schematic view of intersubband relaxation for the far-infrared, i.e. where the energy between the two subbands is smaller than the optical phonon energy. The main scattering mechanisms are electron-electron scattering (ee), acoustic-phonon emission (ac), ionized-impurity or interface roughness scattering (ii) and optical phonon emission (op).

At high temperature, the optical phonon emission keeps on playing the most important role, because the electrons can have enough excess energy to emit an optical phonon even if the intersubband energy separation is less than the optical phonon energy [62, 63, 64]. At low temperature the main scattering mechanisms are electron-electron scattering [65, 66, 67], ionized-impurity scattering and interface roughness [68, 69]. The electron-electron interaction varies with the square of the carrier density and becomes then important for large carrier density ($> 10^{10}$ cm^{-2}). Its corresponding scattering time is of the order of a picosecond. For very low densities ($< 10^{9}$ cm^{-2}), the intersubband scattering may be dominated by acoustic phonons [66].

The radiative rate for spontaneous photon emission τ_{rad}^{-1} for a two-level system with a transition energy $\hbar\omega$ is given by [70]

$$\tau_{rad}^{-1} = \frac{q^2\omega^3 n^3}{3\pi c^3 \hbar \varepsilon} z_{ij}^2 = \frac{q^2 n}{3\pi c^3 \varepsilon_0 \hbar^4} E_{ij}^3 z_{ij}^2 = \frac{4n\pi q^2}{3\varepsilon_0 c\hbar^2 \lambda^2} E_{ij} z_{ij}^2 \tag{2.5.9}$$

where $n = \sqrt{\varepsilon/\varepsilon_0}$ is the refractive index, q the electronic charge, c the light velocity, ε_0 the vacuum permittivity, E_{ij} the transition energy and z_{ij} the dipole matrix element B. The λ^2-dependence makes the radiative lifetime quite long at far-infrared wavelengths compared to the mid-infrared values (about 5 μs and 80 ns for a vertical transition in a square well of respectively 380 Å-width and 100 Å-width). The radiative efficiency for spontaneous emission is then given by

$$\eta_{rad} = \frac{\tau_{nr}}{\tau_{rad} + \tau_{nr}} \simeq \frac{\tau_{nr}}{\tau_{rad}} \tag{2.5.10}$$

where the non-radiative lifetime τ_{nr} is deduced from Eq. 2.5.6. This radiative efficiency is then on the order of 10^{-5} in the mid-infrared and 10^{-6} in the far-infrared.

2.6 Photon-assisted tunneling transition

As already mentioned, most results of this thesis are based on the photon-assisted tunneling (or diagonal) transition. This transition occurs across a barrier, the population inversion being mainly due to tunneling [71, 72, 73], without using an optical phonon resonance for the extraction, as in the first demonstrated so-called three-quantum well active region [1]. The typical active region of such a photon-assisted tunneling transition is shown in Fig. 2.5 in comparison with the three-quantum well active region. In fact, many different ways to achieve population inversion between subbands have already been demonstrated. They can be distinguished by the character of their 3-2 transition (see Fig. 2.3 b). A discussion about the population inversion engineering with a review of the different quantum cascade laser designs which have demonstrated lasing action is given in Appendix C.

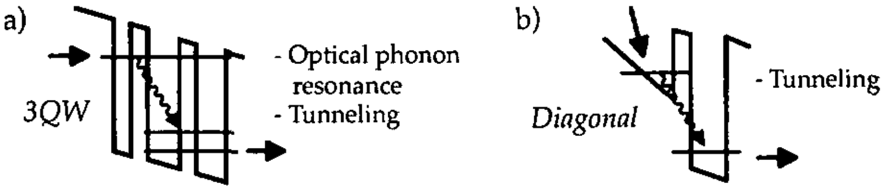

Figure 2.5: a) Three quantum well active region based on optical phonon resonance extraction of the lower state of the transition and b) active region based on photon-assisted tunneling (diagonal) transition, without using an optical phonon resonance for the extraction.

As shown schematically in Fig. 2.6, one period of a photon-assisted tunneling transition structure comprises a trapezoidal well consisting of a short period superlattice and a quantum well with two tunneling barriers. Under suitable applied bias, photon-assisted tunneling emission occurs across the injection barrier upstream from the quantum well. The downstream barrier allows electron escape into the next well by tunneling.

At low electric fields, the trapezoidal well creates a thick effective barrier between the ground states of the wide quantum wells (dotted lines in Fig. 2.6 a), and the current flowing through the structure by hopping is negligible. A significant current starts to flow in the structure only for applied fields large enough to compensate the conduction band gradient of opposite sign in the trapezoidal well, as schematized in Fig. 2.6 b). Above threshold, the ground state 1 of the injector is energetically separated from the ground state 1' and the excited state 2' of the well in the adjacent period downstream, as schematized in Fig. 2.6 c). This prevents resonant tunneling injection into these two latter states and thus negative differential resistance. The transport between states 1 and 1' is then described in terms of photon-assisted tunneling. This insures a stable injection without high field domains in the whole operating range of the laser, unlike in the resonant tunneling structures proposed by Kazarinov and Suris described in Sec. 2.4. In this field range, the ground state $n = 1$ of one period, which is also the upper state of the laser transition, has a lifetime which is by design much longer than that of the other states, including the lower $n = 1'$ state, and, therefore, contains the majority of the electron population. In this design, the threshold condition is then achieved by keeping the upper state population essentially constant while increasing the optical matrix element of the laser transition with electric field. This is in marked contrast to other QC lasers, where the threshold condition is achieved by increasing the population inversion, either by electrical or optical pumping.

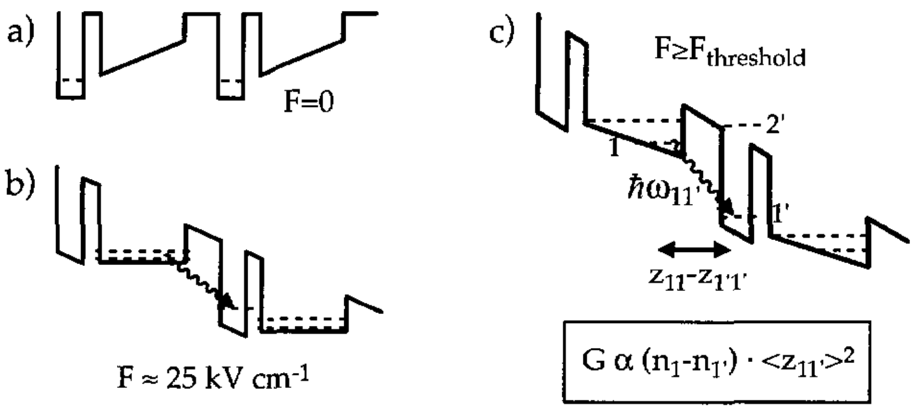

Figure 2.6: Schematic band diagram of two periods for different applied electric field (a) $F = 0$, b) $F \approx 25$ kV cm^{-1} and c) $F > F_{threshold}$) showing the principle of laser action in a diagonal transition. The electron population is majoritary concentrated in the lowest state of the triangular well created by the applied field. Laser action occurs when the latter is increased until the oscillator strength of the $1 - 1'$ transition satisfies the threshold condition. The wavy arrow indicates the radiative transition.

The total gain can be written as the product of the population difference $\Delta n = (n_1 - n_{1'})$ between the states 1 and 1', the dipole matrix element squared and the transition energy. As below threshold, the population difference Δn is essentially constant, the electric field dependence of the gain is due to: *i)* the increased dipole due to the enhanced spatial overlap between the 1-1' states; *ii)* the linear Stark effect which increases the transition energy $E_{11'}$. One has then laser action by oscillator strength tuning in a photon-assisted tunneling transition.

Because of the spatial separation between the centers of the wavefunctions of the laser transition, which is very large in this type of active region design, this design offers in addition the potential of very wide electrical tunability defining the ultimate limit in the electric tunability of QC lasers [74, 72].

Such lasers may also be seen as a kind of "model system" which is easier to describe than conventional QC structures. In particular, the injection process is easy to model since it is just a capture process into the lower state of the injection region. The transport (V-I) characteristics can therefore be computed "ab initio" from the values of the optical phonon scattering rates. In contrast, V-I characteristics have also been computed in conventional QC structures, but the model requires the introduction of a phenomenological broadening parameter, the in-plane scattering time [75]. We performed detailed characterization and modeling for such a photon-assisted tunneling transition. In particular, the influence of a non-zero lifetime of the lower state of the transition on the voltage-current (V-I) and threshold current versus temperature characteristics have been studied both theoretically and experimentally. This model is presented, together with the experimental results for comparisons, in Sec. 4.1.

2.7 Magnetic field

One goal of this thesis was to study quantum cascade structures in a strong magnetic field. This paragraph is therefore devoted to the analysis of the motion of a quasi bidimensional electron gas subjected to a static and uniform magnetic field $\vec{B}$ [76]. Let us consider first the general case where the magnetic field is tilted by an angle θ with respect to the growth axis (z-axis) of the structure (see Fig. 2.7). This choice of axes defines the magnetic field $\vec{B}$ in the $y-z$ plane, whereas the confinement potential $V_{conf}(z)$, due to the conduction-band discontinuity, is along the z-axis. Using the Landau gauge ($div\vec{A}=0$), the potential vector

$\vec{A}$ of $\vec{B}$ is relatively simple to deduce ($\vec{B} = \vec{\nabla} \times \vec{A}$) and one sets:

$$\text{Magnetic field } \vec{B} = \begin{pmatrix} 0 \\ Bsin\theta \\ Bcos\theta \end{pmatrix} \qquad \text{Potential-vector } \vec{A} = \begin{pmatrix} Bzsin\theta \\ Bxcos\theta \\ 0 \end{pmatrix} \tag{2.7.11}$$

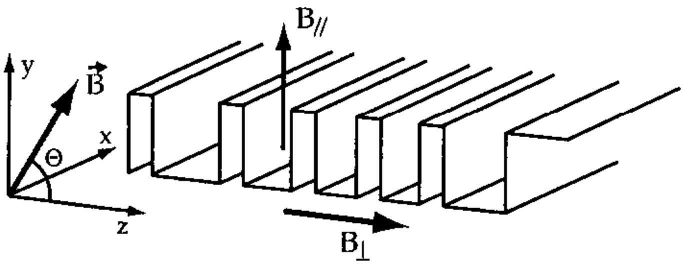

Figure 2.7: Magnetic field configuration for a quantum well structure. The z-axis corresponds to the growth axis. The two cases presented further are also shown as $B_{||}(\theta = 90°)$ and $B_{\perp}(\theta = 0)$.

The Hamiltonian is given by

$$H = \frac{1}{2m^*}\vec{\Pi}^2 + V_{conf}(z) + g^*\mu_B\vec{\sigma}\cdot\vec{B} \tag{2.7.12}$$

with $\vec{\Pi} = \vec{P} - q\vec{A}$ being the canonical momentum, m^* the effective mass, and q the charge of the carrier ($q = -e$ for electrons, $e > 0$). The last term takes into account the electron spin $\vec{\sigma}$ which interacts with the magnetic field adding to the particle energy the quantity $g^*\mu_B\vec{\sigma}\cdot\vec{B}$, where $\mu_B = \frac{e\hbar}{2m_0} = 9.27 \cdot 10^{-24}$ J/T is the Bohr magneton and g^* is the effective Landé g factor of the carrier. The operator $\vec{\sigma}$ has the eigenvalues $\pm\frac{1}{2}$. We ignore here the effective mass difference between the well and the barrier. Introducing the expression for the momentum operator $\vec{P} = -i\hbar\vec{\nabla}$ and for the position operator $Z = z$, as well as the notations $Bsin\theta = B_{||}$ and $Bcos\theta = B_{\perp}$ (see Fig. 2.7), the hamiltonian 2.7.12 becomes

$$
\begin{aligned}
H &= \frac{1}{2m^*}\left[\left(P_x + eB_{\|}Z\right)^2 + \left(P_y + eB_{\perp}X\right)^2\right] + \frac{P_z^2}{2m^*} + V_{conf}(z) + g^*\mu_B\vec{\sigma}\cdot\vec{B} \\
&= \frac{1}{2m^*}\left(P_x^2 + 2eB_{\|}P_xZ + e^2B_{\|}^2Z^2 + P_y^2 + 2eB_{\perp}P_yX + e^2B_{\perp}^2X^2\right) \\
&\quad + \frac{P_z^2}{2m^*} + V_{conf}(z) + g^*\mu_B\vec{\sigma}\cdot\vec{B} \\
&= \frac{1}{2m^*}\left(-\hbar^2\frac{\partial^2}{\partial x^2} - 2ieB_{\|}\hbar\frac{\partial}{\partial x}z + e^2B_{\|}^2z^2\right) + \frac{1}{2m^*}\left(-\hbar^2\frac{\partial^2}{\partial y^2} - 2ieB_{\perp}\hbar\frac{\partial}{\partial y}x + e^2B_{\perp}^2x^2\right) \\
&\quad - \frac{\hbar^2}{2m^*}\frac{\partial^2}{\partial z^2} + V_{conf}(z) + g^*\mu_B\vec{\sigma}\cdot\vec{B}
\end{aligned}
\tag{2.7.13}
$$

It is now possible to separate the orbital and spin variables. The spin term is rotationally invariant. Therefore, if we quantized $\vec{\sigma}$ along a fixed direction (say y), we will obtain the same spin eigenvalues $\pm\frac{1}{2}g^*\mu_B B$. Thus the spin-splitting is only depending on the modulus of $\vec{B}$, not on its direction. The value of the effective Landé g factor is about $g^* = -0.4$ for GaAs wells [77, 78], whereas the bulk value at low temperature is about -0.44 [79, 80]. This value increases for thin wells as shown theoretically [78] and experimentally [81]. For bulk $In_{0.53}Ga_{0.47}As$, g^* is about -4.1 theoretically [82] as well as experimentally [83]. Again, this value is expected to increase for thin wells [82, 78]. The spin splitting $\frac{1}{2}g^*\mu_B B$ at 12 T is therefore about 1.4 meV for InGaAs and 0.14 meV for GaAs.

Let us take the orbital part of the Hamiltonian 2.7.13. We notice that it is y-independent, Thus the wave function $\Psi(x, y, z)$ is given by a function of x and z and by a plane wave in the y-direction

$$\Psi(x, y, z) = \varphi_k(x, z)\cdot e^{ik_y y} \tag{2.7.14}$$

The Schroedinger equation $H\Psi(x, y, z) = E\Psi(x, y, z)$ is in this case

$$
\begin{aligned}
&\left[-\frac{\hbar^2}{2m^*}\frac{\partial^2}{\partial z^2} + V_{conf}(z) - \frac{\hbar^2}{2m^*}\frac{\partial^2}{\partial x^2} + \frac{1}{2m^*}\left(\hbar k_y + eB_{\perp}x\right)^2\right. \\
&\qquad\left. + \frac{1}{2m^*}\left(e^2B_{\|}^2z^2 - 2ieB_{\|}\hbar\frac{\partial}{\partial x}z\right)\right]\varphi_k(x, z) = E\varphi_k(x, z)
\end{aligned}
\tag{2.7.15}
$$

We can now decouple the problem in two different cases studied separately :

a) Magnetic field perpendicular to the layers (parallel to the growth axis): $\theta = 0$, $\vec{B} = (0, 0, B_\perp)$. This case will be treated in paragraph 2.7.1.

b) Magnetic field parallel to the layers: $\theta = 90°$, $\vec{B} = (0, B_{||}, 0)$. This case will be treated in paragraph 2.7.2.

2.7.1 Perpendicular magnetic field

With a magnetic field only perpendicular to the layers, the Schroedinger equation 2.7.15 is reduced to

$$\left[-\frac{\hbar^2}{2m^*}\frac{\partial^2}{\partial z^2} - \frac{\hbar^2}{2m^*}\frac{\partial^2}{\partial x^2} + \frac{1}{2m^*}\left(\hbar k_y + eB_\perp x\right)^2 + V_{conf}(z)\right]\varphi_k(x, z) = E\varphi_k(x, z) \quad (2.7.16)$$

The wave function $\varphi_k(x, z)$ can be factorized into

$$\varphi_k(x, z) = \varphi_n(x) \cdot \chi_m(z) \quad (2.7.17)$$

Substituting 2.7.17 in 2.7.16, we obtain the following equations for $\varphi_n(x)$ and $\chi_m(z)$

$$\left[-\frac{\hbar^2}{2m^*}\frac{\partial^2}{\partial z^2} + V_{conf}(z)\right]\chi_m(z) = \xi_m \chi_m(z) \quad (2.7.18a)$$

$$\frac{\partial^2 \varphi_n(x)}{\partial x^2} + \frac{2m^*}{\hbar^2}\left[E_n - \frac{\hbar^2 k_y^2}{2m^*} - \frac{2\hbar k_y e B_\perp x}{2m^*} - \frac{e^2 B_\perp^2 x^2}{2m^*}\right]\varphi_n(x) = 0 \quad (2.7.18b)$$

$\chi_m(z)$ are the wave functions for the z motion corresponding to the m^{th} state (bound or unbound) of energy ξ_m for the heterostructure Hamiltonian without magnetic field. Introducing $\omega_c = \frac{eB_\perp}{m^*}$ in Equ. 2.7.18b, which is called cyclotron frequency, and $x_0 = \frac{\hbar k_y}{eB_\perp} = \frac{\hbar k_y}{m^* \omega_c}$, one can write

$$\frac{\partial^2 \varphi_n(x)}{\partial x^2} + \frac{2m^*}{\hbar^2}\left[E_n - \frac{m^* \omega_c^2}{2}\left(x + x_0\right)^2\right]\varphi_n(x) = 0 \quad (2.7.19)$$

This equation is identical to the Schroedinger equation of a harmonic oscillator oscillating at a frequency ω_c around the point $x = x_0$. One concludes that the constant E_n is the oscillator energy which can take the values $(n + 1/2)\hbar\omega_c$, n being an integer.
Thus one obtains the eigenvalues of Eqn. 2.7.19 which are k_y-independent and evenly spaced in $\hbar\omega_c$. They are the well-known Landau levels [84] (see Fig. 2.8):

$$E_n(k_y) = \left(n + \frac{1}{2}\right)\hbar\omega_c \quad ; \quad n = 0, 1, 2\ldots \tag{2.7.20}$$

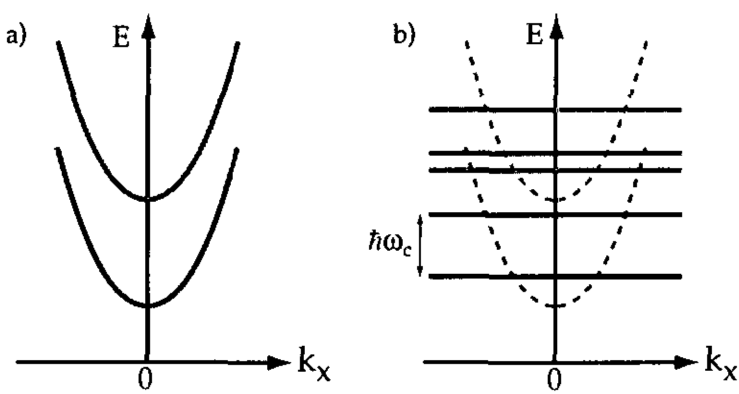

Figure 2.8: Dispersion relation for the two subbands a) in the absence of magnetic field and b) with a perpendicular magnetic field present. The subbands split in this case in Landau levels separated by $\hbar\omega_c$.

The eigenstates $|\nu\rangle = |m, n, k_y\rangle$ of the Hamiltonian in Equ. 2.7.16 consist of Landau level ladders which are attached to each of the zero field heterostructures bound (or unbound) states. The energy levels of a particle in a magnetic field perpendicular to the layers is therefore

$$E_\nu = \xi_m + \left(n + \frac{1}{2}\right)\hbar\omega_c \tag{2.7.21}$$

The carrier motion is then entirely quantized. Indeed $V_{conf}(z)$ has quantized the z component of the carrier motion, whereas the magnetic field along the growth axis (perpendicular to the layers) has quantized the in-plane motion.

2.7.2 Parallel magnetic field

In this second case, with a magnetic field only parallel to the layers, the Schroedinger equation 2.7.15 is reduced to

$$\left[\frac{1}{2m^*}\left(-\hbar^2\frac{\partial^2}{\partial z^2}-\hbar^2\frac{\partial^2}{\partial x^2}+\hbar^2k_y^2+e^2B_\parallel^2z^2-2ieB_\parallel\hbar\frac{\partial}{\partial x}z\right)+V_{conf}(z)\right]\varphi_k(x,z)=E\varphi_k(x,z) \tag{2.7.22}$$

The wave function $\varphi_k(x,z)$ can be simplified because the latter Hamiltonian does not contain the x coordinate. So we will look for

$$\varphi_k(x,z)=\varphi_k(z)\cdot e^{ik_xx} \tag{2.7.23}$$

and the equation 2.7.22 simplifies in

$$\left[-\hbar^2\frac{\partial^2}{\partial z^2}+V_{conf}(z)+\frac{\hbar^2}{2m^*}\left(k_x^2+\frac{2eB_\parallel k_xz}{\hbar}+\frac{e^2B_\parallel^2z^2}{\hbar^2}\right)+\frac{\hbar^2}{2m^*}k_y^2\right]\varphi_k(z)=E\varphi_k(z) \tag{2.7.24}$$

The magnetic field can now be treated as a perturbation; this allows us to find the eigenvalues of the Hamiltonian [85, 86, 87]. The presence of crossed electric and magnetic fields has been also treated without applying the perturbation procedure [88, 89]. The first-order perturbation-theory calculation gives the energy as [90, 91]

$$E=E_{conf}(z)+\frac{\hbar^2}{2m^*}k_y^2+\frac{\hbar^2}{2m^*}k_x^2+\frac{2eB_\parallel\hbar}{2m^*}k_x\langle z\rangle+\frac{e^2B_\parallel^2\langle z^2\rangle}{2m^*}\quad, \tag{2.7.25}$$

where $E_{conf}(z)$ is the confinement energy due to the potential $V_{conf}(z)$. The three first terms are the eigenvalues of 2.7.24 if the parallel magnetic field is zero. The two last terms are the result of the perturbation theory $\langle\varphi_k(z)|H_{pert}|\varphi_k(z)\rangle$. The terms $\langle z^2\rangle$ and $\langle z\rangle$ are the expectation values of the respective operators for the unperturbed wave functions. In fact $\langle z\rangle$ represents the position of the gravity center of the wavefunction $\varphi_k(z)$ in function of the origin of the z-axis. One can rewrite the expression 2.7.25 by forming a square such as $(k_x + \frac{eB_\parallel(z)}{\hbar})^2$:

$$E = E_{conf}(z) + \frac{\hbar^2}{2m^*}k_y^2 + \frac{\hbar^2}{2m^*}\left(k_x + \frac{eB_\parallel(z)}{\hbar}\right)^2 + \frac{e^2B_\parallel^2}{2m^*}\left(\langle z^2\rangle - \langle z\rangle^2\right) \quad . \tag{2.7.26}$$

One observes that the usual k_x^2-dispersion changes in a parabola shifted by a quantity called $k_{shift} = -\frac{eB_\parallel(z)}{\hbar}$. The last term $(\langle z^2\rangle - \langle z\rangle^2)$ is independent of the choice of the origin. It represents a diamagnetic shift which changes only slightly the energy and can be neglected for thin wells. These effects are shown schematically in Fig. 2.9 for the two subbands involved in a diagonal transition.

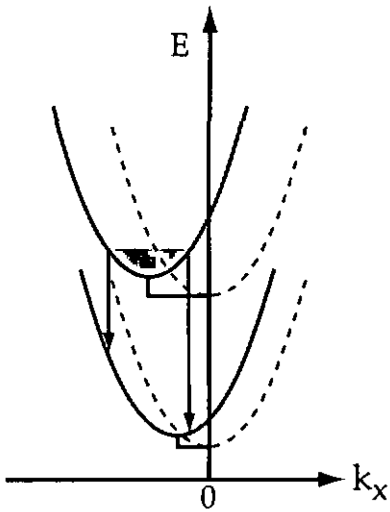

Figure 2.9: Dispersion relation for the upper and lower state of a diagonal transition in the absence of magnetic field (dashed curves) and with a parallel magnetic field present (solid curves). According to theory the parabola are shifted in the k_x direction by $-\frac{eB_\parallel(z)}{\hbar}$ and raised in energy by $\frac{e^2B_\parallel^2}{2m^*}\left(\langle z^2\rangle - \langle z\rangle^2\right)$. The arrows indicate the maximum and minimum energy splittings.

It is clear now that the k_{shift}-effect is a pure diagonal transition effect. Indeed, the value of $\langle z \rangle$ can be chosen to be the zero of the z-axis (for example for the lower state of the transition). So the k_x-dispersion of the upper state of the transition will be shifted with respect to the latter. For a vertical transition, $\langle z \rangle$ is the same for the two states involved in the transition and therefore the dispersion relations will not be changed. If the parabola are shifted as in Fig. 2.9, the transition energy can be different depending on where you are in the dispersion curve: for example at $k_x = 0$ or $k_x = k_{shift}$.

Chapter 3

Experimental setup and sample fabrication

In the first sections of this chapter, we describe the experimental setup which was developed to perform mid-infrared measurements in a magnetic field as well as far-infrared magneto-transport measurements and electroluminescence in a perpendicular magnetic field. Then will follow a description of the sample growth technique, the molecular beam epitaxy. The last section of the chapter is devoted to the devices processing, both for mid- and far-infrared samples.

3.1 Magnetic field cryostat

All measurements performed in a magnetic field have been done in a cryostat which contains a superconducting coil allowing us to reach a magnetic field of 14 T, when using a lambda plate above 12 T. This cryostat was supplied by Janis Research Company, Inc.[1] and comprises a ^{4}He dewar which can contain up to about 25 liters of liquid helium allowing an autonomy of about 60 hours before refill (without pumping on the sample tube or using the magnet). The magnet inductance is 31.5 H and the maximum magnetic field of 12 T at 4.2 K corresponds to a rated current of 78.3 A, while the maximum magnetic field of 14 T at 2.2 K corresponds

[1] Janis Research Company, Inc., PO Box 696, 2 Jewel Drive, Wilmington, MA 01887, USA.

to a rated current of 91.35 A. The precise field to current ratio is 0.1533 T/A. The bottom flanges have windows to collect the light from the inner sample tube (see Fig. 3.2). The tricky piece of this assembly is the window separating the vacuum and the sample tube which can be filled with liquid helium. We use a sapphire window for mid-infrared measurements up to 6 μm. Indeed sapphire is completely transparent in the near-infrared up to 4.5 μm, with still 10 % of transmittance at 6 μm. For longer wavelengths, such as for all our samples at about 10 μm, we need a ZnS window which is more delicate, but transparent up to 14 μm. The sample temperature can be varied between 2 and 300 K using a needle flow control valve between the helium bath and the sample tube.

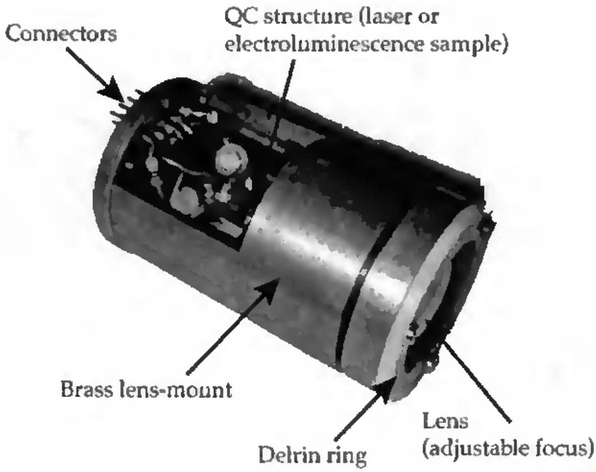

Figure 3.1: Sample holder and lens mount for mid-infrared measurements.

For mid-infrared electroluminescence, the devices are mounted on special holders which allow measurements in perpendicular- as well as in parallel-magnetic field. To collect the light, a f/1.36 lens (38.1 mm focal length, 27.94 mm diameter) is fixed on the sample holder with a brass mount and a delrin ring to overcome the thermal stress due to cooling down to 2.2 K (see Fig. 3.1). The resulting parallel beam leaves the cryostat through the sapphire or ZnS/ZnSe windows system and is then collected by mirrors and lenses to be sent in a Fourier-transform infrared interferometer (FTIR) Nicolet 860 to perform spectra or in a HgCdTe detector to perform L-I curves (for a laser).

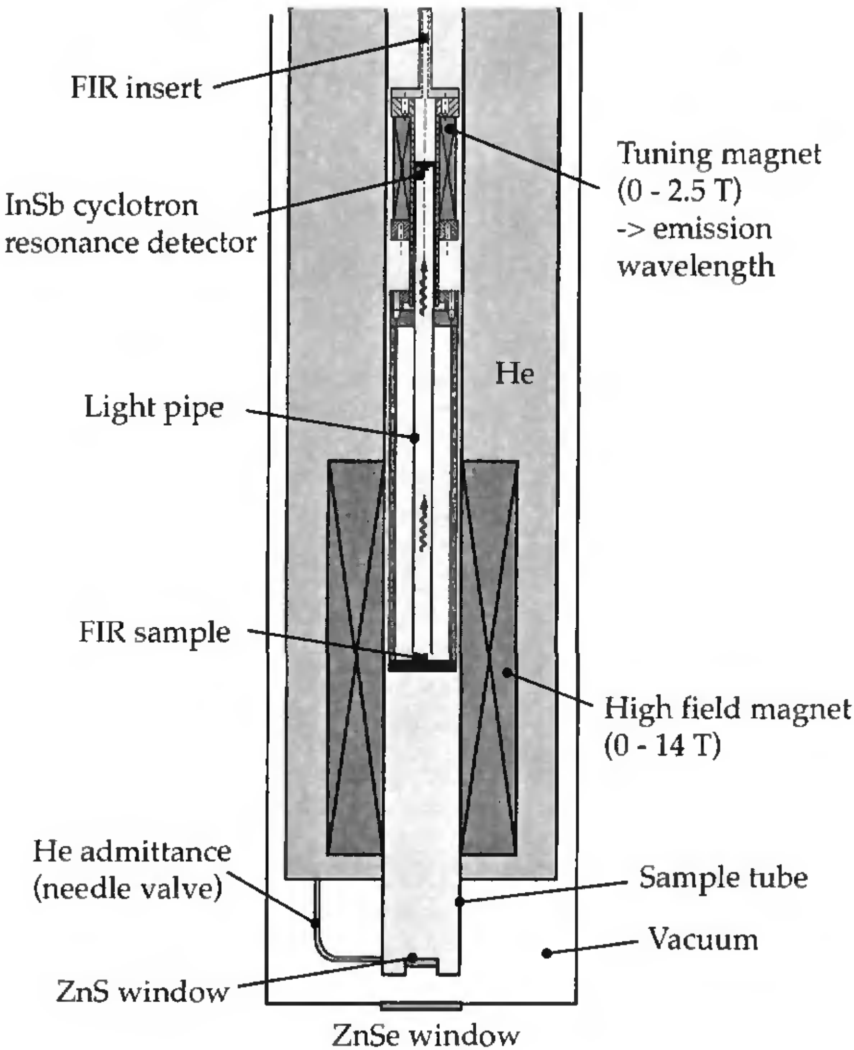

Figure 3.2: Experimental setup used for far-infrared spectra in magnetic field.

3.2 Far-infrared insert

In order to perform optical measurement in the far-infrared and in high magnetic field, we decided to use a new insert. This sample-insert contains a small 2.5 T-magnet coil and a magnetically tunable InSb-cyclotron resonance detector [92, 93], which operates as a photoconductor. This latter is located in the center of the small magnet while the sample is located in the center of the 12 T-magnet of the cryostat itself. The light is then collected by a copper light-pipe. The whole assembly is finally immersed in liquid helium (see Fig. 3.2). The insert containing the small magnet was also supplied by Janis Research Company, Inc. The magnet inductance is 1.3 H and the maximum magnetic field of 2.5 T corresponds to a rated current of 7.69 A. The field to current ratio is 0.32513 T/A.

Figure 3.3: Photo of the InSb detector-mount

The detector mounts have been supplied by QMC Instruments Ltd to be inserted into the light pipe. Fig. 3.3 shows a photograph of the detector mount with such an InSb detector. The detector is electrically isolated from the block mount by a quartz substrate. The detector block itself has a flat face to allow mounting of a Hall probe device in close proximity to the detector. This allows to measure the magnetic field on the detector (see Sec. 3.3). Two holes allow the passage of Hall probe wiring. A spring loaded ball bearing is located into a small hole in the side of the light pipe to maintain the assembly in place. The spectra are then performed by sweeping the detector magnetic field (small coil) while keeping the sample magnetic field (big coil) constant. To know the absorption wavelength of the detector, we have to convert the rated current (or magnetic field) of the small coil in energy. As the InSb has an effective mass of $m^* = 0.0139 m_0$, the cyclotron energy (at which the detector absorbs light) is $\hbar\omega_c = \frac{\hbar e B}{m^*} = 8.324 \cdot B$ [meV] (or $2.706 \cdot I$ [meV]).

The use of this magnetically tunable cyclotron-resonance detector has an inferior spectral resolution than the FTIR spectrometer (see Appendix D). A schematic drawing of the standard FIR electroluminescence setup is shown in Fig. 3.4. The light coming from the sample is collected by an off-axis parabolic mirror with an $f/1.5$ aperture and sent through a FTIR spectrometer in a liquid-helium cooled Si bolometer [2].

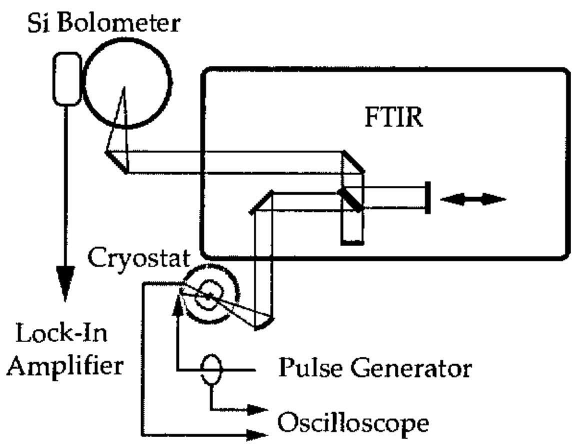

Figure 3.4: Schematic drawing of the FIR electroluminescence setup [12].

[2]An optical calibration of the Si bolometer has been performed using a blackbody radiation source. A large difference between the electric and optical responsivity has been observed. Indeed the optical responsivity was found to be only 13% of the claimed electrical responsivity specified by the manufacturer.

The use of the two setups together will give the possibility to work with a high spectral resolution (1 cm^{-1} or better with FTIR) on one side and offer the possibility of applying a strong magnetic field on the structures on the other side. This new FIR setup has also a further advantage besides allowing the measurement of a sample with an applied magnetic field: it should have a much better signal to noise ratio compared to our standard electroluminescence setup. Indeed, high-performance FIR detectors are usually limited by the room temperature 300K thermal background radiation. By immersing the whole setup in liquid Helium, we completely remove this noise source. After measurements performed at 4.2K and having an insufficient signal to noise ratio, we decided to work at a lower temperature (3 K) by pumping on the sample tube. By decreasing the temperature, we decrease the Johnson noise and there is also an increase in the InSb detector resistance. Therefore we should have a pronounced improvement in the NEP. The V-I curves and main characteristics of the detector are discussed in the Appendix D.

3.3 Hall probe

We use a home-made two dimensional electron gas (2DEG) sample in the standard-Van der Pauw geometry as a Hall probe to accurately measure the magnetic field due to the small and the big coil felt by the detector. Indeed, the big 14 T-coil induces a non-negligible magnetic field on the detector, mainly because of the short distance separating the center of them ($\sim$ 25 cm). Therefore the spectra performed at high magnetic field have to be corrected in energy. We measure the Hall voltage by the Van der Pauw technique using a Hall current of 100 μA. Typical Hall measurements performed at magnetic fields of 0, 4, 8 and 12 T in the big coil at 3 K as a function of the magnetic field in the small coil are shown in Fig. 3.5 a). These measurements allow also to deduce the 2DEG sheet carrier concentration n_s since the sample resistivity ρ_{xy} (ratio of the Hall transverse voltage V divided by the longitudinal current I) is given by [76]

$$\rho_{xy} \equiv \frac{V}{I} = \frac{m^*\omega_c}{n_s e^2} = \frac{B}{en_s} \tag{3.3.1}$$

where m^* is the effective mass and $\omega_c = \frac{eB}{m^*}$ the cyclotron frequency.

The Hall resistivity increases then linearly with the applied magnetic field. We obtain a 2DEG sheet carrier concentration of $n_s = 2.1 \cdot 10^{12}$ cm^{-2}. The oscillations observed for magnetic field higher than 1.5 T are due to Landau quantization, in units of a fundamental constant $\left(\frac{h}{e^2}\right)$, known as the quantized Hall effect [94, 95, 96, 97].

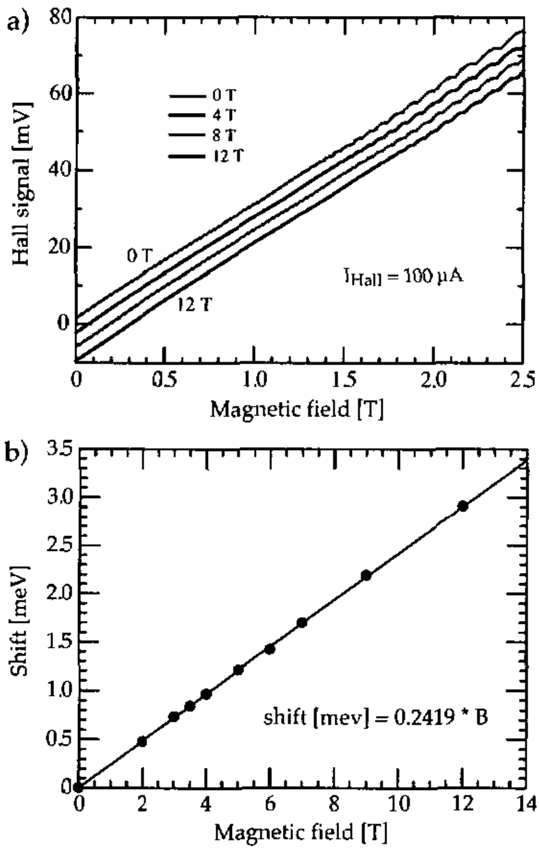

Figure 3.5: a) Typical Hall measurements as a function of the magnetic field in the small coil at 3 K and b) correction in energy (shift of the raw spectra) deduced from these Hall measurements due to the magnetic field induced by the big coil on the detector.

These Hall measurements allow us to determine the quantity which we have to subtract at the emission energy detected by the InSb detector. With the value obtained for different magnetic fields in the big coil, we deduced that the raw data should simply be shifted by a quantity of $0.2419 \cdot B$, where B is the field in the big coil (or by $2.796 \cdot I$, where I is the rated current of the small coil), as shown in Fig. 3.5 b).

3.4 Growth

In the course of this thesis, all samples, both on InP- and on GaAs-substrate, were grown by molecular beam epitaxy (MBE). The quantum cascade lasers consist of III-V heterostructures. The group III elements are aluminium (Al), gallium (Ga) and indium (In), with arsenic (As) being the only V element. MBE is basically an evaporation technique under ultra-high vacuum (UHV) conditions (base pressure $< 10^{-10}$ mbar), which allows the growth of very thin layers (< 5 Å) with sharp interfaces and an excellent compositional control (for a review, see for example [6]). MBE systems include in situ analysis capabilities. For example an electron gun for reflection high-energy electron diffraction (RHEED) which allows the analysis of the growing surface to monitor and control the growth conditions. There is also a mass spectrometer to analyze trace gases which is in particular very useful to detect micro-leaks. The typical MBE growth rate is in the order of one monolayer per second, corresponding to approximatively 1 μm per hour. The quality of the growth can then be controlled by X-ray diffraction. Fig. 3.6 is a transmission electron microscope (TEM) image of a portion of the cleaved cross section of a quantum cascade laser active region: the quality of the interfaces is really excellent.

The MBE growth of the sample studied during this thesis was carried out by Dr. Mattias Beck (usually the InP-based samples) and Dr. Ursula Oesterle (usually the GaAs-based FIR samples) at IMO, EPFL in Lausanne and also by the Cavendish Laboratory's group at Cambridge (UK) for some GaAs-based FIR samples.

A complete listing of the structures studied during this thesis can be found in the Appendix A, with the layer sequence of one period, the doping and the number of periods of each sample.

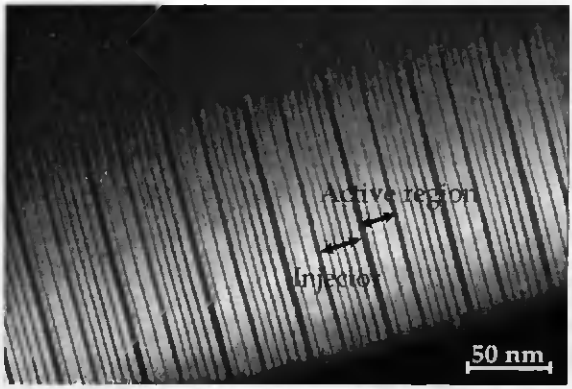

Figure 3.6: TEM image of a part of a portion of the cleaved cross section of a quantum cascade laser active region (sample S1549). This image was provided by Fabienne Bobard at EPFL-Cime.

3.5 Processing

3.5.1 Mid-infrared structures

The active region must be embedded in an optical waveguide to obtain laser action. This waveguide must fulfill the requirements of low optical losses and high confinement (or overlap) factor Γ with, at the same time, a minimum thickness of grown material for a TM propagating mode, as required by the optical selection rules for intersubband transitions. On both sides of the active region, the waveguide comprises then two thick guiding layers (in InGaAs for InP-based QC lasers), which enhance the optical confinement by increasing the refractive index difference between the core and cladding regions of the waveguide. This will confine the laser mode vertically in the cavity. The bottom cladding is formed by the InP substrate. The top cladding consists of a thick InAlAs layer followed by a thick heavily doped InGaAs layer. The purpose of this InGaAs layer is to decouple the high loss metal-semiconductor interface plasmon mode from the laser mode. The complete layer sequence of the waveguide for a laser at about $\lambda \sim 10\mu m$ (typically laser S1548 extensively measured) is shown in Table 3.1.

An other important feature of the waveguide design is to minimize the optical losses due to free carriers. This is obtained by reducing the doping level around the waveguide region to its minimum value while maintaining low resistivity. The mode profile, effective refractive index and optical losses are calculated by solving the wave equation for a planar waveguide with a complex propagation constant and modeling each layer with its complex refractive index. The free-carrier absorption losses (imaginary part of the refractive index) are obtained using the Drude model [98, 34].

Material	Thickness [nm]	Doping [cm^{-3}]
GaInAs	1050	$7 \cdot 10^{18}$
AlInAs	1050	$1.5 \cdot 10^{17}$
GaInAs	800	$6 \cdot 10^{16}$
35x Active	1700	
GaInAs	700	$6 \cdot 10^{16}$
InP		$1 - 5 \cdot 10^{17}$

Table 3.1: Waveguide layer structure for a laser at about $\lambda \sim 10\mu m$.

For laser characterization, the structures are usually processed into ridge waveguides of 28 μm-width by wet chemical etching. A thick isolation layer (normally SiO_2 or Si_3N_4 depending of the emission wavelength) is then deposited by PECVD, but during this thesis we tried also with ZnSe evaporated by e-gun. Ti/Au ohmic contacts are evaporated on the top. Thinning (to reach a thickness of about 150-200 μm), back contacting with Ge-Au-Ag-Au (usual respective thicknesses of 12-27-50-100 nm) and cleaving complete the processing. The two mirrors of the laser cavity are then provided simply by the cleaved facets. A schematic drawing of a processed laser stripe is shown in Fig. 3.7 a). The devices are usually cleaved in 0.5- to 3-mm-long bars.

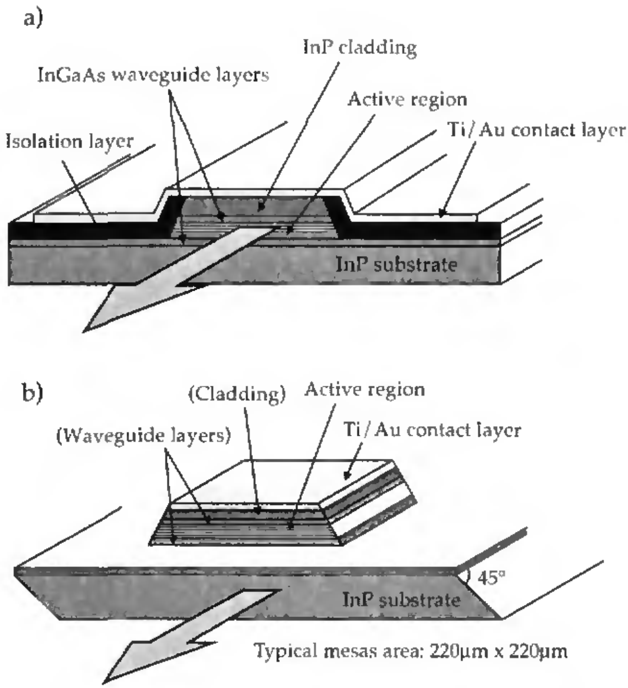

Figure 3.7: a) a laser stripe (the light comes from a cleaved facet) and b) a mesa for electroluminescence measurements (the light is coupled out of the structure through the polished wedge at 45° angle from the plane of the layers). The waveguide and cladding layers are normally not grown for luminescence samples. There are present if one process a laser sample for luminescence experiment.

Recently, better laser performances have been achieved by substituting the SiO_2 / Si_3N_4 isolators by InP regrowth, which allows lower lateral waveguide losses and improves lateral heat dissipation [99]. The samples are etched as ridge waveguides after MBE growth and then transferred into a MOCVD (metal-organic chemical vapor deposition) reactor to form buried heterostructures, the top of the mesa ridge being covered by SiO_2 inhibiting InP regrowth on top of the cladding. The SiO_2 film is removed chemically after deposition of 3 μm nonintentionally doped InP and non-alloyed Ti/Au ohmic contacts are finally evaporated to the top of the highly doped cladding layer. This buried heterostructure QC laser yields both lower optical losses (higher slope efficiency) and a higher thermal conductivity, allowing higher average powers and higher duty cycle operation [99, 100, 11].

For luminescence measurements, the structures are normally processed in mesas of between 220 μm × 220 μm and 450 μm × 450 μm instead of laser stripes, as shown in Fig. 3.7 b). That is to avoid optical feedback and gain. The light is then coupled out the structure through a polished wedge which forms a 45° angle with the plane of the layers. The 45° angle-wedge is provided to collect as much light as possible. In fact the light is deviated by an angle of about 33° between the air and the semiconductor due to the refractive index change at the interface.

The cleaved laser devices, or luminescence devices, are then soldered epilayer up to a copper holder, wire-bonded with Au wires and mounted in the cold head of a temperature controlled helium flow cryostat, on a Peltier-cooled laser housing or on specific sample mounts for the magnet-cryostat.

3.5.2 Far-infrared or terahertz structures

For the electroluminescence experiments, the FIR samples were processed into mesas of typically between 220 μm × 220 μm and 450 μm × 450 μm with Au/Ge ohmic contacts on top. The light was extracted from the structures through an evaporated Ti/Au metal grating of 15 μm periodicity, as explained below. To see whether the far-infrared structures have gain, we have to embed them in a waveguide, as for the mid-infrared QC lasers. But in the far-infrared, waveguides based on pure dielectric confinement would require a cladding thickness on the order of 20-50 μm, which is unreasonable. This technological difficulty can be avoided by using a metal instead of dielectrics for the mode confinement. Sirtori *et al.* used first this technique in a waveguide based on surface plasmons with a QC laser at long wavelength [101]. The FIR waveguides used for some sample in this thesis are based on metal-dielectric-metal, or double plasmon confinement [102]. The metal layer below the active region is replaced by a heavily doped GaAs layer, which leads to similar guiding properties as a metal-semiconductor-metal confinement, but with slightly higher waveguide losses. However, these waveguides allows a drastic reduction of the cladding thickness and achieve larger overlap factor.

For the structures designed to emit in the far-infrared, or terahertz, range, the light must be coupled out by a metal grating. Indeed, the selection rules for intersubband transitions require that the emitted light has an electric field polarized perpendicularly to the confining layers. The light with this polarization will then travel parallel to the layers, i.e. in the plane of the sample. As the absorption of the free carriers in the substrate is proportional to the square of the wavelength, it is impossible to extract the light with a 45° angle facet as in the mid-infrared. We use then a diffraction grating which converts the radiation polarized perpendicular to the interface into a plane wave radiating from the surface. The period of the grating must be smaller than the wavelength corresponding to the respective transition divided by the refractive index of the material. It has been observed experimentally [103, 46, 64] and theoretically [104] that the coupling efficiency decreases very rapidely towards longer grating periods, but quite slowly towards short periods. As the wavelength of the transition in the GaAs material is about 25 μm, we have chosen a grating period of 15 μm. If we focus on waves whose wavelength for a given frequency cannot propagate in the bulk and which are trapped on the surface, their decay length is given by the following relation [103]: $(2\pi/\lambda)^2 = (2\pi/d)^2 - 1/\delta^2$. Here λ is the wavelength of the emitted light in the GaAs, d the grating period and δ the thickness of the active region. We get an optimal grating period of 15 μm, using $\delta = 3\mu$m and $\lambda = 25\mu$m, in agreement with the chosen value.

Chapter 4

Mid-infrared quantum cascade lasers

This chapter of the thesis presents the main results obtained on mid-infrared structures, in particular a detailed analysis of the laser structure S1548 based on a photon-assisted tunneling transition (see Sec. 2.6 for theory). The second part of the chapter shows electroluminescence measurements performed on a superlattice, including a presentation of a method to investigate gain in such a superlattice, followed by a a discussion of the effects of a parallel magnetic field. Measurements performed in parallel magnetic field, including luminescence dependence of diagonal-based QCL and threshold current dependence of various QCLs, are presented in Sec. 4.4. Finally the effects of a perpendicular magnetic field on the threshold current of various QCLs are discussed in Sec. 4.5.

4.1 Photon-assisted tunneling transition-based QCL

We present here a detailed characterization and modeling of long-wavelength ($\lambda \sim 10\mu$m) quantum cascade lasers based on photon-assisted tunneling transition. Such QC lasers have already shown a promising degree of performance at $\lambda = 6.5$ μm with pulsed operation up to $T = 280$ K [71]. In Sec. 4.1.1, we present the design and the characterization of the laser. In Sec. 4.1.2, we develop a model based on an non-zero lower state lifetime and study voltage-current (V-I) and threshold current versus temperature characteristics both theoretically and experimentally. The V-I curves have been calculated at finite temperature, whereas previous studies were limited to low temperature. This model enables also the computation of gain saturation with temperature. A comparison of the model predictions with experiment is then discussed. Continuous-wave operation and a spectral analysis with waveguide loss measurements will be shown in Sec. 4.1.5 and Sec. 4.1.6, whereas electroluminescence measurements and the electrical tuning behavior of these lasers are presented in Sec. 4.1.7. We conclude this discussion in Sec. 4.1.8 with the presentation of two new designs. For both of them, we used a finite value of the lower state lifetime that was deduced from the experiments. We performed also measurements on a new photon-assisted tunneling design which should operate up to room-temperature.

4.1.1 Laser design and characterization

Each period of the laser structure S1548, as shown in Fig. 4.1, comprises an $Al_{0.48}In_{0.52}As$ / $In_{0.53}Ga_{0.47}As$ superlattice injector coupled to a 7.4 nm thick $In_{0.53}Ga_{0.47}As$ quantum well surrounded by two 2.5 nm thick $In_{0.52}Al_{0.48}As$ tunneling barriers. Under suitable applied bias, photon-assisted tunneling emission occurs across the injection barrier upstream from this quantum well (see Sec. 2.6). The downstream barrier allows electron escape into the next well by tunneling.

Typical light vs. current (L-I) and voltage vs. current (V-I) curves for a 28 μm-wide, 1.4-mm-long device are shown in Fig. 4.2. The current pulses were 100 ns long with a pulse repetition frequency of 5 kHz. At low temperature (80K), we observed a threshold current density of 1.1 kA/cm^2 and a maximum output power up to 160mW for 13 V bias voltage. This threshold current density is lower than the 3 kA/cm^2 [105] or the 1.4 kA/cm^2 [74] reported for this kind of QC lasers and at these long wavelengths. The laser operates up to 200K, with up to 20mW at 190K for the best device. The emission wavelength was on the order of 10 μm depending on electric field and temperature.

As shown in Fig. 4.2, the L-I characteristics of the device are not linear. The initial slope efficiency is very poor but increases rapidly with voltage. We attribute this behavior to the too small voltage at which the laser operates initially; at this small bias, the lower state of the laser transition is thermally populated due to its proximity ($\Delta \cong 30$ meV) to the Fermi sea of the injector. Shorter devices having larger mirror losses and therefore operating at higher biases did in contrast exhibit a linear L-I curve above threshold.

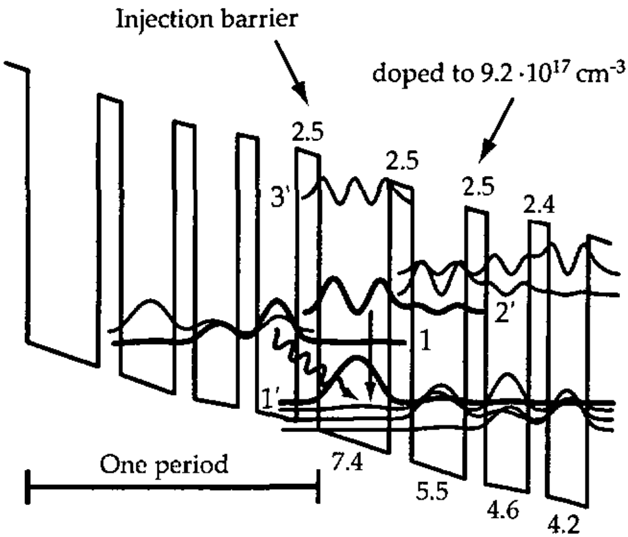

Figure 4.1: Self-consistent computation of the energy band diagram of two periods of the structure S1548 under an average applied electric field of about 55 kV/cm. The moduli squared of the relevant wave functions are shown. The wavy line indicates the transition responsible for laser action. The thickness of the different layers is indicated in nanometers.

The shape of the V-I curve (Fig. 4.2 and Fig. 4.8) is well understood: between 0 and about 4 Volts, the current is very small, because the injector states are not aligned (the electric field is small). The graded region creates a thick effective barrier between the ground states of the wide InGaAs quantum well and therefore the current flowing through the structure by hopping is negligible. When the voltage increases up to 5 V (corresponding to an electric field of 32 kV/cm), the injector states align and electrons can cascade into the structure. At the threshold voltage, we see in the V-I curve of Fig. 4.2, and particularly in Fig. 4.8, an abrupt slope change. Ideally (i.e. if the lower state lifetime $\tau_{1'}$ were negligible) the differential resistance above threshold should be zero, pinning the bias voltage at its threshold value. But here, due to the finite lifetime of the lower $n = 1'$ state, the change in differential conductance at threshold is small. We show in the next section that the ratio of the conductances below and above threshold is a measure of the ratio of the lifetimes of the states 1 and 1'.

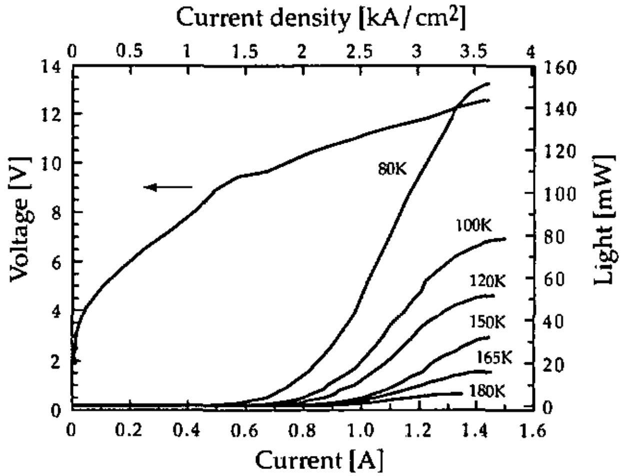

Figure 4.2: L-I curves in pulsed mode of a 28-μm-wide and 1.4-mm-long QC laser measured at different temperature. Also is shown a V-I curve measured at 80K.

4.1.2 Rate equations

In this approach, and in contrast to previous reports [71], we take into account *i)* a non-zero (but assumed constant) lower state lifetime $\tau_{1'}$ and *ii)* the fact that the total integrated charge in a period n_{tot} remains constant. For simplicity, we neglect the population of the other excited states of the injector and keep only the population $n_{1'}$ of the lower state of the laser transition. Therefore we are, in our model, left with only two states (1 and 1'). Their populations n_1 and $n_{1'}$ fulfill the equation

$$n_1 + n_{1'} = n_{tot} \quad . \tag{4.1.1}$$

In steady state, the rate equation for state 1 can be written as

$$-\frac{n_1}{\tau_1} - g_c S(n_1 - n_{1'}) + \frac{n_{1'}}{\tau_{1'}} = 0 \quad , \tag{4.1.2}$$

where S [$\mathrm{cm}^{-1} \cdot \mathrm{s}^{-1}$] is the photon flux per unit length per period and g_c [cm] the gain cross section [34]. The laser threshold condition, gain equals the total losses α_{tot}, is

$$g_c \cdot (n_1 - n_{1'}) = \alpha_{tot} \quad . \tag{4.1.3}$$

By design, the cross section gain g_c and the lifetime τ_1 are not constant in photon-assisted tunneling structures. However, according to our calculations, the product $g_c \cdot \tau_1$ is constant within 4% in the range of the electric field between 55 and 70 kV/cm:

$$g_c \cdot \tau_1 = A \quad , \tag{4.1.4}$$

where A [cm · s] is a constant, characteristic of the heterostructure. In addition, the cross section gain g_c is, with good accuracy, proportional to the applied voltage V between 55 and 70 kV/cm:

$$V \propto g_c \quad . \tag{4.1.5}$$

It is convenient to express the lifetime τ_1 (g_c) and $\tau_{1'}$ as a function of the cross section gain g_0 needed by an (idealized) device with zero lower state lifetime, i.e.

$$g_0 \cdot n_{tot} = \alpha_{tot} \tag{4.1.6}$$

and

$$\tilde{g} \cdot \tau_{1'} = A \quad ; \tag{4.1.7}$$

so that the ratio of $\tau_{1'}/\tau_1(g_0)$ is the inverse of the effective cross section gains $\tilde{g}/g_c$.

4.1.3 Lifetime ratio and condition for lasing

Equations 4.1.1-4.1.7 allow a prediction of the normalized L-I and V-I curves. In particular, the current density j was obtained from the lower laser state population $n_{1'}$ using $j = qn_{1'}\tilde{g}/A$. The photon flux becomes then

$$S(g_c/g_0) = \frac{g_c \cdot \tilde{g} - g_c \cdot g_0 - g_0 \cdot \tilde{g} - g_c^2}{2A \cdot g_c \cdot g_0} \quad . \tag{4.1.8}$$

The slope efficiency dP/dI is given by

$$\frac{dP}{dI} = N_p h\nu \alpha_m \frac{dS}{dJ} \quad , \tag{4.1.9}$$

where N_p is the number of periods, $h\nu$ is the photon energy and α_m are the mirror losses. The current density below threshold ($S = 0$) can be expressed as

$$j_b(g_c/g_0) = \frac{n_{tot} \cdot q}{A}\left(\frac{\tilde{g} \cdot g_c}{\tilde{g} + g_c}\right) \quad , \tag{4.1.10}$$

and the current density above threshold is

$$j_a(g_c/g_0) = \frac{n_{tot} \cdot q}{A}\left(\frac{\tilde{g} \cdot (g_c - g_0)}{2 \cdot g_c}\right) \quad . \tag{4.1.11}$$

The total current density is therefore $j(g_c/g_0) = max(j_b, j_a)$. Inversely, the cross section gain g_c over g_0 can be expressed as a function of the current density, below threshold, as

$$g_c^b/g_0 = \frac{\tilde{g}j}{g_0\left(\frac{n_{tot}q}{A}\tilde{g} - j\right)} \quad , \tag{4.1.12}$$

and above threshold as

$$g_c^a/g_0 = \frac{n_{tot}q\tilde{g}}{n_{tot}q\tilde{g} - 2jA} \quad . \tag{4.1.13}$$

The total cross section gain, which is proportional to the bias voltage, is therfore $g_c/g_0 = min(g_c^b/g_0, g_c^a/g_0)$. The result of this model is plotted in Fig. 4.3 for different values of the ratio $\tilde{g}/g_0$. For large values of the ratio $\tilde{g}/g_0$ (thus for low lower state lifetimes), the change in differential conductance at threshold is clearly visible and the laser exhibits a large slope efficiency. If we use for the ratio $\tilde{g}/g_0$ in our model values less than 6, we observe the somewhat surprising fact that lasing is not possible. In fact, the limit value for the ratio $\tilde{g}/g_0$ is obtained by imposing $S(g_c/g_0) > 0$. In other words, a ratio of at least $\tilde{g}/g_0 > 3+2\sqrt{2}$ ($\simeq 5.8$) is required to make such a laser operational (independently of A).

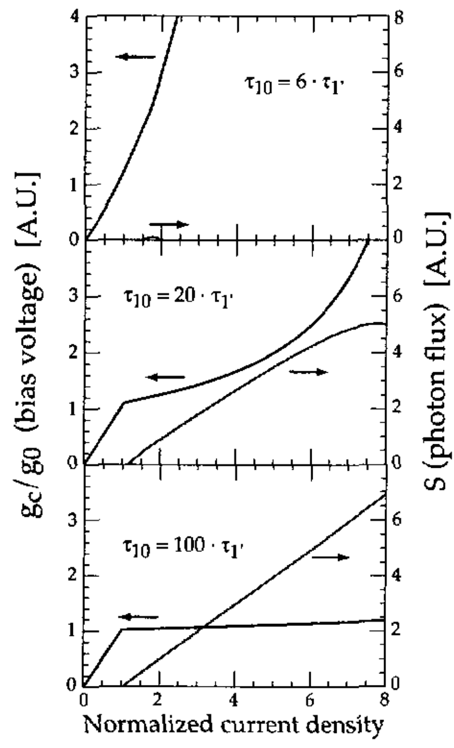

Figure 4.3: V-I and L-I curves computed by the model for three different values of $\tau_{10}/\tau_{1'}$, i.e. of $\tilde{g}/g_0$. Lasing is impossible if the lower state lifetime is longer than 6 times the upper state lifetime at the g_0 threshold.

This sensitivity to the lower state lifetime has its origin in a kind of positive feedback loop. As the lower state lifetime is increased, the population on this state increases and therefore decreases the population of the upper state (since the total population is conserved, see Eq. 4.1.1). The increase of gain needed to overcome this decrease in population difference can only be obtained at the cost of a further reduction of the upper state lifetime. This fact has important consequences for the design of high performance QC lasers based on photon-assisted tunneling transition.

In Fig. 4.3 (particularly visible for $\tilde{g}/g_0 = 20$), we observe also a saturation of the photon flux accompanied by an increase of the differential resistance, as observed experimentally [106]. This is the result of a strong reduction of the effective upper state lifetime due to stimulated emission ($\tau_{1tot}^{-1} = \tau_1^{-1} + \tau_{st}^{-1}$). The saturation of the photon flux can be deduced analytically by demanding $dS(g_c/g_0)/dg_c = 0$. Using formulae 4.1.8 and 4.1.11, we can calculate the value of the current density for which the photon flux is maximum (assuming $d\tilde{g}/dg_c = 0$):

$$j(S_{max}) = \frac{n_{tot}q}{2A} \cdot (\tilde{g} - \sqrt{\tilde{g}g_0}) \quad . \tag{4.1.14}$$

Computing analytically the ratio of the differential conductances just below G_b and just above G_a threshold, we obtain, assuming that $g_c \sim g_0$ and $\tilde{g} \gg g_0$, that this latter is roughly half of the ratio of the lifetimes:

$$\frac{G_b}{G_a} \sim \frac{1}{2}\frac{\tilde{g}}{g_0} = \frac{1}{2}\frac{\tau_{10}}{\tau_{1'}} \quad , \tag{4.1.15}$$

where τ_{10} is the $n = 1$ state lifetime at a bias corresponding to a gain g_0, i.e. $\tau_{10} = A/g_0$. The inset of Fig. 4.4 displays the exact solution (solid curve) and the approximation of Eq. 4.1.15 (dashed curve) for a ratio of the conductance G_b/G_a between 0 and 15.

4.1.4 Comparison with experiment

We are then able to deduce the lower state lifetime by measuring the ratio of the conductances below and above threshold. Looking at the V-I curves of all measured lasers (as for example in Fig. 4.2 and 4.8), we determined the ratio of the lifetimes $\tau_1/\tau_{1'}$ from the ratio G_b/G_a (using the exact solution displayed in the insert of Fig. 4.4) and the threshold current density.

We then calculated the lower state lifetime for each laser using the fact that

$$\tau_{1'} = \frac{n_s \cdot q}{j_{th}} \cdot \frac{g_0}{\tilde{g}} \quad , \tag{4.1.16}$$

where $\tau_1 = n_s \cdot q/j_{th}$. The Fig. 4.4 shows the value of $\tau_{1'}$ calculated by this method as a function of the threshold current density for several measured lasers. One obtains a mean value of $\tau_{1'} = 2.6$ ps. The uncertainty of these points is a result of both the intrinsic uncertainty for n_s and the fact that n_s is not the exact value of the density of the state 1.

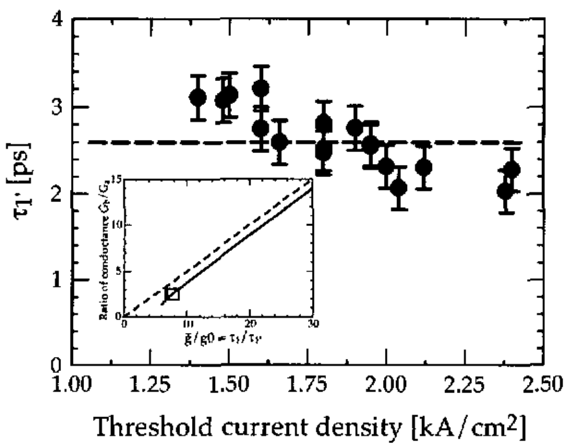

Figure 4.4: Lower state lifetime $\tau_{1'}$ as a function of threshold current for several lasers, calculated using the exact solution for the ratio of the conductances G_a/G_b. Inset: exact solution (solid curve) and approximation of Eq. 4.1.15 (dashed curve). The small rectangle represents the region of the values obtained for our lasers.

The ratio between the lifetimes at threshold ($\tau_1/\tau_{1'}$) is then about 8, because τ_1 is approximatively equal to 20 ps in this structure [71]; this is enough for lasing, but much smaller than for previous lasers based on the same photon-assisted tunneling transition at lower wavelength (more than 40 for example for D2190) [71]. The small rectangle in the inset of Fig. 4.4 represents the region of the values obtained for our lasers.

The density of state 1 and the current flowing through the structure allow us to determine the lifetime $\tau_{1'}$ of this $n = 1$ state. With the values of this lifetime as a function of the electric field, we are then able to simulate the transport characteristics (V-I curves) of the structure. We took into account the phonon absorption and the population decrease of state 1 at higher temperature by populating the higher states including the first excited state 2' (see Fig. 4.1). Indeed, the electroluminescence spectra show an intensity increase of the 2'-1' vertical transition with temperature (see below and Fig. 4.11); thus the current due to this 2' state gets important at high temperature and therefore becomes an important current leakage channel. We assumed also an injection time into this 2' state of twice the lifetime of the state itself (about 1.2 ps), changing the population of the state 2' by a ratio of 2. We calculated the current and the population of state 1 by iteration taking into account the population of the lower state $n_{1'} = j \cdot \tau_{1'}/q$. As explained above, the non zero lifetime of this lower state has been deduced from the ratio of the lifetimes at threshold (calculated to be about 2.6 ps). We calculated the current density vs. voltage for different temperatures and compared them with the experimental curves measured on the electroluminescence sample (see below), as shown in Fig. 4.5. Good agreement with the experimental curves was obtained after dividing the calculated current by 1.17. An adjustment of the current was also performed in Ref. [71], and is probably due to an uncertainty of the doping level and/or the injection barrier thickness.

Since the gain cross section g_c is

$$g_c = \frac{4\pi q^2 z_{11'}^2 \Gamma}{\varepsilon_0 n L_p (2\gamma) \lambda} \quad , \tag{4.1.17}$$

the different quantities used in the model can be related to the material properties. In Eq. 4.1.17, $\lambda = 10.1\mu m$ is the emission wavelength, $n = 3.2$ the material's refractive index, $\Gamma = 0.52$ the modal overlap factor, ε_0 the vacuum permittivity, $L_p = 31.6$ nm the period thickness, $z_{11'}$ the matrix element of the laser transition and $(2\gamma) = 12$ meV the full-width at half-maximum of the luminescence peak (see below). α_{tot} are the total losses (waveguide, α_w, and mirror, α_m, losses: $\alpha_{tot} = \alpha_w - \frac{1}{L} ln(R)$, where R = 0.26 is the facet reflectivity and

L the cavity length). The peak material gain is then $G_p = \frac{g_c}{\Gamma}(n_1 - n_{1'})$.

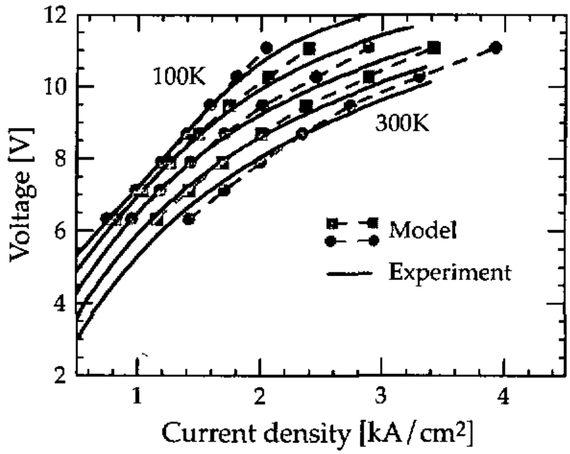

Figure 4.5: V-I curves of luminescence sample at different temperature (respectively 100, 150, 200, 250 and 300K) with corresponding calculated curves.

The calculated matrix elements of the transition at different electric fields allow us to determine the gain cross section g_c of the device. In a second step, we calculated the peak net modal gain $G_M = g_c(n_1 - n_{1'})$ for different temperatures as a function of the current, taking into account the density of state n = 1' as well. The result of these calculations is shown in Fig. 4.6 for different temperatures between 0 and 300K. We observe a gain saturation for $T > 180K$. This explains the abrupt degradation of the laser performance for temperatures above 150K. Indeed, by using the threshold condition (Eq. 4.1.3), we could calculate the threshold current density. QC lasers with the same waveguide at 11.5 μm and about 10 μm exhibited waveguide losses of $\alpha_w = 74$ cm^{-1} and $\alpha_w = 40$ cm^{-1} respectively [105, 74]. Assuming a value for α_{tot} (= G_M at threshold) of 57 cm^{-1} (dashed curve in Fig 4.6), we get a $I_{th}(T)$ dependence which is in good agreement with the experimental data as shown in Fig. 4.7. Assuming mirror losses of $\alpha_m = 6.4$ cm^{-1} (with $L = 2.1$ mm of the device shown in Fig. 4.7 with squares), we find waveguide losses of about $\alpha_w = 50.6$ cm^{-1}. A discussion about these waveguide losses with measurements using the Hakki-Paoli method will be presented in the Sec. 4.1.6.

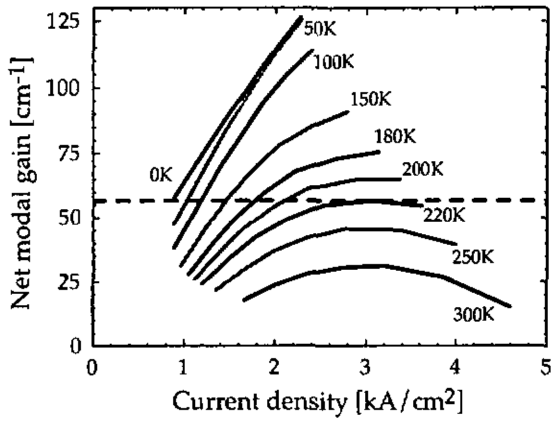

Figure 4.6: Peak net modal gain $G_M = g_c \cdot (n_1 - n_{1'})$ derived by the model as a function of the current density. The dashed curve represents the total losses of our device (57 cm^{-1}) used in Fig. 4.7.

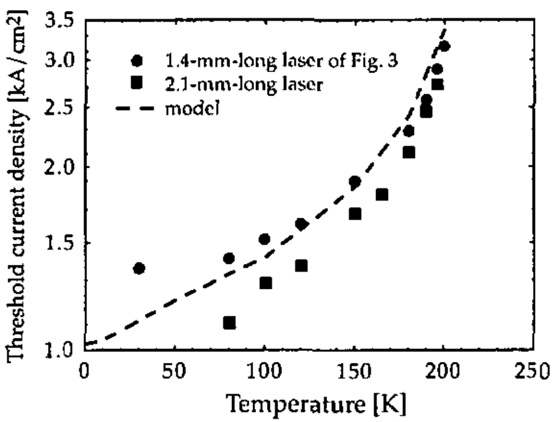

Figure 4.7: Comparison between threshold current density measured on two different lasers and calculated (dashed line) for the 2.1-mm-long laser with $\alpha_{tot} = 57$ cm^{-1}.

The experiments show an abrupt increase of the threshold current above T = 150K which is well predicted by our model. The model also predicts that laser action stops at 220K while experimentally a maximum operating temperature of 200K was observed. Therefore room-temperature operation is not possible with this structure. To get higher maximum temperature operation, we need to decrease the lifetime of the downstream $n = 1'$ state and increase the energy of state 2' (i.e. increase the energy difference between state 1 and 2'). We expect that such changes in the laser design should improve the performance of the laser.

4.1.5 Continuous-wave and spectral analysis

The spectra of the laser in pulsed mode are strongly multimode. In continuous-wave (CW), the spectrum slightly above threshold is monomode, with a measured linewidth limited by the resolution of our spectrometer (0.1 cm^{-1}). When increasing the electric field, the device becomes multimode. CW L-I curves are shown in Fig. 4.8 for a 0.782 mm-long, 18μm-wide buried heterostructure device.

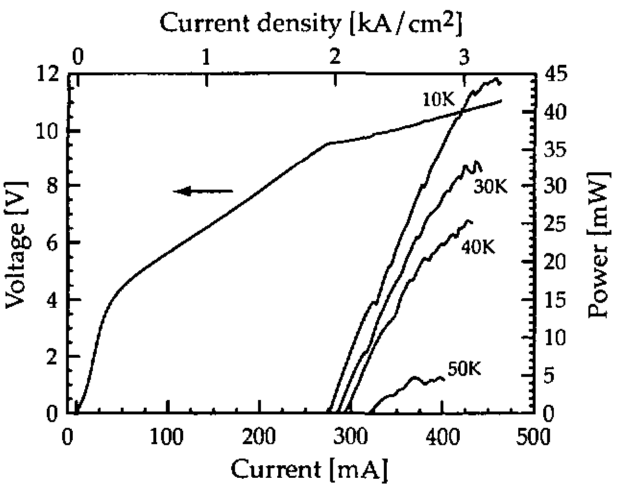

Figure 4.8: L-I curves in continuous wave of a 0.782mm-long, 18μm-wide buried heterostructure laser at four different temperature with a V-I curve at 10K.

Indeed such a device give really better performances in continuous-wave than the devices processed in the standard way (see Sec. 3.5). The laser operates up to 50K with a maximum output power of 45 mW at 10K from a single facet measured by a powermeter. The threshold current is $I = 280mA$, corresponding to a threshold current density of $J_{th} = 1.99kA/cm^2$ which is higher than in pulsed mode because of heating of the active region.

In order to measure the linewidth of the laser with higher accuracy, we used a confocal-planar Fabry-Pérot resonator in an open-loop measurement. The distance between the two mirrors is 16.8 cm, resulting in a free spectral range of about 0.9 GHz and a minimal full width at half maximum (FWHM) of the resonance peak of $\delta\nu \sim 2$ MHz. The latter value was calculated using a reflectivity of the mirrors of R $\sim$ 99.3 % at 10.1 μm. As shown in Fig. 4.9, we have been able to detect a linewidth of $\sim$ 3.9 MHz on the device shown in Fig. 4.8 driven with a current of 306 mA (corresponding to 2.2 kA/cm^2) in continuous-wave. The linewidth obtained is only twice the limit of the setup. QCL linewidths in the kilohertz level have been accomplished by using electronic servo techniques frequency [107].

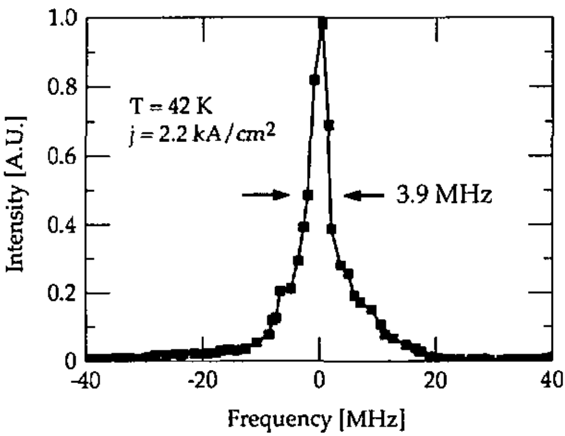

Figure 4.9: High resolution Fabry-Pérot spectrum of the device shown in Fig. 4.8 driven in continuous-wave at a current of 306 mA (corresponding to 2.2 kA/cm^2) and at a stabilized temperature of 42 K. The FWHM obtained is only 3.9 MHz. The origin of the frequency axis is coincident with the emission wavelength of 10.1 μm.

4.1.6 Waveguide losses

We obtained waveguide losses on the order of 50 cm^{-1} by comparing the threshold current density temperature dependence of our laser with the model (Sec. 4.1.4). We can also determine these waveguide losses experimentally using the Hakki-Paoli technique [108]. This technique allows to evaluate the gain below threshold through high-resolution measurements of the Fabry-Pérot oscillations in the luminescence spectra. We use in fact a technique based on the analysis of the Fourier transforms of subthreshold emission spectra (interferograms). This method takes into account both shape and contrast of the Fabry-Pérot fringes, and is therefore superior to the classical Hakki-Paoli technique [109].

Starting from the interferograms of the high-resolution luminescence spectra, this technique measures the peak net modal gain minus waveguide losses $G_M - \alpha_w$ or net gain. We performed these measurements in continuous-wave. The 0.782 mm-long, 18 μm-wide buried heterostructure laser whose performance has already been shown (Fig. 4.8) was used for these measurements. The results are reported in Fig. 4.10 where the net gain is displayed for different increasing injected currents. The plot of the peak net gain versus injected current density j shows a linear dependence with a slope $\Gamma g = 64.5\mathrm{cm/kA}$, where $g = \frac{G_M}{\Gamma j} = \frac{g_c(n_1-n_{l'})}{\Gamma j}$ is the gain coefficient. The extrapolation at $j = 0$ yields waveguide losses of 111.8 cm^{-1}, which is much larger than the 50 cm^{-1} deduced by the model.

This large discrepancy could have several reasons. First, the waveguides of the investigated lasers are not identical. The waveguide of the laser used for the comparison with the model is a standard waveguide with a ternary top cladding, while the one of the laser used in the Hakki-Paoli measurements is symmetric with two InP cladding layers (one of them regrown). But the use of two different waveguides cannot explain such a big difference in the waveguide loss. Another reason could be either that current and gain are not linearly depending on each other or that the mathematical analysis itself has a problem, mainly because of an inaccuracy in the measurement of the background. An additional, but non-negligible, possibility is the current-depending lifetime of the lower state which leads to an increasing re-absorption at low current densities. This effect was not taken into account in the calculations.

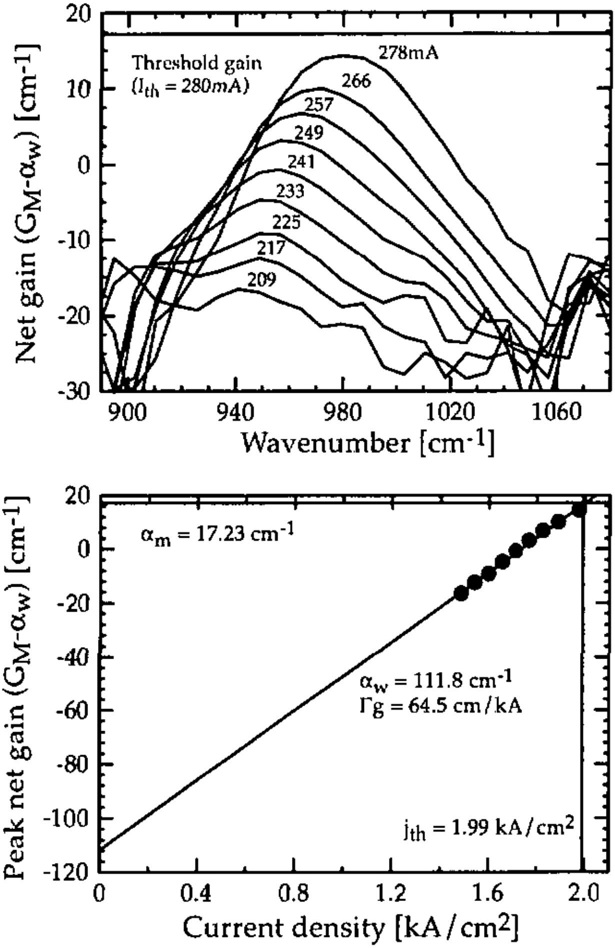

Figure 4.10: (Upper) Peak net modal gain measurements using the Fabry-Pérot fringes of the luminescence spectra in continuous-wave for increasing current (Hakki-Paoli measurements). The temperature is 10 K and the measurements were performed on the device shown in Fig. 4.8. (Lower) Peak net gain $G_M - \alpha_w$ as a function of the current density.

Indeed, we considered a constant lower state lifetime, but we can observe a small overall change as a function of the threshold current density in Fig. 4.4, leading to an approximative value of 4 ps by extrapolating at zero current. The ground state population is thus large enough to enable residual intersubband absorption from the ground state to the excited states. This effect leads to an over-estimation of the waveguide loss using the Hakki-Paoli measurements.

4.1.7 Electroluminescence and tuning

The intersubband electroluminescence was investigated as a function of applied electric field in order to study the nature of the photon-assisted tunneling transition. Luminescence spectra performed at 80 K for different voltages are displayed in Fig. 4.11. A strong first-order Stark-shift is easily observable due to the interwell 1-1' transition. This is because of the large spatial difference $z_{11} - z_{1'1'}$ between the center of the electron probability distribution of states 1 and 1'. The measured electroluminescence peak shifts from 13.38 μm at low current densities (4.9 V)to 9.27 μm at 13.0 V. The second peak observed in the electroluminescence spectra at high bias is due to the vertical interwell transition 2'-1' in the 7.4 nm-wide well. The third peak is attributed to a transition between miniband states. The full-width at half maximum of the luminescence peak is about 12 meV. This is significantly larger than the one observed for a vertical transition structure at similar wavelengths ($\sim$ 8 meV) [110]. The reason for this broadening is that diagonal transitions are more sensitive to interfacial roughness than vertical ones (see Appendix C).

The inset of Fig. 4.11 plots the measured transition energy $E_{11'}$ of the electroluminescence peak as a function of the voltage. The Stark-shift of this transition can be written as $\Delta E_{11'} = q\Delta F[z_{11} - z_{1'1'}]$, where q is the electron charge and ΔF is the increment of the electric field in the region between states 1 and 1'. ΔF can be expressed as $\Delta V_p/L_p$ where ΔV_p is the voltage increment across one period (here $V/50$) and L_p is the thickness of one period (31.6 nm). From the data of the inset of Fig. 4.11 between V = 6.3 V and V = 13V, we deduce a value of 7 nm for $z_{11} - z_{1'1'}$. At low bias, the experimental Stark-shift deviates slightly from the straight line due to the screening regime where the electron charge progressively transfers from the doped regions into the $n = 1$ state [71].

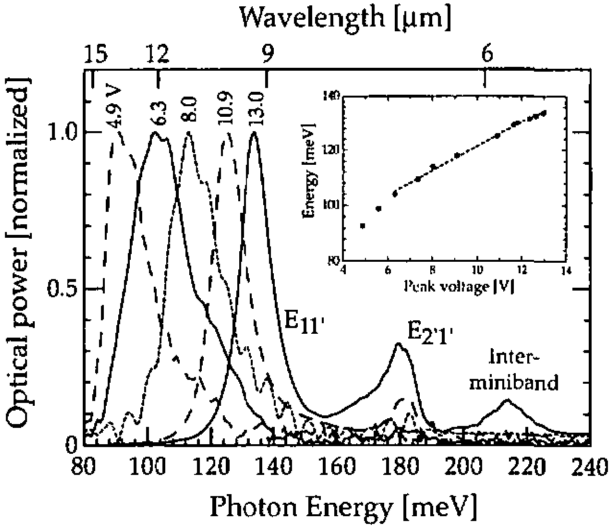

Figure 4.11: Intersubband electroluminescence spectra at 80K between 4.9 and 13.0 V. The transition energies are labeled by the states numbering in Fig. 4.1. The inset shows the position of the electroluminescence peak as a function of applied voltage. The dashed line is a linear fit between 6.3V and 13V which yields a value of 6.97 nm for $z_{11} - z_{1'1'}$.

We also tested the electrical tuning behavior of these lasers [71, 74]. The top contact metallization consists of two segments of equal length (0.75 mm) separated by a small gap. We are then able to inject different current densities J_1 and J_2 (and thus different voltages V_1 and V_2) in each section; this allows us to adjust electrically the laser photon energy towards large energies. In Fig. 4.12, the electrical tuning of a 1.5-mm-long laser at 80 K in pulsed mode with two sections of equal length is presented. For this measurement, the current I_1 in the first section was set to some arbitrary value and the current I_2 in the second section was increased until threshold. We measured also the voltage in each section; this is shown in Fig. 4.12 as well. The tuning range obtained for this laser is about 85 cm^{-1} (9.47 μm to 10.31 μm). We observed thus a tuning factor of $\frac{\Delta\lambda}{\lambda} = 8.3$ %. This value is larger than the ones seen in other structures based on the same photon-assisted tunneling transition: 6% at 6 μm [71], 3% for a bidirectional laser at about 6.5 μm [111], or even 4% for an anticrossed transition at 10 μm [74]. However, the last result was measured close to room-temperature, which makes the laser very suitable for spectroscopy of liquids.

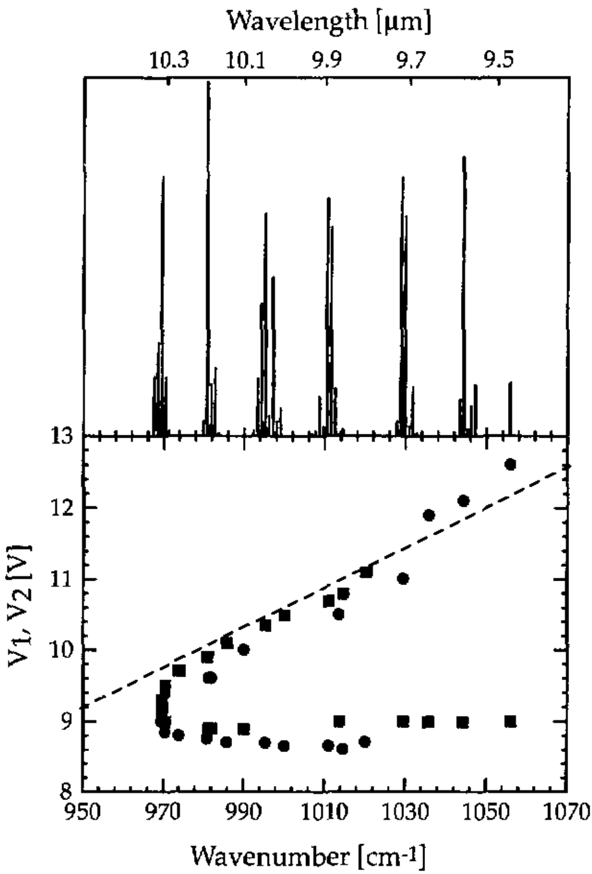

Figure 4.12: Laser tuning at 80 K at threshold showing a tuning range of 85 cm^{-1} corresponding to $\Delta\lambda/\lambda \sim 8\%$. (a) Representative spectra at different currents. (b) Voltage in the two sections vs. lasing energy. The dashed curve shows the Stark tuning observed in the electroluminescence measurements (see Fig. 4.11).

4.1.8 Conclusion

We have shown modeling of QC lasers based on a photon-assisted tunneling transition taking into account a finite lifetime of the lower state of the laser transition. This tunneling escape time is about 1 ps computed under the assumption that the injection region behaves as a continuum, and was then often underestimated and considered to be zero in the models used until now. In fact, we found in this work that the escape time is 2.6 ps, which is much longer than 1 ps. This was already shown by Faist *al.* [112]. The new value found for the lower state lifetime is therefore not negligible and is important for all designs, in particular for the three-quantum well active region, since ultimately the populations of the lowest states are extracted into the injection/relaxation region by a tunneling process. This long escape time can create an effective bottleneck effect [113] and therefore decreases the performance of the lasers. On the contrary, no bottleneck is foreseen in a superlattice active region (see Appendix C.3), since transport in the lower miniband provides a very efficient electron extraction. Nevertheless, the injection efficiency is not optimum in these superlattice active regions, and is less efficient than for the three-quantum well design.

These considerations led recently to the proposition and experimental demonstration of new designs which combine the advantages of the resonant tunneling injection feature of the three-quantum well design and the electron extraction efficiency of the superlattice design. These new approaches are based on a bound-to-continuum transition [114] or on two-phonon resonances [115] (see Fig. 4.13).

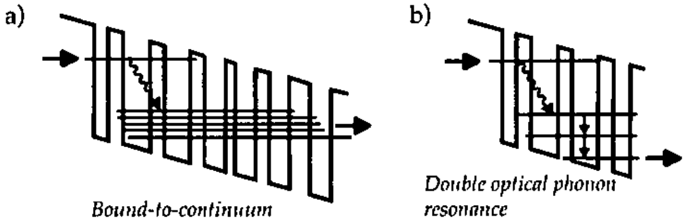

Figure 4.13: New designs recently demonstrated. The active regions are based on bound-to-continuum or two-phonon resonances.

In both cases, one uses the high injection efficiency into the upper state of the transition provided by the fact that the upper state wavefunction penetrates significantly into the injection barrier (three-quantum well active region characteristic). In the bound-to-continuum design, a high extraction efficiency is achieved by having the lower state of the transition belonging to a miniband, whereas the high extraction efficiency of the two-phonon resonances design is obtained by spacing the lowest three levels by an optical phonon energy each [113]. Significantly better performances than the traditional design based on the three-quantum well active region have been obtained with these two new designs, promising useful room-temperature applications using quantum cascade lasers. Continuous-wave operation at 39°C with few milliwatts of optical power has recently been demonstrated using the two-phonon resonances design [11].

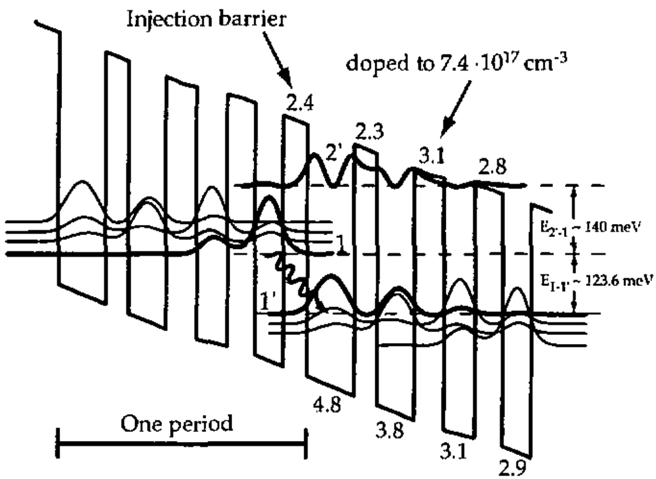

Figure 4.14: Self-consistent computation of the energy band diagram of two periods of the InGaAs/InAlAs structure S2007 under an average applied electric field of about 75 kV/cm. The thickness of the different layers is indicated in nanometers.

Another result obtained in this work is the good agreement between theory and experiment for the voltage vs. current density and the threshold current density vs. temperature characteristics. To eventually obtain lower threshold current and pulsed mode operation up to room temperature, instead of only 200 K, we have to decrease the lifetime of the downstream state and design the structure in such a way to increase the energy difference between the state 1 and 2'. This will avoid a population of state 2' with hot electrons. We designed and grew such a structure (sample S2007) in which this energy difference is more than 140 meV, compared to about 60 meV in the laser structure S1548, as shown in Fig. 4.14.

L-I and V-I curves in pulsed mode of a 1.875mm-long, 28μm-wide laser are displayed in Fig. 4.15 for four different temperatures.

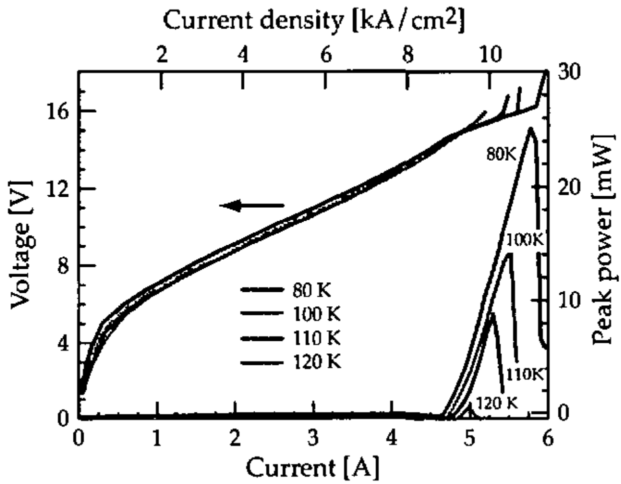

Figure 4.15: L-I and V-I curves in pulsed mode of a 1.875mm-long, 28μm-wide laser S2007 based on the new design at four different temperatures.

The performance is not as high as predicted. Indeed, using our model, we predicted room-temperature operation (see the prediction of the peak net modal gain for this structure in Fig. 4.16) and this laser operates only up to 120 K with a voltage threshold much larger than expected. A 3 mm-long laser worked up to 200 K. The high threshold voltage causes the NDR observed in the V-I curves, which corresponds to a dramatic breakdown of the laser. At this point, electrons are injected in higher states and the structure is no longer well aligned. Another problem, which was not taken into account, is the re-absorption into the upper lasing state. Indeed, at voltages slightly above the predicted threshold voltage (already at 80 kV/cm), the energy differences between states 1 and 1' (the transition energy) and states 1 and 2' become roughly the same, leading to a substantial re-absorption. This re-absorption decreases again if the field becomes larger than 110 kV/cm. The corresponding voltage of 14 V is approximately the threshold voltage observed at 80 K. Given this design bug, it is nevertheless surprising that lasing operation was obtained in this structure.

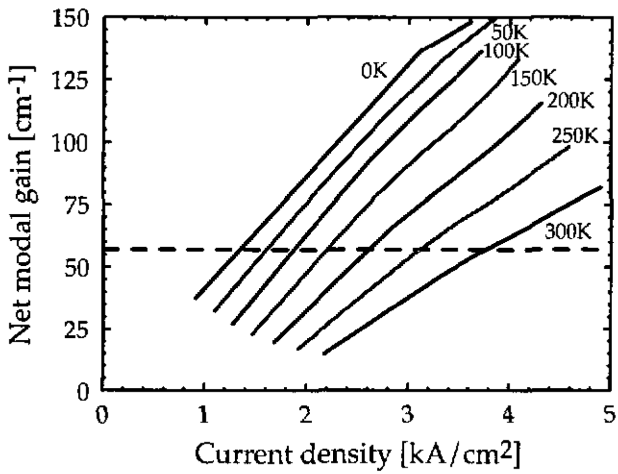

Figure 4.16: Peak net modal gain $G_M = g_c \cdot (n_1 - n_{1'})$ derived by the model as a function of the current density for the new design S2007. The dashed curve represents the total losses of 57 cm^{-1}, as in Fig. 4.6 for laser S1548.

4.2 Measurements on a superlattice

We observed mid-infrared electroluminescence from a doped superlattice and performed measurements in which the superlattice was embedded in a waveguide to allow a comparison between the spontaneous emission and the emission amplified in a cavity.

4.2.1 Electroluminescence in a superlattice

The superlattice studied is formed by 120 periods of $Ga_{0.47}In_{0.53}As$ wells of 8 nm and $Al_{0.48}In_{0.52}As$ barriers of 3.2 nm (sample S1390). For optical characterization, the sample was processed into 150μm diameter circular mesas, instead of usual square mesas (see Sec. 3.5). In contrast to the nominally undoped sample of Scamarcio *et al.* [47], our sample is highly doped.

Luminescence spectra at different voltages show both vertical (intrawell) and diagonal (interwell) transitions, as shown in Fig. 4.17.

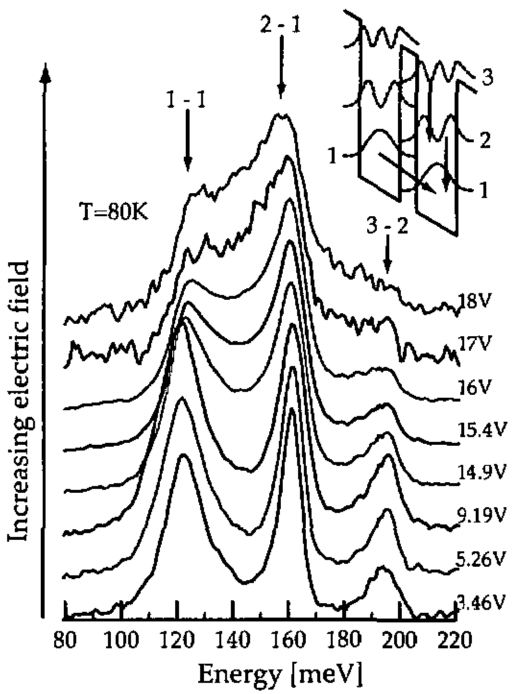

Figure 4.17: Normalized electroluminescence spectra for different applied voltage between 3.4 and 18V. The insert shows the conduction band diagram for an electric field of 100 kV/cm. The three arrows indicate the three different transition observed in the electroluminescence spectrum.

The luminescence spectra consist of three peaks. The first peak centered at an energy of about 120 meV is identified as the diagonal interwell transition between the lowest Wannier-Stark states of two adjacent wells ($1 \rightarrow 1$, see inset of Fig. 4.17). A first-order Stark-shift is easily observable for this transition between 107 kV/cm (14.3 V) and 130 kV/cm (17.5V) as shown in Fig. 4.18. However, for small electric fields ($<$ 100 kV/cm), the transition energy is almost constant, which is explained by the formation of spatial field domains with different electric fields, where only a portion of the structure is electric field tilted. The observed Stark-shift is weaker as expected by a simple calculation of the diagonal (interwell) 1-1 transition corresponding to $E_{11} = eFd$, where $d = 11.2$ nm, or even with taking into account the anticrossing which occurs between the ground state and the first excited state of the next well.

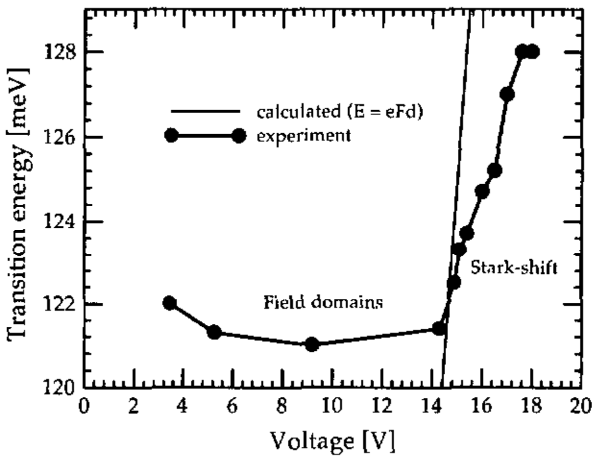

Figure 4.18: Transition energy as a function of the applied voltage for the diagonal (interwell) transition. The straight line represents the calculated linear Stark-shift.

The second peak is identified as the vertical (intrawell) transition between the first excited state $n = 2$ and the ground state $n = 1$; its measured photon energy of 160 meV corresponds well to the calculated value of 166 meV. The third peak centered at 195 meV is identified as the vertical (intrawell) transition between the second excited state $n = 3$ and the first excited state $n = 2$, in agreement with the calculated value of 196 meV. The linewidths of the two vertical intrawell transition are narrower than that for the interwell diagonal transition, which is a characteristic of the intersubband transitions. As already mentioned above (Sec. 4.1.7), this is due to the fact that the diagonal transitions are more sensitive to interface roughness.

4.2.2 Measuring gain in a superlattice

Electromagnetic gain in an inversionless, strictly periodic superlattice has been calculated using the semi-classical miniband picture by Ktitorov *et al.* [116] and Ignatov *et al.* [38]. The dispersive AC conductivity, which corresponds to gain below and absorption above the Bloch frequency, has yet to be demonstrated, although it has been clearly demonstrated that Bloch oscillations couple to an external terahertz radiation [117].

We present a technique which allows the investigation of the superlattice gain profile by comparing the spontaneous emission $L(\omega)$ and the emission amplified in a cavity $G(\omega)$ measured on a superlattice embedded in a waveguide. A red-shift between both emissions should indicate a dispersive Bloch gain.

To obtain a laser structure, we regrow an InP top cladding (2 μm n-doped to 1 x 10^{17} cm^{-3} and 1 μm n-doped to 8 x 10^{18} cm^{-3}) onto the active region by Metal Organic Chemical Vapor Deposition (MOCVD). Thus the optical waveguide is formed by the InP substrate on one side and by the InP cladding on the other side. The wafer was then processed like a laser into ridge waveguides of 28 μm width by wet chemical etching. One facet was polished at a 45° angle, but only on half the substrate thickness. This way, the light could be coupled out of the structure either by the facet (with passing the waveguide) or by the 45° angle (as for luminescence experiment) as shown in Fig. 4.19.

Optical measurements are then performed on these laser stripes. Fig. 4.20 (upper) shows the signal measured either by the facet $G(\omega)$ or by the 45° angle $L(\omega)$ at 4.2 K. We find two differences between both emission profiles. The peak corresponding to the diagonal (interwell) transition between the WS states is indeed slightly red-shifted by about 2 meV. In addition, the emission peak which is attributed to the vertical (intrawell) transition between first excited and ground state is strongly suppressed.

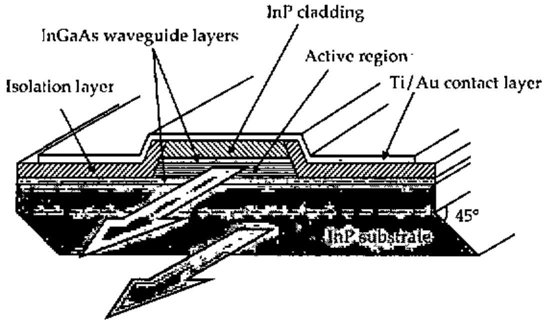

Figure 4.19: Schematic drawing of a laser stripe with the polished 45° angle facet.

The experimentally observed red shift can be explained by investigating the interplay of three phenomena that might be responsible for the observed difference of the emission from the waveguide (facet) and the 45° angle, i.e., the waveguide losses, the re-absorption of the emission into the first excited state and the intra-miniband absorption (Bloch gain). The waveguide losses, assumed to be dominated by free-carrier absorption, are calculated using the following relation [34]:

$$\alpha_{wg}(\omega) = \frac{C}{(\hbar\omega)^2}, \tag{4.2.18}$$

where the constant $C \sim 0.479$ eV cm^{-1} for our structure. For the re-absorption into the excited state, assuming that this state is empty, we use a Lorentzian-shaped absorption spectrum, i.e.:

$$\alpha_{12}(\omega) = \omega \frac{e^2}{\epsilon_0 n_r c} z_{12}^2 \frac{\gamma_{12}}{(\hbar\omega - \hbar\omega_{12})^2 + \gamma_{12}^2} \frac{n_s \Gamma}{d}, \tag{4.2.19}$$

where $z_{12} = 1.9$ nm is the dipole matrix element, $2\gamma_{12} = 14$ meV the full width at half maximum (FWHM) of the measured transition, $n_r = 3.2$ the real part of the refractive index, c the speed of light, $d = 112$ Å the superlattice period and $\Gamma = 0.5$ the confinement factor. This re-absorption also results in a red-shift of the peak corresponding to the diagonal transition.

The intra-miniband absorption, or Bloch gain, can be deduced from the linear component of the AC conductivity [38, 118]:

$$\alpha_B(\omega) = \frac{1}{\varepsilon_0 n_r c} \Re \left[\frac{ne^2 \tau_p}{m^{SL}} \frac{I_1(\Delta/2kT)}{I_0(\Delta/2kT)} \cdot \frac{1 - i\omega\tau_\epsilon - \omega_B^2 \tau_\epsilon \tau_p}{(1 + \omega_B^2 \tau_\epsilon \tau_p)(\omega_B^2 \tau_\epsilon \tau_p + (1 - i\omega\tau_p)(1 - i\omega\tau_\epsilon))} \right] \tag{4.2.20}$$

where $\omega_B = eFd/\hbar$ is the Bloch frequency, Δ the miniband width, τ_ϵ^{-1}, τ_p^{-1} the energy and momentum relaxation rates, $m^{SL} = 2\hbar/\Delta d^2$ the effective mass at the bottom of the miniband and I_n are the modified Bessel functions.

The theoretical curves for $G(\omega)$ and $L(\omega)$ are shown in Fig. 4.20 (Lower). The theoretical shift of $G(\omega)$ due to the different absorption mechanisms of the originally gaussian luminescence signal $L(\omega)$ with a measured FWHM $2\gamma_{11} = 16$ meV is given by:

$$G(\omega) = L(\omega) \cdot \frac{1}{L} \int_0^L dz \cdot e^{-(\alpha_{wg}(\omega) + \alpha_{12}(\omega))z} \, , \tag{4.2.21}$$

where the Bloch contribution has been neglected at first.

With a cavity length of $L = 0.83$ mm, we obtain a total shift of -2.52 meV due to the re-absorption, whereas the contribution from waveguide losses are negligible. Thus, the experimental value of -2 meV can be already explained by the re-absorption of the signal by the intrawell transition from the strongly occupied ground state into the almost empty excited state. The re-absorption suppresses the high-energy shoulder of the diagonal transition and thus pushes the luminescence signal towards lower energies. A more detailed investigation including the Bloch gain $\alpha_B(\omega)$, Equ. 4.2.20 calculated for a temperature of 80 K, reveals that the red-shift due to this Bloch gain amounts to only a small fraction (~ -0.4 meV) of the red-shift due to the re-absorption [118]. In addition, we do not observe the predicted shoulder at about 125 meV in $G(\omega)$ (dashed curve in Fig. 4.20), which is a signature of the dispersive Bloch gain.

In conclusion, this technique is indeed sensitive to gain/loss mechanism in waveguide heterostructures. In a superlattice, field domains are always accompanied by a more or less pronounced anticrossing of ground and adjacent excited states, which leads to an inevitable re-absorption. Thus, it is questionable if it is possible to obtain a stable superlattice structure with little re-absorption.

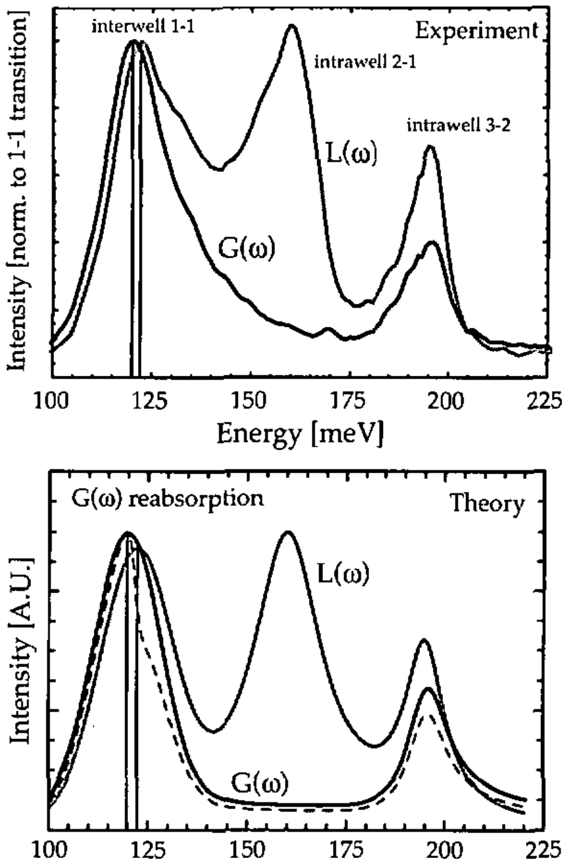

Figure 4.20: (Upper) Experimental at 4.2 K and (Lower) theoretical electroluminescence spectra (normalized to the 1-1 diagonal transition signal for the experimental results) for the signals coming from both the facet ($G(\omega)$, black curve) and from the 45° ($L(\omega)$), gray curve) for a current of 1.2A, at 4.2 K. The shift of the peak due to the 1-1 transition is clearly resolved. The dashed curve represents the theoretical $G(\omega)$ curve taking into account the red-shift due to the Bloch gain $\alpha_B(\omega)$.

4.3 Superlattice in magnetic field

4.3.1 Motivation: superlattice laser

The energies of the Wannier localized states in a superlattice are subbands separated in energy by eFd and show a parabolic dependence in k-space of the dispersion relation, as shown in Fig. 4.21 a). As explained in Sec. 2.7.2, the main effect of a magnetic field applied parallel to the layers is to shift the subbands one according to the other by the quantity k_{shift}. This applies obviously to superlattices as schematically shown in Fig. 4.21 b).

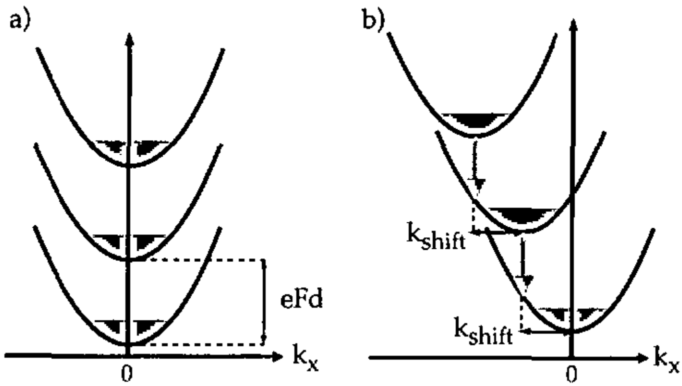

Figure 4.21: Dispersion relation of a superlattice (a) without magnetic field and (b) with a magnetic field applied parallel to the layers.

The optical transitions between a Wannier-Stark state ν and a second one $\nu+1$ occurs between occupied states if there is no applied magnetic field. The motivation of the study of diagonal transitions in magnetic field comes then from the fact that a high enough k_{shift} allows the electrons of the subband ν to reach unoccupied states of the $(\nu+1)$-subband. A population inversion could be created simply by putting a superlattice into a parallel magnetic field. In the same way, one could imagine to obtain a superlattice-laser.

In fact, the theoretical situation is relatively complicated if a magnetic field is applied parallel to the layers on quasi two-dimensional electron systems; in this case, we end up with a crossed electric and magnetic field system (see Sec. 2.7.2). Numerous studies have been done for such conditions: theoretically [91, 119] as well as experimentally (see for example [120, 121, 122]).

4.3.2 Magnetic field electroluminescence of a superlattice

This idea incited us to perform electroluminescence spectra of our superlattice under applied parallel magnetic field. As shown in Fig. 4.22 for spectra at a constant voltage of 14 V and at 30 K, the diagonal (interwell) 1-1 transition is strongly quenched by increasing parallel magnetic field in contrast to the expected behavior.

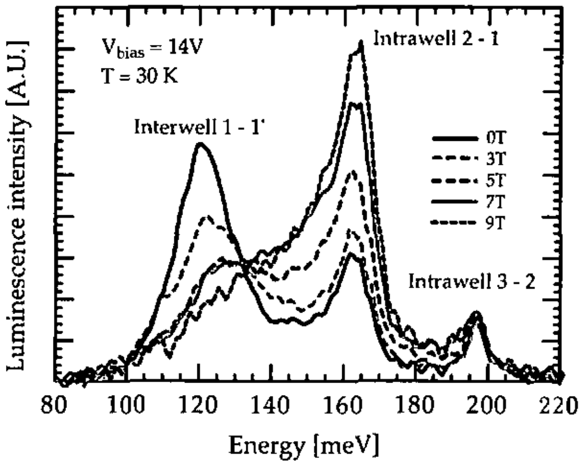

Figure 4.22: Electroluminescence spectra of a superlattice at a constant voltage of 14 V for different applied parallel magnetic field between 0 and 9 T.

Moreover, the vertical (intrawell) 2-1 transition is on the contrary increased in magnetic field, while the vertical (intrawell) 3-2 transition seems to be unchanged. So the basic idea of the superlattice laser in parallel magnetic field seems not to work. To be sure, it would be useful to do the same measurements on a superlattice embedded in a waveguide identical to the one used for the measurements presented upper in the text (Sec. 4.2.2).

4.4 Quantum cascade lasers in parallel magnetic field

Following the latter measurements performed on the superlattice, which are difficult to explain because of the three different transitions observed are relatively important (see Fig. 4.22), we present in this section experimental measurements investigating the influence of a magnetic field applied parallel to the layers on our QC laser S1548 based on photon-assisted tunneling transition. This laser shows also the vertical (intrawell) transition 2-1, but with a strongly reduced intensity (see Fig. 4.11). Therefore it is more adapted for the investigation of the diagonal interwell transition in a parallel magnetic field, by studying the behavior of the intersubband electroluminescence spectra in presence of such a field.

4.4.1 Luminescence dependence of diagonal-based QC lasers

Luminescence spectra at 30K obtained at a constant voltage of 13 V for different applied magnetic fields are displayed in Fig. 4.23 a). The main peak due to the diagonal interwell 1-1' transition at about 130 meV presents three important different behaviors in function of the applied magnetic field. First, the peak has a strong quenching of its intensity. Figure 4.24 shows the decrease of the peak integral in function of the magnetic field (normalized to the zero-field value). The light intensity is proportional to the oscillator strength and therefore to the squared transition matrix element. This latter seems to strongly decrease in a parallel magnetic field. We made computation of the energy band diagram and matrix elements of the transition taking into account the effects of the parallel magnetic field by inserting the hamiltonian in our model. The values of the transition matrix elements calculated by this model are shown by the dashed curve in Fig. 4.24. They decrease significantly less than the experimental results.

The peak exhibits also a broadening and a small blue-shift of the transition energy. In contrast, besides the broadening, our model predicts a red shift of the emission, as shown in Fig. 4.23b). Here we made the assumption that the matrix element of the transition is constant. This explains why the peak intensity does not change in the simulation. Measurements performed at 10 V and at 200 and 300K at 13V have shown the same decrease of the peak integral of the luminescence peak, as shown in Fig. 4.24. This effects seem to depend neither on bias nor on temperature.

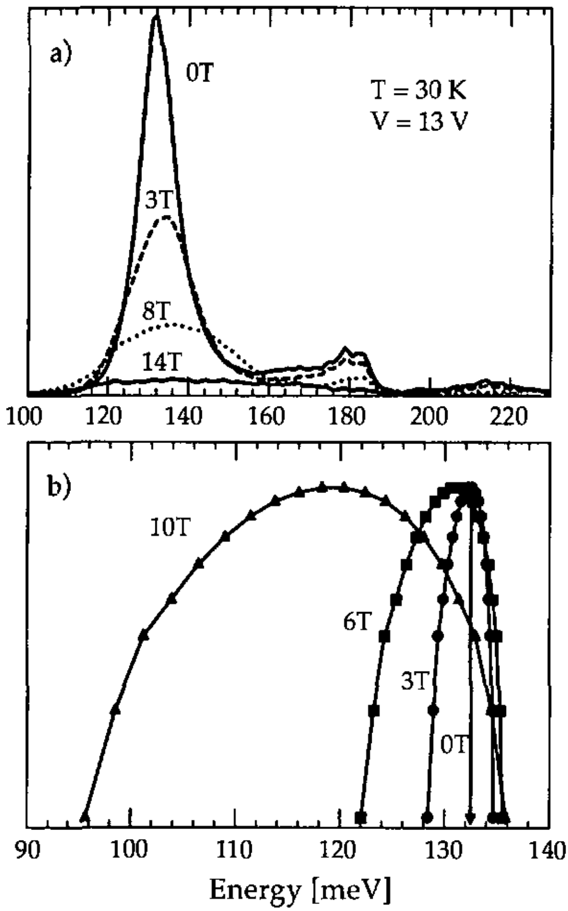

Figure 4.23: a) Luminescence spectra at 30 K for different applied parallel magnetic fields at a voltage of 13 V and b) simulated luminescence spectra predicting a broadening and a red-shift of the peak.

We performed the same measurements on a structure with has an identical design, but which is five times less doped (sample S1672). Roughly the same three behaviors were seen.

Luminescence spectra performed at 30 K and 150 K are shown in Fig. 4.25.

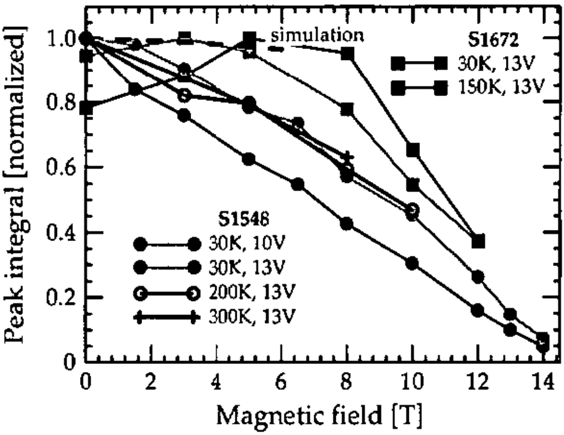

Figure 4.24: Peak integral as a function of the applied parallel magnetic field for structures S1548 (circles and crosses) and S1672 (squares) for different temperatures and voltages. Simulation is shown by the dashed curve.

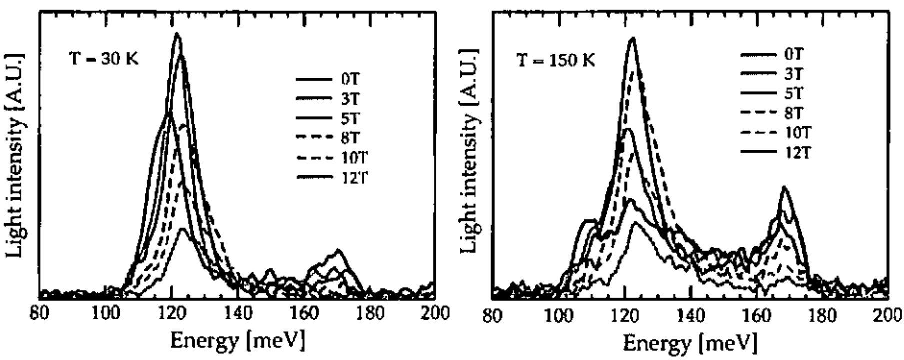

Figure 4.25: Luminescence spectra in parallel magnetic field of structure S1672 at 13 V, at 30 K (left) and at 150 K (right).

Nevertheless, we observed, before decrease of the peak integral at high magnetic field, a small increase of the intensity and a narrowing of the peak, which is more clearly visible at 150 K. Due to the weak doping ($n_s = 5 \cdot 10^{10}$ cm^{-2}), there are probably field domains present without magnetic field and the structure is stabilized by applying a parallel magnetic field. We see that the intensity of the second peak at about 170 meV decreases strongly with magnetic field. That is a signature of an electron cooling which proves that there is less current flowing across the structure. This, in turn, means that the structure is in fact stabilized by the magnetic field. Furthermore, the narrowing of the 120 meV peak between 0 and 3 T might be due to the quenching of impurity-induced transitions. Those transitions, which are produced by the weak doping, are allowed at zero magnetic field.

We see that our simple model based on single-particle theory is in relatively good agreement with the broadening of the luminescence emission, while it predicts a red-shift of the peak. This shift cannot be cancelled by many-body corrections as shown by Apalkov and Chakraborty [123], who have calculated the effect of a tilted magnetic field on our QC laser design. They arrived at the same conclusions for increasing the parallel component of the magnetic field: redshift, broadening and slight decrease of the intensity. In order to explain our experimental tiny blueshift of the emission peak, they considered the effect of the disorder due to interface roughness and due to charged impurities in the structure [124]. In both cases, they saw a large suppression of the redshift predicted for clean samples, as shown in Fig. 4.26. The emission line at high parallel magnetic field is almost at the same energy as for the zero field case. There is even a small blueshift of the peak due to band non-parabolicity in the case of disorder due to charged impurities, as shown in Fig. 4.26 b). Moreover, the intensity of the peak shows a rapid decrease in the presence of the disorder. Our experimental measurements can then be explained by the presence of disorder in the structure.

The effect of the disorder could be observed by comparing quantum cascade lasers with abrupt and with graded interfaces at the quantum wells of the active region. Indeed, luminescence measurements at both cryogenic and room-temperature have shown narrower spectra and slightly better threshold current density for a graded interface device [125]. These better performances were attributed to the changing interfacial roughness, but are still to be confirmed by investigating in details two samples grown one after the other. The measurements in a parallel field can be one of these investigations.

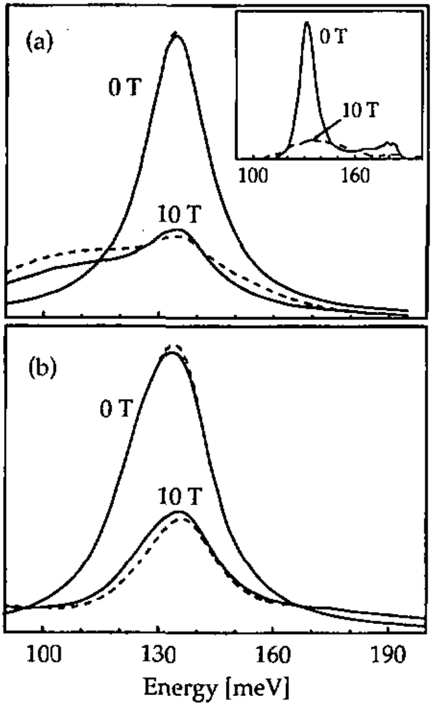

Figure 4.26: Luminescence spectra of our QC structure in the case of (a) charge-neutral impurities and (b) charged impurities in the presence of an externally applied parallel magnetic field coming from Apalkov and Chakraborty [124]. The insert shows our experimental results.

4.4.2 Dependence of the threshold current

Besides the electroluminescence study, we performed measurements of the threshold current of various QC lasers as a function of the applied parallel magnetic field. The threshold current normalized by its zero-field value as a function of the ratio of $\hbar\omega_c$ over the transition energy $h\nu$ is shown in Fig. 4.27 for six completely different lasers. We measured two lasers based on a vertical transition at about 4.6 μm (lasers D2065 and D2075 [112]), a similar laser but at about 5 μm (laser D2122 [7]), one laser based on an anticrossed transition at about 10.4 μm (laser S1397 [126]), one GaAs/AlGaAs-based anticrossed laser at 9.4 μm (laser S1543 [9]) and the laser based on a photon-assisted tunneling transition at about 10 μm (laser S1548).

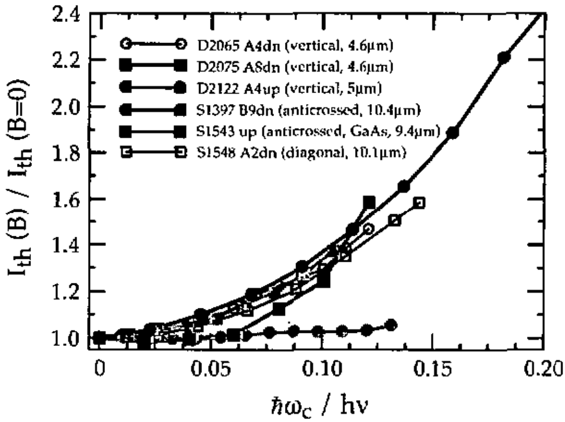

Figure 4.27: Threshold current as a function of parallel magnetic field for various QCLs.

The dependence of the threshold current is approximatively proportional to B^2 for each laser. More remarkable, their behavior scale very well together if plotted as a function of $\hbar\omega_c/h\nu$. The threshold current depends then more specifically on $\left(\frac{B\lambda}{m^*}\right)^2$. The exact reason for this behavior is not yet known.

4.5 Quantum cascade lasers in perpendicular magnetic field

If the magnetic field is applied perpendicularly to the layers, i.e. parallel to the electric field, the Hamiltonian can be separated in perpendicular and in-plane motion. The in-plane states are then localized into Landau levels, as explained in detail in Sec. 2.7.1.

In mid-infrared quantum cascade lasers, the lifetime of the upper state is controlled by optical phonon emission (see Sec. 2.5.3), which strongly reduces this lifetime. It has been proposed that a quantum dot laser could efficiently quench the optical phonon emission and therefore lower the threshold current density substantially [127, 128, 129]. Predictions range from one to many orders of magnitude reduction in the threshold current density. However, the manufacture of such a quantum dot structure for the observation of confinement effect is a difficult experimental task. It has also been proposed that a magnetic field applied perpendicular to the layer, by completely quantifying the system into Landau levels, would have the same qualitative effect [130], simulating then a quantum box laser, since the inter-subband emission should occur between Landau levels instead of subbands. This approach has already been tried for interband lasers [131].
This behavior is expected: the lifetime of the upper state will decrease (and the threshold current density increase) each time the upper state can emit an optical phonon resonantly into a Landau level, and increase in the opposite situation, since the optical phonon emission should be forbidden in this case (see Fig. 4.28).

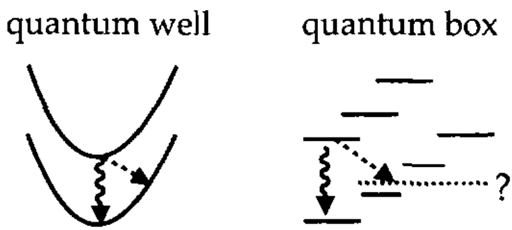

Figure 4.28: Schematic drawing of the transition in a quantum well and in a quantum box. The dashed arrows represent the possible optical phonon transitions.

The energy of the n^{th} Landau level of state i (which has the energy E_i) is given by (Equ. 2.7.21)

$$E_{l,n}(E_i) = E_i + \left(n + \frac{1}{2}\right)\hbar\omega_c \tag{4.5.22a}$$

$$= E_i + \left(n + \frac{1}{2}\right)\frac{\hbar e B}{m^*\left(1 + \frac{E_i}{E_g}\right)} \quad , \tag{4.5.22b}$$

where we took into account the non-parabolicity in the energy-dependent effective mass $m^*(E) = m^*\left(1 + \frac{E_1}{E_g}\right)$, where E_g is the material's band gap (= 0.8 eV in InGaAs), and which is valid if $(n + \frac{1}{2})\hbar\omega_c \ll E_i$. So the magnetic fields for which there is a resonance between the n^{th} Landau level of the lower state of the laser transition (of energy E_2) and the first Landau level of the upper state of the laser transition (of energy E_3) minus the optical phonon energy are simply given by the condition [1]

$$E_{L0}(E_3) - \hbar\omega_{LO} = E_{Ln}(E_2) \tag{4.5.23}$$

The threshold current of several quantum cascade lasers have been measured in a strong perpendicular magnetic field to observe these resonances. Indeed the threshold current shows maxima when a resonance with the optical phonon occurs. First, a quantum cascade laser based on a vertical transition at about 5 μm (sample D2160 [7]) was measured, but no oscillations of the threshold current were clearly seen. A second test was done on a device based on an anticrossed-transition at about 10.4 μm (sample S1397 [126]). As shown in Fig. 4.29, oscillations of the threshold current have been observed, but they cannot be explained only with the energy of the lasing transition $E_3 - E_2$.

Unfortunately for our experiment, the design used for this QC laser requires two states below the upper state of the lasing transition (states 2 and 1, see inset of Fig. 4.29), which then translate into two ladders of Landau levels and therefore into two different resonance channels. The arrows indicate the position of the resonances between states 3 and 2 (solid) and between states 3 and 1 (dashed). This decreases the average distance between Landau levels and, due to their broadening, decreases the modulation of the threshold current density. The mixing of these two scattering mechanisms (with different transition energies) in the well where the transition occurs has to be taken into account to explain the oscillations. The peak of the threshold current density at about 10 T can be explained by the simultaneous resonance between states 3 and 2 and the resonance between states 3 and 1.

[1] The energies of the states are calculated from the bottom of their own well and we take into account the energy difference between the bottom of the two wells.

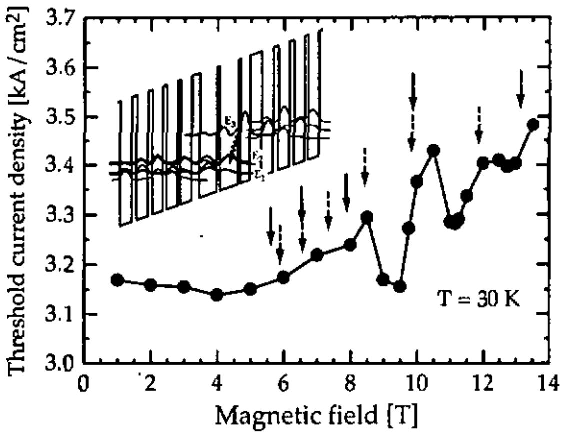

Figure 4.29: Threshold current density as a function of the applied perpendicular magnetic field for the laser S1397 based on a vertical transition at $\lambda \sim 10.4$ μm. The arrows indicate the positions of the resonances (full lines for $E_3 \rightarrow E_2$, dashed for $E_3 \rightarrow E_1$). The inset shows the energy band diagram of two periods of the structure under an electric field of 41.6 kV/cm. The laser transition occurs between state E_3 and E_2.

In order to avoid this effect, we used a structure based on a photon-assisted tunneling transition at 6μm (sample S1384, copy of sample D2190 [72]) in which there is only one state below the upper state of the lasing transition. In this way, we will have only one ladder of Landau levels to which the upper state can scatter. This should maximize the modulation of the threshold current. Oscillations of the threshold current between 9 and 14 T and a curve of the light intensity versus applied magnetic field are displayed in Fig. 4.30.

Resonances with the optical phonon, which lead to increases in the threshold current, are clearly identified in correspondence with the decrease of the emitted light. The arrows indicate the positions of the resonances calculated using Equ. 4.5.22b with an effective mass of $m^* = 0.0469m_0$ [2]. The resonance occurring at higher magnetic field corresponds to the

[2]This effective mass was obtained by fitting the value of the magnetic field of the experimental resonances as a function of the Landau level index of the lower state ($n = 7, 8, 9, 10$) with Equ. 4.5.22b.

resonance with the 7^{th} Landau level of the lower state. A smaller energy difference between the states involved in the transition should give more obvious effects, seeing that we should observe resonances with Landau levels of smaller index.

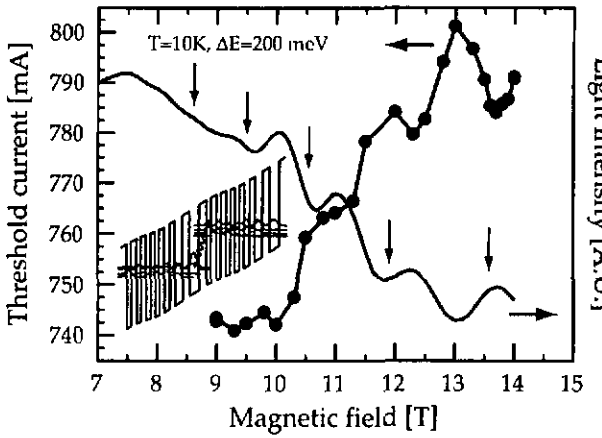

Figure 4.30: Threshold current and light intensity as a function of the applied perpendicular magnetic field for the laser S1384 based on a photon-assisted tunneling transition at 6 μm. The arrows indicate the positions of the resonances with $m^* = 0.0469m_0$ (see text). The inset shows the energy band diagram of two periods of the structure under an electric field of 79 kV/cm.

Therefore, we measured the device already well studied in Sec. 4.1 based on the photon-assisted tunneling transition transition at about 10 μm (sample S1548). Unfortunately, the measurements on this sample did not give a larger modulation amplitude of the oscillations in threshold current, although their positions are measured correctly. These oscillations are not dramatically different from those seen in the previous sample, as shown in Fig. 4.31. The arrows indicate the positions of the resonances calculated using Eqn. 4.5.22b with an effective mass of $m^* = 0.0472m_0$ [3]. It is not well understood why this experiment did not lead to a clearer result; more detailed measurements will be necessary to clarify this point.

[3]This effective mass was obtained by fitting the value of the magnetic field of the experimental resonances as a function of the Landau level index of the lower state ($n = 4, 5, 6$) with Equ. 4.5.22b.

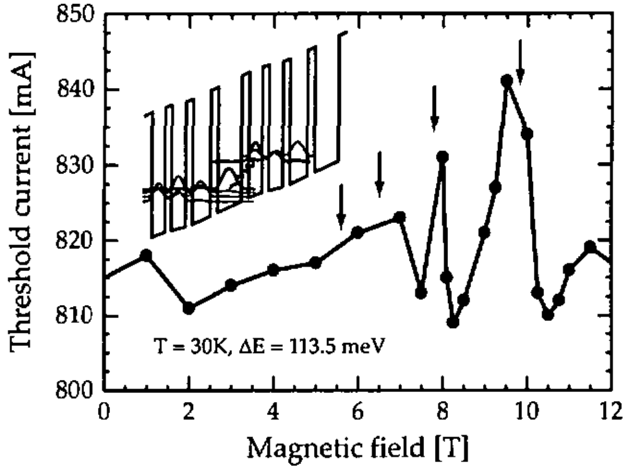

Figure 4.31: Threshold current as a function of the applied perpendicular magnetic field for the laser S1548 studied in Sec. 4.1 based on a photon-assisted tunneling (diagonal) transition at 10 μm.

Chapter 5

Far-infrared quantum cascade structures

5.1 Motivation for the magnetic field measurements

In the far-infrared, where the subband separation energy $E = h\nu$ is larger than the optical phonon energy $\hbar\omega_{LO}$, various elastic scattering processes are allowed such as scattering by ionized impurities, interface roughness scattering or electron-electron scattering, or inelastic processes such as acoustic-phonon emission (see Sec.2.5.3). With the subband energy spacing being less than the optical phonon energy, the emission of such optical phonons is forbidden, but can be extremely efficient as soon as the temperature is high enough to thermally activate electrons with a sufficiently high energy. This relaxation process becomes then again dominant at high temperature [63].

Without magnetic field, all these scattering mechanisms, in particular intersubband electron-electron scattering, can occur continuously in k-space, the energy and momentum of the carriers being conserved after the interaction. The main channel which contributes to the upper state depopulation is the 2211 process [65], i.e. an interaction between two carriers initially in the excited state which scatter into the ground state with energy and momentum conservation, as schematized in Fig. 5.1 a). This scattering is possible for a continuum of energy changes ΔE, meaning that one electron undergoes an energy change $+\Delta E$ and the other one a change of $-\Delta E$.

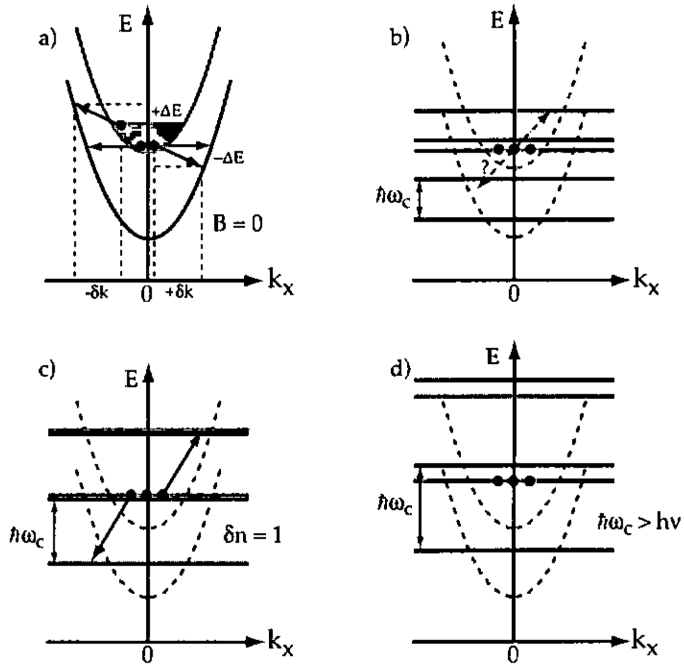

Figure 5.1: Dispersion relations in the case of a) no applied magnetic field and with an applied perpendicular magnetic field (b, c, d). The magnetic field reduces the carrier-carrier scattering b) which is almost forbidden in intermediate situations and c) allows the intersubband Landau resonances sketched here for $\delta n = 1$. d) Full quantum limit: $\hbar\omega_c > h\nu$.

We already noticed that the effect of a magnetic field applied perpendicularly to the layers on the structure leads to the appearance of the Landau levels and quantizes the in-plane states (see Sec. 2.7.1 for the theory or Sec. 4.5 for experiments in the mid-infrared). As theoretically predicted by several authors [130, 132], these Landau levels create a dramatic suppression of intersubband carrier-carrier recombination rates. This is because the only energy changes ΔE are now multiples of the cyclotron resonance energy: $N\hbar\omega_c = \Delta E$, with

N being an integer, as shown in Fig. 5.1 c). Of course discrete Landau levels exist only in ideal situations. In real structures, these Landau levels are broadened by impurities or interface roughness and carrier-carrier scattering can occur nevertheless in intermediate situations, as schematized in Fig. 5.1 b). Moreover the electron-electron scattering rate is inversely proportional to the associated change in energy and momentum [133]. So this scattering is suppressed more and more by increasing magnetic field, since the Landau levels splitting is increased. In fact, the intersubband emission should then occur between Landau levels instead of subbands, thereby efficiently quenching the non-radiative scattering mechanisms, and without being influenced by the optical phonon emission as in the mid-infrared.

The internal quantum efficiency, which is the radiative transition rate over the total rate, should increase since the latter is governed by the non-radiative scattering rates. The observation of an enhancement of the emission intensity, which is proportional to the internal quantum efficiency, is then a direct measure of the suppression of the intersubband scattering rates. This effect was first observed by Ulrich *et al.* [134] and then demonstrated in our vertical transition-based structures as shown further in the text. A lifetime increase or intersubband relaxation rate slowdown has already been observed in quasi quantum dots [135] created also by magnetic confinement, and in a three-barrier, two-well heterostructure [136].

Depending on the magnetic field, one can have intersubband Landau resonances if the Landau levels of each subband are at the same energy with a Landau level index-change $\delta n = 1, 2, 3, \cdots$ (see Fig. 5.1 c). The condition for such a resonance is given by

$$E_{trans} = \delta n \cdot \hbar\omega_c \tag{5.1.1}$$

where E_{trans} is the transition energy and $\omega_c = eB/m^*$ is the cyclotron frequency. Coherent tunneling between intersubband Landau levels with different indices is forbidden in ideal cases, but these resonances are possible due to the scattering between the Landau levels. Since the current should increase in such resonant situations due to the scattering mechanisms being more efficient, magneto-transport measurements should allow the observation of such resonances in the variation of the current (or the voltage) as a function of the magnetic field. If the magnetic field is strong enough, i.e. when the cyclotron energy is higher than the intersubband transition energy (at about 9.3 T for GaAs system and 5.9 T for InGaAs system for $h\nu = 16$ meV), we are in the so-called full quantum limit and we simulate the ultimate quantum box structure, as shown in Fig. 5.1 d).

Transport in superlattices in perpendicular electric and magnetic fields has been the subject of many investigations [137, 138, 139] and these resonances have been first observed by Canali *et al.* [140, 141] in an undoped GaAs/$Al_xGa_{1-x}As$ superlattice structure. They called them Stark-cyclotron resonances due to the Wannier-Stark-Landau localization of the electronic states in the superlattice. Liu *et al.* have obtained similar results in sequential resonant tunneling through Landau levels measurements [142].

The goal for the far-infrared quantum cascade structures was to investigate their behavior under the application of a strong perpendicular magnetic field and to observe the effects discussed just above: current decrease, lifetime increase, light intensity enhancement, intersubband Landau resonances,... First, we will present the experimental results obtained on vertical transition-based (intrawell) QC structures, followed by magneto-transport measurements performed on a chirped superlattice. Then we will present measurements performed on two different photon-assisted tunneling transition-based QC structures. The first one gave broad electroluminescence peaks and we used magneto-transport measurements to confirm that the electronic spectrum was due to the diagonal transition. The second structure used the conclusion of the analysis of Sec. 2.6 and was designed to prevent hot electrons doing vertical transitions in the active region-well.

5.2 Vertical transition-based structures

5.2.1 Structures

We studied two vertical transition-based (intrawell) structures, based on either InGaAs/InAlAs lattice matched to an n^+-InP substrate (sample S1431) or GaAs/AlGaAs lattice matched to a n-doped GaAs substrate (sample S1774). In fact the GaAs-based structure is a copy of the first design which gave far-infrared electroluminescence [12], but with a higher doping that enables large injection currents (the NDR appears here at $j = 150\mathrm{A/cm^2}$ at low temperature). Compared to diagonal (interwell) transitions, the vertical transition has the advantage of large oscillator strength and a narrower linewidth since it is less influenced by interface roughness, as we will see below. Both structures consist of 35 periods of four quantum wells separated by thin tunnel barriers. As in mid-infrared conventional quantum cascade structures, each period consists of an undoped active region, in which the spontaneous emission occurs, and a graded-gap injector. Both structures have been designed to emit approximatively at the same wavelength (around 15-16 meV). The calculated band structures and thicknesses of the different layers are presented in Fig. 5.2.

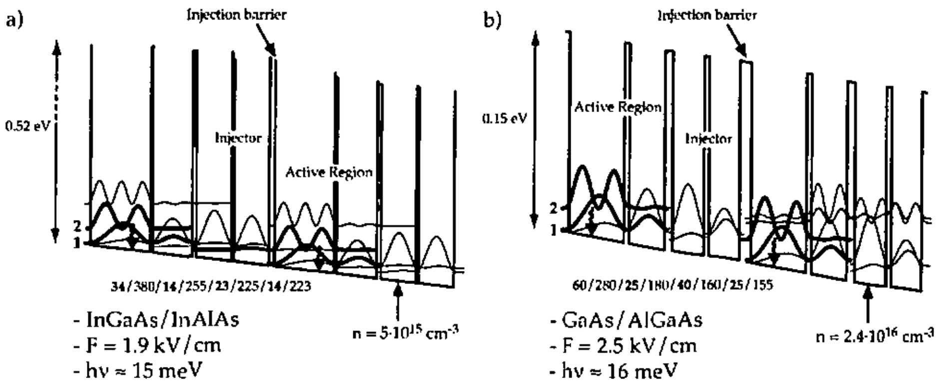

Figure 5.2: Energy band diagrams of two periods of the FIR vertical transition-based structures a) in $In_{0.53}Ga_{0.47}As/In_{0.52}Al_{0.48}As$ material under an average applied electric field of 1.9 kV/cm and b) in $GaAs/Al_{0.15}Ga_{0.85}As$ material under an average electric field of 2.5 kV/cm. The conduction band offset is respectively 0.52 eV and 0.15 eV for InGaAs and GaAs material systems. Shown are the moduli squared of the relevant wavefunctions. The wavy line indicates the transition responsible for electroluminescence emissions between state 2 and 1. The layer sequence of one period is indicated in nanometers.

The electroluminescence and magneto-transport measurements were performed with the superconducting magnet and using the InSb detector (see Sec. 3.2 and Appendix D). For the electroluminescence measurements, we applied electrical pulses between top and back contact at 6 kHz repetition rate and at a duty cycle of 50 %. For the magneto-transport measurements, we applied a continuous voltage on 220 $\mu m \times 220$ μm samples and measured the current while sweeping the magnetic field between zero and 14 T.

5.2.2 Electroluminescence spectra in magnetic field

The electroluminescence spectra at a constant current of the two vertical transition-based structures ($I = 40$ mA for InGaAs sample and $I = 100$ mA for GaAs sample) are displayed in Fig. 5.3 for different applied magnetic fields.

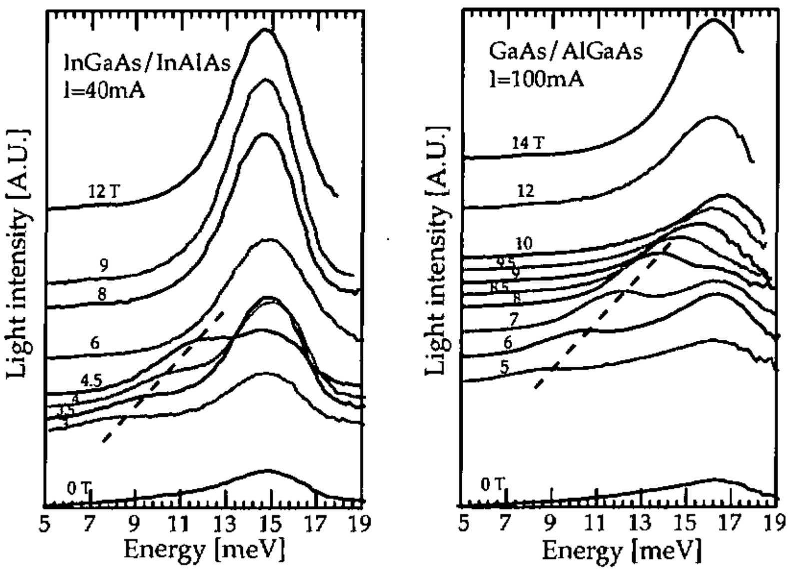

Figure 5.3: Electroluminescence spectra at 3K for different applied magnetic fields on both vertical transition-based structures. The curves are vertically displaced for clarity. The dashed curves indicate the peaks due to cyclotron emission.

We observed an increase of the luminescence intensity for both materials. The light intensity normalized to the zero field value is displayed for both materials in Fig. 5.4 as a function of the magnetic field (L-B curves). These measurements show an increase by a factor of almost 6 in InGaAs at 12 T and almost 5 in GaAs at 14 T. An additionnal peak which tunes linearly with applied magnetic field is also observed in Fig. 5.3 (dashed curves); it corresponds to the cyclotron emission of the samples. Electron injection into the excited Landau level is suppressed when the cyclotron energy is larger than the intersubband transition energy, quenching the cyclotron emission as observed experimentally.

This enhancement of the light intensity for vertical transition-based structures indicates that the non-radiative lifetime of the upper state of the transition increases with applied magnetic field, if we consider that the radiative lifetime should remain constant. At low temperature, this non-radiative lifetime was measured to be 11 and 14 ps for InGaAs and GaAs respectively [63]. That means that the lifetime increases up to 66 ps at 12 T for InGaAs and up to 70 ps at 14 T for GaAs.

The width of the intersubband peak seems to be narrowed by about 30% for InGaAs and about 20% for GaAs under application of magnetic field (see Fig. 5.3). But that is not the true narrowing of the intersubband emission because the resulting spectrum is broadened by the intrinsic linewidth of the InSb detector. The experimental data are a convolution between the detector's impulse response and the intersubband transition peak. Using a laser [14] as a probe of the InSb intrinsic linewidth (deduced to be 2.8 meV), we have convolved this response function with the expected unbroadened lorentzian shape intersubband spectrum, obtaining an estimate of the narrowing due to the field roughly equal to 60% (in respect to the zero field value). Since, for the tested structure, the linewidth at zero magnetic field measured in a vacuum FTIR is 1 meV, we can claim that the real linewidth at high magnetic field is only on the order of 0.4 meV. This zero field measured intersubband linewidth is too large to originate from lifetime broadening (0.06 meV $= \frac{\hbar}{e\tau}$) of the upper state whose lifetime is estimated to about 14 ps [63]. Consequently we cannot attribute the observed linewidth narrowing in magnetic field to the increase in intersubband lifetime. However, the measurements are consistent with a picture where the intersubband linewidth originates from intrasubband scattering events that are efficiently quenched by the magnetic confinement. In Fig. 5.4, we see that the light intensity increases in an oscillatory manner. These oscillations are due to the intersubband Landau resonances (see Equ. 5.1.1). Minima in the L-B curves correspond to maxima in the current (or minima in the voltage) vs. magnetic field curves, since an increase of the current corresponds to an increase of the non-radiative scattering. The vertical dashed curves in Fig. 5.4 indicate the positions of such resonances calculated using $m^* = 0.0427$ for InGaAs and $m^* = 0.067$ for GaAs. There is a good agreement with the observed experimental resonances except for the resonance occurring at high field corresponding to $\delta n = 1$ (around 5.5 T for InGaAs and around 9 T for GaAs).

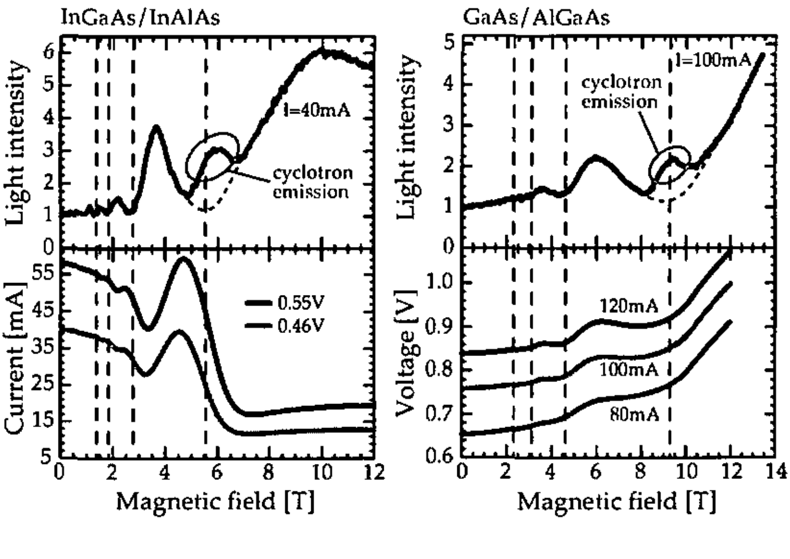

Figure 5.4: Upper: Light intensity as a function of the magnetic field for both vertical transition-based structures. The intensity is normalized to the zero field value. Lower: current (or voltage) vs magnetic field curves.

To understand this effect, we have displayed the respective positions of the intersubband and cyclotron emissions as a function of the magnetic field in Fig. 5.5. The cyclotron emissions of the two different materials are in good agreement with the theoretical values calculated with an effective mass of $m^* = 0.067$ for GaAs and $m^* = 0.0427$ for InGaAs (dashed curves in Fig. 5.5). At the energies where the intersubband and cyclotron transitions energies are approximately the same, we observed an effect of repulsion between them. In a perpendicular magnetic field, Landau and intersubband confinements are only coupled in the presence of elastic scattering events. This coupling will also lead to the repulsion between the cyclotron and intersubband emissions, with an energy scale given by the strength of the scattering. It is therefore not a surprise that the energy level repulsion observed in Fig. 5.5 is on the order of the linewidth of the intersubband peak (of 1 or 2 meV measured in the FTIR). At the magnetic fields corresponding to this repulsion effect, the cyclotron emission overlaps with the intersubband emission which is at its minimum. The dashed curves in Fig. 5.4 show the expected behavior of the intersubband emission intensity, suppressing the cyclotron emission. So, based on the repulsion observed in Fig. 5.5 and the additional unexpected resonance in Fig. 5.4, we can conclude that this resonance must be due to cyclotron emission.

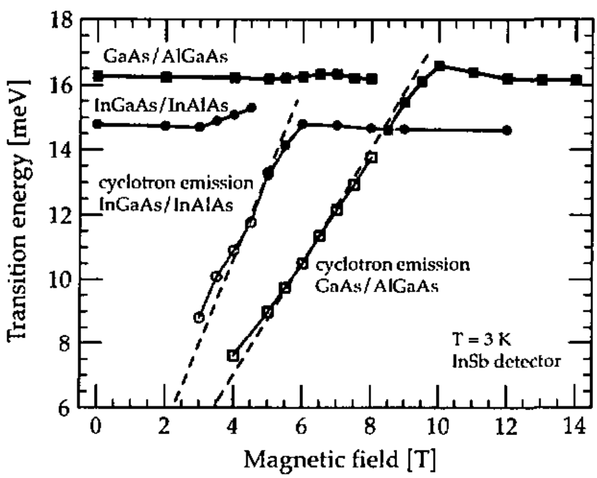

Figure 5.5: Intersubband and cyclotron transition energies of the electroluminescence spectra in function of the magnetic field. The dashed curves indicate the theoretical values of the cyclotron emission for both materials using $m^* = 0.067$ for GaAs and $m^* = 0.0427$ for InGaAs.

5.3 Superlattice structure

Graded superlattice quantum cascade lasers have shown high operation performance in the mid-infrared above the reststrahlen band energy [143, 4] (see Sec. C.3). We applied the same technology, i.e. emission between minibands in a chirped superlattice, for terahertz intersubband emission. This type of structure has the advantage that the applied electric field is compensated by a gradually varying SL and flat minibands can be obtained without dopants.

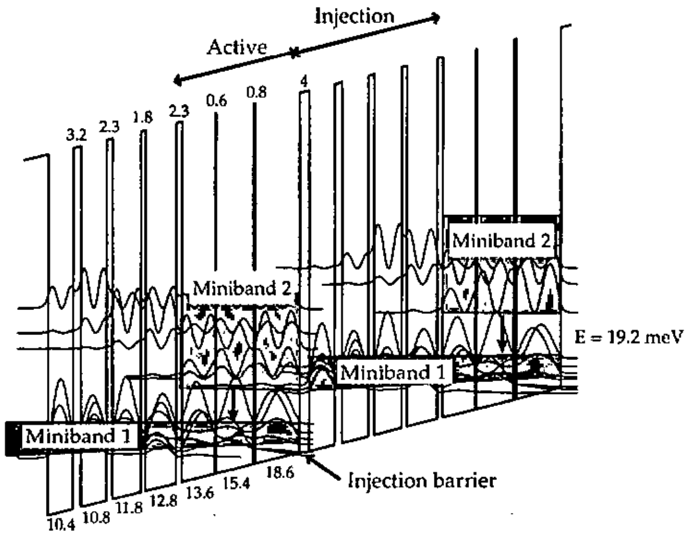

Figure 5.6: Energy band diagram of two periods of the superlattice structure under an average applied electric field of 2.5 kV/cm. Shown are the moduli squared of the relevant wavefunctions and the minibands. The thicknesses of the wells and barriers are given in nanometers.

Our structure, which has been realized in the GaAs/AlGaAs material system[1] consists of 120 periods embedded in a waveguide based on a double-plasmon structure [101, 102] formed by

[1] This structure was grown in Cambridge (*UK*) by the Cavendish Laboratory's group.

the Al metallic contact grown in-situ in the MBE system on the upper side and a heavily n doped ($n = 5 \times 10^{18}$ cm^{-1}) GaAs layer on the other. A schematic band diagram is shown in Fig. 5.6. One period of our structure consists of a four well injector and a three well active region leading in both cases to two well-defined minibands. The injector's lower miniband is matched to the active region SL's upper miniband through a 4.0 nm injection barrier. The expected terahertz emission should be dominated by a pronounced peak near the wavelength corresponding to the minigap between the second and the first miniband. We have computed this value to be close to 19.2 meV (corresponding to a wavelength of 64 μm).

For the experiments, the samples were processed into 500 μm-wide stripes of various lengths between 220 and 880 μm. The samples were powered by trains of 2 μs long current pulses providing an overall duty factor of 45 % at a frequency of 413 Hz. The light was then collected by an off-axis parabolic mirror, sent through a home-built Fourier transform infrared spectrometer (FTIR) under vacuum (principle identical to the one presented in Sec. 3.2) and detected by the liquid-helium cooled Si bolometer to perform spectra; the entire light pass was under vacuum. Representative spectra taken at $T = 10$ K are displayed in Fig. 5.7.

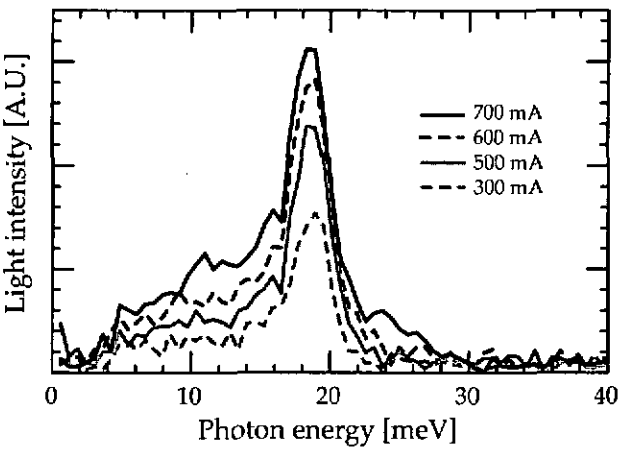

Figure 5.7: Optical spectra of the emitted radiation for different injected currents between 300mA and 700mA for a 220 μm-long waveguide.

They show that the luminescence spectrum consists of one main peak centered at a photon energy of 18.8 meV for a 220 μm-long waveguide. This is in good agreement with the calculated transition energy of 19.2 meV. The linewidth of the peak is relatively narrow ($\Delta\nu$ = 3 meV).

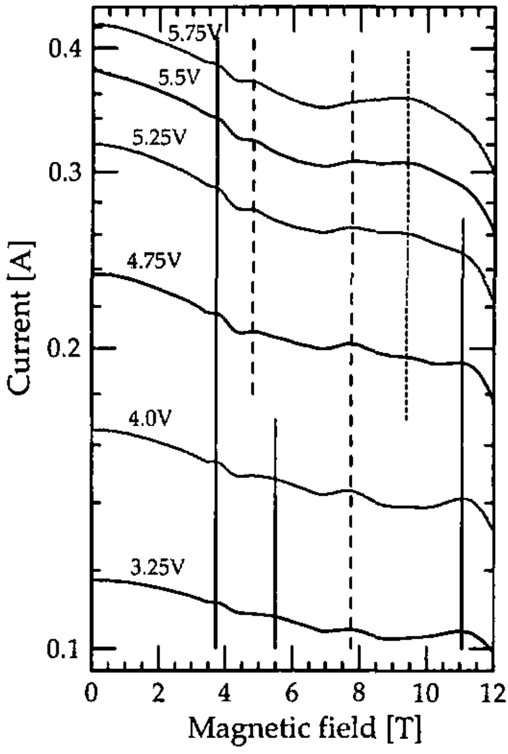

Figure 5.8: Current vs. magnetic field curves for a 880 μm-long waveguide taken at 6 different voltages. The different resonances are indicated by the vertical lines for the three different transitions (see text).

To measure this transition energy using a different technique, we used, as already explained, the magneto-transport measurements, i.e. the behavior of the current as a function of the magnetic field. These I-B curves are displayed in Fig. 5.8 for a 880 μm-long waveguide taken at 6 different voltages. The intersubband Landau resonances are clearly resolved. The solid lines indicate the resonances of the lower state of the upper miniband with the upper state of the lower miniband (radiative transition) with $\delta n = 1$ (around 11 T), $\delta n = 2$ (around 5.5 T) and $\delta n = 3$ (around 3.7 T). The dashed lines indicate the resonances of the lower state of the upper miniband with a state in the center of the lower miniband with $\delta n = 2$ (around 7.7 T) and $\delta n = 3$ (around 4.8 T). The dotted line, finally, indicates one resonance, with $\delta n = 2$ (around 9.4 T), of the lower state of the upper miniband with the bottom of the lower miniband. Considering these resonances, we can derive the transition energy using Equ. 5.1.1.

Figure 5.9 a) shows, for the three different transitions, the comparison between transition energy vs. voltage curves derived from the spectra and the one obtained from the intersubband Landau resonances with $\delta n = 1, 2$ and 3. The transition energies resulting from the calculations are also displayed for each transition. Figure 5.9 b) shows the active region of the structure at 2.5 kV/cm. The arrows indicate the three different transition energies ($E_4 - E_3 = 19.2$ meV, $E_4 - E_2 = 25.5$ meV and $E_4 - E_1 = 31.7$ meV) observed in the magneto-transport measurements. We see that there is a very good agreement between the transition energies deduced from magneto-transport measurements and calculations as well as with the electronic spectra for the radiative transition $E_4 - E_3$. In conclusion, we have demonstrated that the observed terahertz luminescence occurs through an electronic transition between the upper and the lower miniband of the structure.

The same superlattice active region was grown in a different waveguide structure. This waveguide [144], which is similar to the single-plasmon waveguide used for long-wavelength mid-infrared QC lasers [101], relies on the confinement provided by the interplay between a metallic reflection at the top metallization and the quasi-metallic confinement provided by a thin (0.3 μm thick) heavily doped ($n = 2 \times 10^{18}$ cm^{-3}) buried contact. This makes a much lower computed value of the waveguide losses than the double-plasmon waveguide. Even if the overlap factor has decreased, the figure of merit Γ/α_w is about four times larger for the buried contact waveguide than for the double-plasmon waveguide. With such a device, a pronounced linewidth narrowing was observed and lasing threshold was reached at a current density of 210 A/cm^2 [14]. Köhler *et al.* have also shown laser action in a similar structure [13].

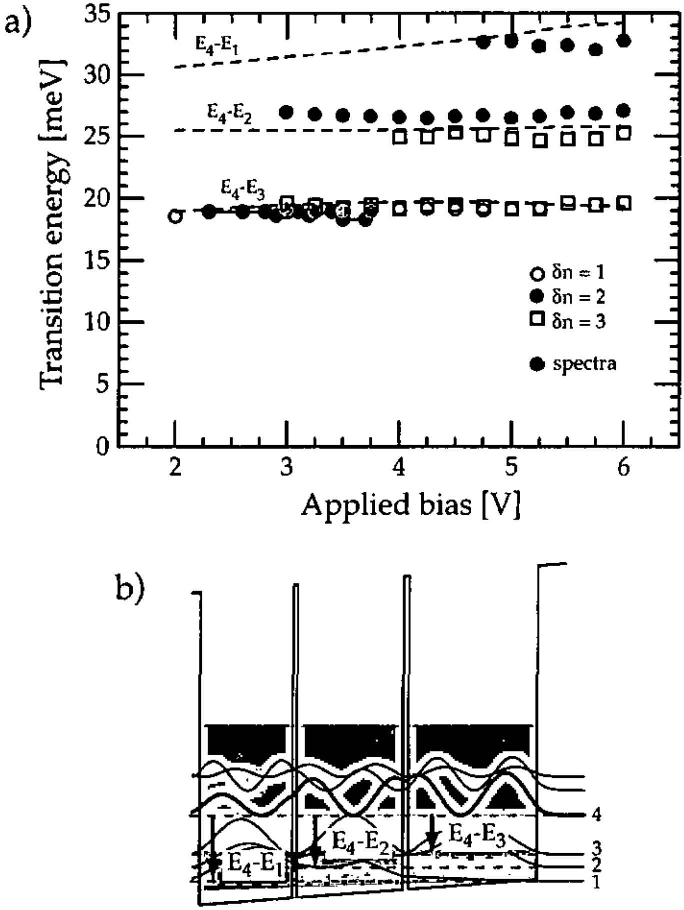

Figure 5.9: (a) Transition energies vs. voltage derived from the intersubband Landau resonances and for the calculations for the three different transitions observed corresponding to $E_4 - E_3$, $E_4 - E_2$ and $E_4 - E_3$. The electronic spectra of the radiative transition $E_4 - E_3$ are also displayed (full black circles). (b) Active region with the three different transitions observed in magneto-transport.

5.4 Diagonal transition-based structures

We studied two different structures based on photon-assisted tunneling transitions. They are also called diagonal or even interwell transitions as already discussed in the previous part of this thesis. First of all, we will present results obtained on a three-quantum well structure, including emission spectra and magneto-transport measurements. The emission spectra were relatively broad and we used the intersubband Landau resonances to confirm the diagonal behavior of the transition. Then we will show improved emission spectra obtained from a five-quantum well structure which has been designed differently taking into account the results of Sec. 4.1.

5.4.1 Three-quantum well diagonal structure

As shown in Fig. 5.10, one period of our three-well structure (sample S1443) consists of three GaAs quantum wells of decreasing width separated by $Al_{0.15}Ga_{0.75}As$ tunnel barriers. The radiative transition is diagonal in real space and occurs via a 3.0 nm wide AlGaAs injection barrier between state n=1' belonging to the third, narrower, GaAs quantum well of one period (width=13.5 nm) and state n=3 belonging to the first, broader, GaAs well of the following period (width=18.5 nm). In the bias voltage range studied, the ground state contains the majority of the electron population in this photon-assisted tunneling transition (see Sec. 2.6). A measurement of the current flowing in the structure allows then to derive the lifetime of the upper state ($n = 1'$) of the transition. Compared to vertical transitions presented in the previous section, the diagonal transition has a smaller oscillator strength and a broader linewidth due to the interface roughness, but it has the potential of a better lifetime ratio for population inversion.

The electronic sheet carrier density per period n_s induced by the doping was measured by capacitive measurements (see Sec. 2.5.2). We found for our sample (numbered as S1443) a value of $N_d = 2.95 \cdot 10^{15}$ cm^{-3} leading to an electronic sheet carrier density of $n_s = 1.67 \cdot 10^{10}$ cm^{-2}. This is about twice as large as the expected value $n_s = 0.87 \cdot 10^{10}$ cm^{-2} from the design.

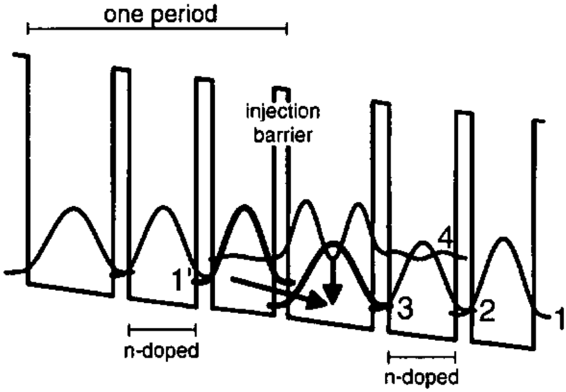

Figure 5.10: Self-consistent computation of the energy band diagram of two periods of the structure under an average applied electric field of 5.3 kV/cm. Shown are the moduli squared of the relevant wave functions. The diagonal arrow corresponds to the radiative transition 1'-3 and the vertical one to the vertical transition 4-3 identified in the luminescence spectra (see text). The layer sequence of one period of the structure left to right and starting with the injection barrier is **3.0**/18.5/**3.5**/14.5/**3.5**/13.5 (thicknesses in nanometers).

Optical measurements

For optical characterization, bursts of 1.7 μs long current pulses at 2.1 μs intervals were injected into the device, providing an overall duty-cycle of 40% at 413 Hz, in order to match the frequency response of the bolometer detector while minimizing heating effects.

A few representative spectra taken using the FTIR of Fig.3.4 at various increasing injected currents at $T = 5$ K are displayed in Fig. 5.11. They show that the luminescence spectrum consists of mainly three peaks. The first peak centered at a wavelength of about $\lambda = 87$ μm is identified as the desired n=1' to n=3 diagonal transition as its measured photon energy of $\sim$ 14.3 meV corresponds to the calculated values of about 11 to 17 meV depending on the applied voltage. The second peak is identified as the vertical transition between the n=4 and n=3 state in the 18.5 nm well; its measured photon energy of 28.7 meV corresponds well to the calculated value of 30.3 meV. The oscillator strength (see Appendix B) of the diagonal and vertical transitions are calculated as 1.21 and 13.7 respectively for a voltage of 1.46 V (corresponding to the spectrum taken at 100 mA). The origin of the peak at $h\nu \sim$ 37 meV, is attributed to a grating artifact.

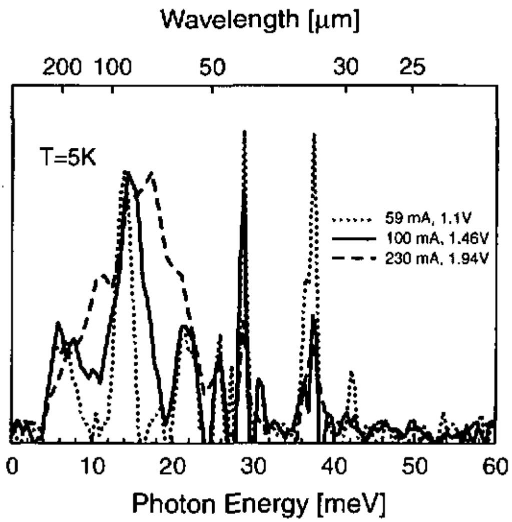

Figure 5.11: Luminescence spectra of the emitted radiation for three different injected currents at $T = 5$ K.

The ratio of the population of states $n = 4$ and $n = 1'$ allows to determine the electron temperature, because

$$\frac{n_4}{n_{1'}} = e^{\frac{-E_{41'}}{kT}} \tag{5.4.2}$$

where $E_{41'} = E_4 - E_{1'}$. The ratio of the population is also proportional to the ratio of the peak integral due to the $n = 4$ to $n = 3$ vertical transition and $n = 1'$ to $n = 3$ diagonal transition:

$$\frac{n_4}{n_{1'}} \cong \frac{I_{4-3}}{I_{1'-3}} \cdot \frac{f_{1'3}}{f_{43}} \cdot \frac{E^2_{1'3}}{E^2_{43}} \tag{5.4.3}$$

where I_{i-j} is the peak integral of the transition $i - j$, f_{ij} is the oscillator strength, and E_{ij} the transition energy, between states i and j. Taking into account the spectrum performed at 100 mA, we obtain an electron temperature of approximatively 30 K. The position of the 1'-3 transition as a function of applied bias is displayed in Fig. 5.12 along with the calculated values. The magnitude of the Stark tuning is significantly lower than the calculated values.

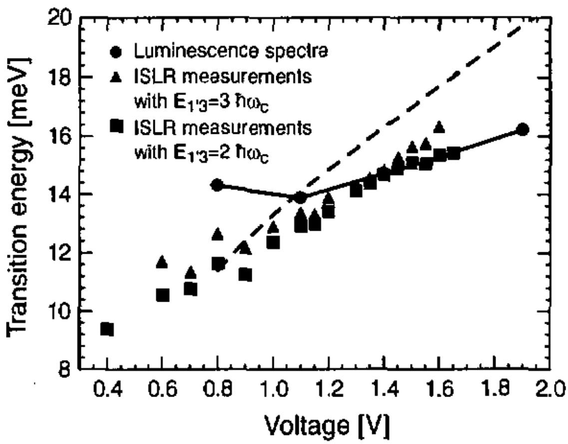

Figure 5.12: Luminescence peaks energy vs. voltage which corresponds to the observed Stark-shift and transition energy obtained by the intersubband Landau resonances measurements (see further in the text) with $E_{1'3} = \delta n \cdot \hbar\omega_c$ for $\delta n = 2$ (squares) and 3 (triangles). The dashed curve represents the calculated Stark-shift.

Lifetime with B=0

Figure 5.13 displays transport measurements such as voltage vs. current (V-I) and light intensity vs. current (L-I) curves which were performed on the same device at $T = 5$ K. In the V-I curve, one observes a region where negative differential resistance (NDR) occurs. This region was avoided in the electroluminescence spectra, because NDR is an indication for electrical instability of the device. As mentioned, one can, from these V-I curves, easily deduce the ground state lifetime τ_{nr} as a function of the voltage using the relation $\tau_{nr} = \frac{n_s q}{j}$, where n_s is the sheet density, q is the electronic charge and j the current density. With the value for the sheet density measured by capacitive measurements, one obtains a lifetime which decreases between τ_{nr}=100 ps at 0.8 V and τ_{nr}=20 ps at 2 V, as shown in the inset of Fig. 5.13.

In such structures based on photon-assisted tunneling, a necessary condition for electrical stability is that the overall scattering rate of the state $n = 3$ should increase with increasing electric field. But, due to the Stark effect, the transition energy $E_{1'3}$ increases with the applied electric field and thus the electron-electron w_{ee} and elastic $w_{elastic}$ scattering tend to decrease with increasing momentum exchange Δk, i.e. with increasing subband separation ($w_{ee}, w_{elastic} \sim \frac{1}{E_{1'3}}$ and $\Delta k \sim \sqrt{E_{1'3}}$). To compensate the latter effect, the tunneling matrix element between the states n=1' and n=3 should increase. In contrast to the work of Ref. 8, this tunneling matrix element is basically constant with applied electric field and therefore the structure is not electrically stable in the range of voltage 0.3 - 0.8 V. As we will see, the NDR can disappear with the application of a magnetic field on the structure.

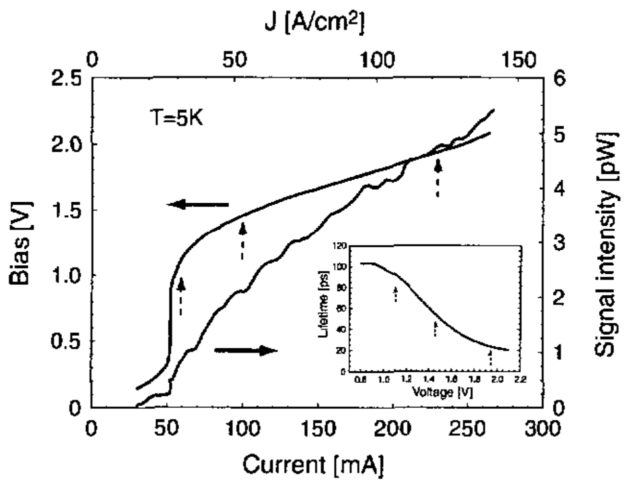

Figure 5.13: Luminescence intensity and bias vs. injected current at T=5K. Inset: lifetime of the upper state of the transition vs. voltage. The dashed vertical arrows indicate the position of the luminescence spectra of Fig. 5.11.

From a $n = 1'$ to $n = 3$ optical matrix element of about 1.8 nm (for an injected current of 100 mA), we derive a radiative lifetime of 63 μs and a radiative efficiency $\eta_{rad} = \tau_{nr}/\tau_{rad} \sim 8.7 \cdot$

10^{-7}. The optical power P_{opt} is related to the injected current I by $P_{opt} = \eta_{coll}\eta_{rad}N_{per}\frac{I}{q_0}h\nu$, where η_{coll} is the collection efficiency, N_{per} the number of periods and $h\nu$ the photon energy. If we take a collection efficiency of $\sim 1.3 \cdot 10^{-4}$ like in our previous paper (a value confirmed by new measurements on structures with vertical transition in GaAs and InGaAs wells) we calculate an expected optical power of 9.6 pW. This is between 4 and 5 times larger than the optical power obtained in luminescence measurements.

This discrepancy could have several reasons. Because of the small energy difference with the $n = 1'$ state, the population of the $n = 2'$ ($E_{1'2'} \sim 3.7$ meV) and $n = 3'$ ($E_{1'3'} \sim 7.1$ meV) could be increased if the electron temperature is high (calculated to be around 30 K). So the lifetime of the $n = 1'$ state should decrease. Moreover, the grating efficiency which involves in the collection efficiency could strongly depend of the processing. The matrix element of the transition could also be smaller than the calculated one.

Magneto-transport measurements

We measured V-I and I-B curves in a magnetic field perpendicular to the layers. V-I curves are plotted at 2K for zero, 7 and 12 Tesla in Fig. 5.14.

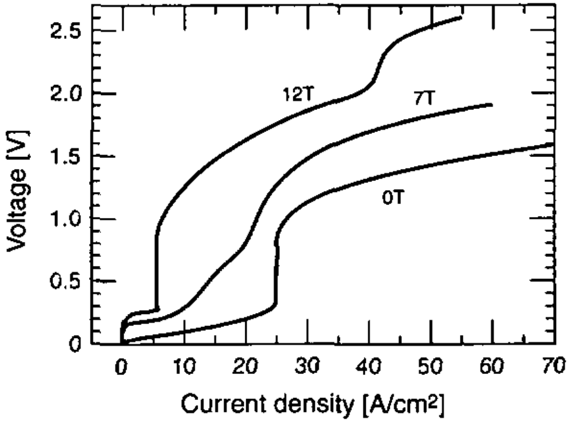

Figure 5.14: Voltage vs. injected current curves at zero, 7 and 12 Tesla at T = 2K. A NDR region occurs at zero and 12 Tesla, but not at 7 Tesla.

They show clearly that, at a fixed voltage, the current decreases strongly with increasing magnetic field. This overall decrease is in good agreement with the picture in which the intersubband transitions occur between dispersionless Landau levels instead of subbands, efficiently quenching the non-radiative transitions. In addition, the current range where NDR occurs shifts in current density and even disappears in the range of 2 - 4 and 5.5 - 10 Tesla. Fig. 5.16 shows in gray areas the regions where NDR occurs for sample S1443 as a function of the magnetic field and voltage. The magnetic field seems to suppress the NDR in this particular range and then to stabilize the structure.

In order to study the behavior of the current (and lifetime) in the structure as a function of the magnetic field, I-B curves were performed by setting the external voltage to a fixed value while ramping B between zero and maximum. It is now possible to plot the lifetime as a function of the magnetic field as shown in Fig. 5.15. As already mentioned, the lifetime is about 40-100 ps at zero field depending of the voltage.

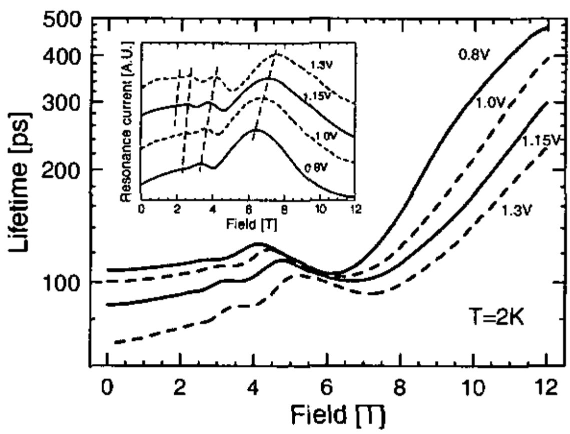

Figure 5.15: Lifetime of the upper state of the transition vs. applied magnetic field for different voltages at T = 2K. Inset: I-B curves with subtracted background current (exponential fit used to better identify the resonance maxima) for the same voltages. The curves are vertically displaced for clarity. The dashed lines show the resonance maxima.

Depending of the applied voltage, one observes a substantial lifetime increase with the magnetic field up to about 400 ps, which is a factor of 4 compared to the value without magnetic field. This increase became important only above 6T, where $\hbar\omega_c \sim 10.5$ meV which is comparable to the transition energy of $\sim$ 14 meV. It corresponds to the strong decrease of the current as a function of the magnetic field observed in the V-I curves.

Intersubband Landau resonances

The I-B curves show also maxima which we attribute to the intersubband Landau resonances explained in the beginning of this chapter, whose condition is given by Eqn. 5.1.1. These resonances are clearly resolved in the I-B curves (see Fig. 5.15). For a better identification of the resonance maxima, we fitted these raw data with an exponential fit, which was subsequently subtracted. The inset of Fig. 5.15 displays such curves with subtracted background current showing the resonances in I-B characteristics for four bias voltages V_{bias} = 0.8, 1.0, 1.15 and 1.3 V.

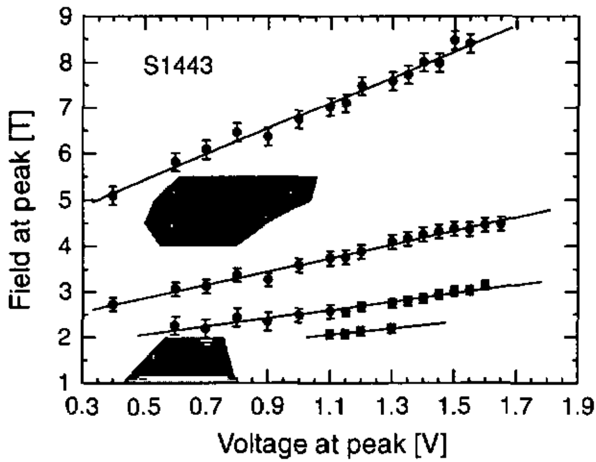

Figure 5.16: Experimental (B_p,V_p) points at Stark-cyclotron resonance with the fits resumed in Table 5.1 for sample S1443. The gray areas correspond to the regions where NDR occur.

To confirm the intersubband Landau resonances with our experimental resonances, we extracted the positions of magnetic field peaks (B_p) for several different external voltages (V_p) from I-B curves. In Fig. 5.16, one can see the (B_p, V_p) points plotted for the sample measured. According to the above equation, a plot of the magnetic field values for which a intersubband Landau resonance occurred as a function of applied voltage should align on straight lines.

	S1443		S1351	
δn	a [T/V]	a(1)/a(δn)	a [T/V]	a(1)/a(δn)
1	2.8± 0.3	[1]	3.2± 0.4	[1]
2	1.5± 0.2	1.9± 0.2	1.6± 0.3	2.07± 0.3
3	0.9± 0.2	3.1± 0.3	1.1± 0.2	3.0± 0.3
4	0.7± 0.3	4.0± 0.5		

Table 5.1: Results of linear fit for the data of Fig. 5.16 and Fig. 5.17. The intersubband Landau resonances are identified by computing the ratios of a(1)/a(δn).

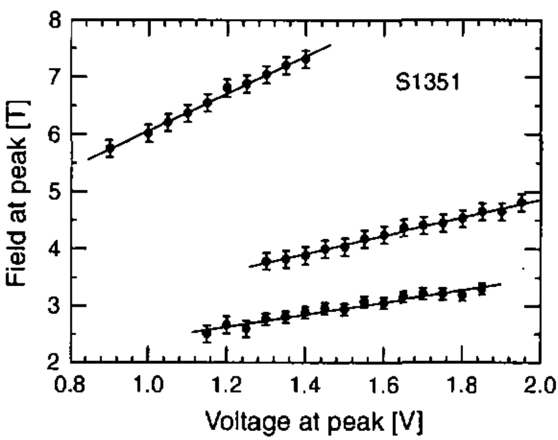

Figure 5.17: Experimental (B_p,V_p) points at Stark-cyclotron resonance with the fits resumed in Table 5.1 for sample S1351.

Experimental points clearly align along lines for the interval between 0.6 and about 1.6 V. The slopes of these lines are inversely proportional to the Landau-level index change δn, since $B_p \alpha \frac{V_p}{\delta n}$. Table 5.1 summarizes the values of the fitted slopes. Looking at the ratios of the slopes to the first one (at higher field), the intersubband Landau resonance conditions for transitions with $\delta n = 1,2,3$ and 4 are perfectly identified. In contrast to earlier papers of Beltram et al. [140, 141], we observed more easily the transitions with Landau-level index change $\delta n = 1$, but experienced more difficulty in measuring those with $\delta n=4$.

As Fig. 5.17 and the two last columns of the Table 5.1 show, we obtained similar results on an other, heavily doped, sample (S1351: $n_s = 7.06 \cdot 10^{10}$ cm^{-2} measured by capacitive measurements), except for $\delta n=4$.

Comparison spectra-transport measurements

We can derive the transition energy with the intersubband Landau resonances using the fact that $E_{13} = \delta n \cdot \hbar\omega_c$. Figure 5.12 shows the transition energies as a function of the voltage deduced form the spectra and from the magneto-transport measurements. The results correspond to the intersubband Landau resonances with $\delta n = 2$ and 3, which, in turn, are equivalent to the resonances occurring at a relatively small magnetic field. These magneto-transport measurements show good agreement with the calculated Stark-shift (dashed curve in Fig. 5.12) given the uncertainty in the calculation, and allow to confirm the diagonal-type of the transition. On the other hand, this figure shows that the Stark-shift from the electronic spectra is smaller than expected from calculations and shown by the location of the resonances in transport measurements. This difference can be explained by the fact that the spectra are very broad; this makes it difficult to determine precisely the transition energy of the relevant transition.

5.4.2 Five-quantum well diagonal structure

We designed a new far-infrared structure based on the same photon-assisted tunneling transition, but based on the conclusion of the discussion on the model described in Sec. 2.6 for a mid-IR quantum cascade laser. We observed that in such a structure the population of the ground state of one period decreases at higher temperature; mainly by populating the higher states, and in particular the excited state of the next period (state $n = 3$ in Fig. 5.19). So it seems to be important to push this state as high as possible. We chose also to design this structure with a five-well period instead of a three-well period as for the previous one in order to improve the stability of the structure.

Indeed, a necessary condition for the stability of the structure is that the overall scattering rate should increase with increasing electric field. This scattering rate is roughly proportional to $\frac{1}{\Delta k^2}$ times the overlap between the wavefunctions of the two states involved in the transition. In this photon-assisted tunneling transition, the transition energy increases with increasing electric field (Stark-shift), which makes $\frac{1}{\Delta k^2}$ decreasing. Therefore the design overcomes this effect in such a way that the overlap increases enough to compensate the decrease of $\frac{1}{\Delta k^2}$. As shown in Fig. 5.18 (right), the V-I curve of this new design (structure A2429) shows that the structure is stabilized. Indeed, we do not see any NDR, as in the previous structure (S1443). The V-I curves of both samples calculated numerically is also displayed on the left of Fig. 5.18. The scattering rate of the x-axis is proportional to the current.

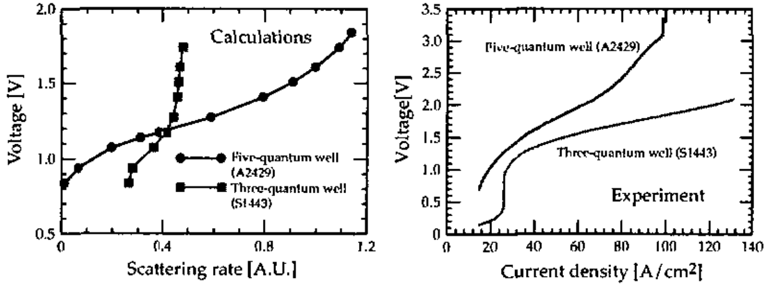

Figure 5.18: Comparison of V-I curves between five- and three-quantum well based structures, from the calculations (left) as well as from the experiment (right).

Structure

As shown in Fig. 5.19, each period of our five-well structure[2] comprises five GaAs quantum wells of decreasing width separated by $Al_{0.15}Ga_{0.85}As$ tunnel barriers. Under suitable applied bias, photon-assisted tunneling emission occurs via a 3.1 nm wide AlGaAs injection barrier between the ground state of the fifth, narrower, GaAs quantum well of one period (width = 9.4 nm) and the excited state of the first, broader, GaAs quantum well of the following period (width = 13.8 nm). The 15 μm metal grating was alloyed to avoid voltage losses in the contacts, which were observed on non-alloyed samples grown in Cambridge [145].

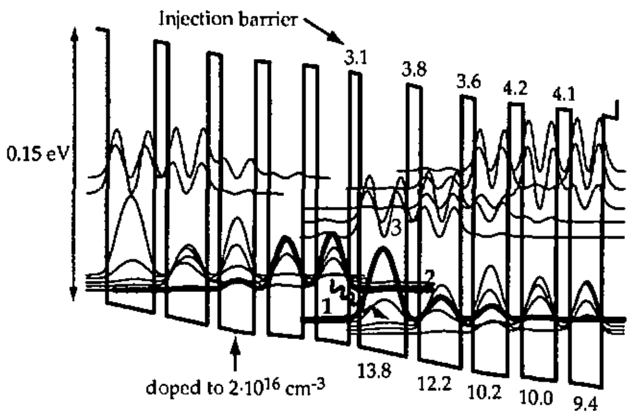

Figure 5.19: Self-consistent computation of the energy band diagram of two periods of the structure in $GaAs/Al_{0.15}Ga_{0.85}As$ material under an average applied electric field of 3.4 kV/cm. Shown are the moduli squared of the relevant wave functions. The wavy line indicates the transition responsible for electroluminescence emission between state 2 and 1. The thickness of the different layers is also indicated in nanometers.

Electroluminescence spectra

We performed electroluminescence measurements in the vacuum FTIR, as shown in Fig. 5.20. The light intensity increases and the peaks shift towards higher energies with increasing ap-

[2]This structure was also grown in Cambridge (UK) by the Cavendish Laboratory's group.

plied bias. This is due to the Stark-shift: as the electric field increases, the energy difference between states 2 and 1 increases proportionally to the field. The raw spectra have a broad shoulder at low energies due to a setup-inherent background blackbody. This shoulder was subtracted by a constant exponential fit and the resulting spectra are displayed in Fig. 5.20. There is still a shoulder at high voltage/current bias due to electron heating. An absorption at 16.4 meV is observed for several spectra. This absorption cannot be attributed to the atmosphere, because of the measurements were performed in vacuum. In fact this absorption is due to a quartz filter placed just in front of the Si bolometer [145]. The linewidth of about 3.5 meV of the emission peak is relatively narrow for a diagonal transition, but larger than the one for vertical transition which is about 1 meV, consistent with interface roughness scattering. Compared to the previous three-quantum well design, we do not observe additional peaks which proves that the new concept of the design is correct. In particular, it seems that the excited $n = 3$ state is not populated by hot electrons.

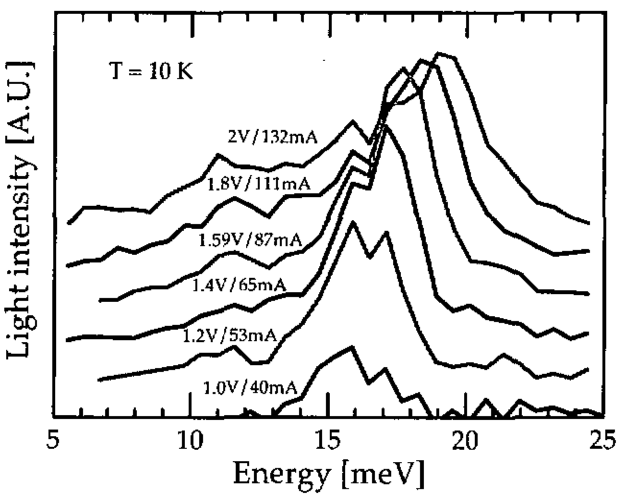

Figure 5.20: Electroluminescence spectra of sample A2429 based on a five-quantum well diagonal transition (with alloyed contacts) performed in the vacuum FTIR at different applied voltages. The Stark shift is clearly observable.

Again, to confirm that the transition is diagonal, we performed current versus magnetic field (I-B) curves. These measurements were performed on samples with non-alloyed contacts, but nevertheless seem to give consistent results. These curves, displayed in Fig. 5.21, show a strong decrease of the current in an oscillatory manner, as for the previous samples. The dashed lines mark the intersubband Landau resonances: they clearly indicate the signature of a diagonal transition. For the photon-assisted tunneling transition, we know that the non-radiative lifetime τ is inversely proportional to the current density j: $\tau = n_s e/j$, where n_s is the electronic sheet density. With a value of $n_s = 2.98 \cdot 10^{10}$ cm^{-2} measured by a capacitive measurement (see Sec. 2.5.2), one observes a lifetime increase with magnetic field up to about 350 ps, depending on the voltage, which is a factor of 2 compared to the zero field value.

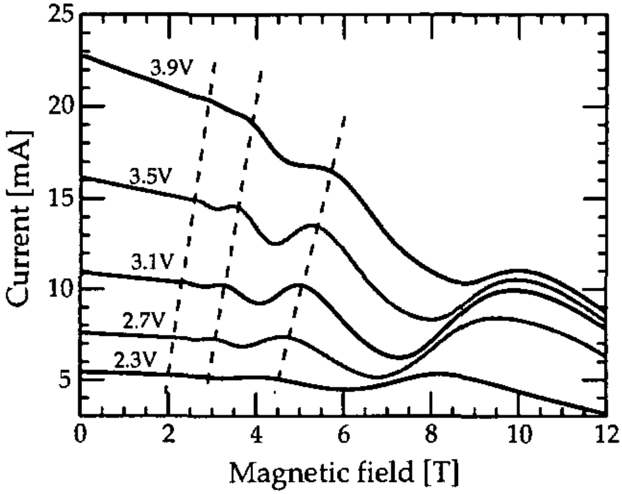

Figure 5.21: Current as a function of the magnetic field of sample A2429 based on a five-quantum well diagonal transition (non-alloyed contacts) for five different voltages. The dashed lines indicate the positions of the intersubband Landau resonances.

The oscillations are due to the intersubband Landau resonances with the condition given by Equ. 5.1.1. The resonance positions allow us to determine the transition energy by identifying the current maxima with different Landau level index-changes. In Fig. 5.22 is shown the comparison between the transition energy vs. voltage corresponding to the spectra and that extracted from the Landau intersubband resonances as well as the transition energy from calculations.

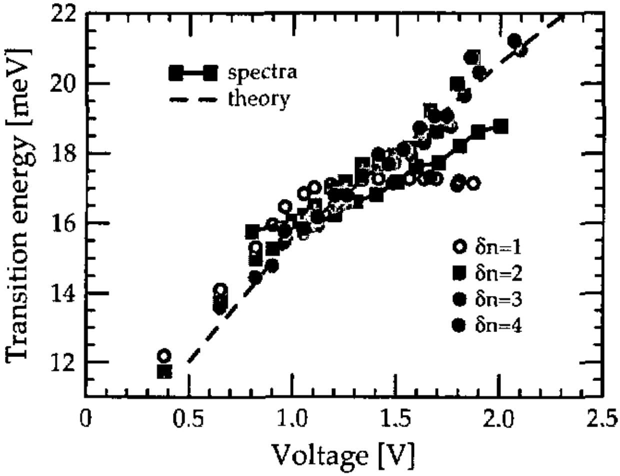

Figure 5.22: Transition energies deduced from magneto-transport measurements, FTIR spectra and calculations.

The Landau intersubband resonances, except for $\delta n = 1$ have given a transition energy in good agreement with the calculations, while the Stark shift resulting from the spectra is slightly smaller than expected, as in the previous structures. In order to match the calculations, the experimental values deduced from the magneto-transport measurements have been shifted by 1 or 2 V due to the contact problems observed with the non-alloyed samples [145]. Due to the observed blackbody emission, the peaks of the intersubband diagonal transition are slightly shifted at lower energies. This is probably the reason why we observed a smaller Stark-shift in the spectra than the one deduced from the magneto-transport measurements, which give the real positions of the resonances even in the presence of background effects.

Chapter 6

Conclusions

The application of a strong magnetic field, applied either perpendicular or parallel to the layers of a quantum cascade structures designed for the emission of light in the mid- as well as in the far-infrared, allows to obtain some new insight into the basic physics behind those emitters. By simulating a quantum box structure, in particular for devices emitting photons of less than 30 meV (in the far-infrared), we have experimentally investigated several theoretical proposals on 0D devices, by using the competition between magnetic and confinement potentials.

In the mid-infrared, the perpendicular magnetic field used during the experiments is not high enough to observe resonances between Landau level of small index and involving an optical phonon energy. To obtain the effect of the quantum box laser in the full quantum limit (cyclotron energy exceeding subband energy separation) here one needs a magnetic field of about 40 T for the InGaAs material system. Recently, a decrease of the threshold current by a factor of two [146] and oscillations in the tunneling current, explained as intersubband magnetophonon resonances due to electron relaxation by emission of optical and acoustic phonons [147], have been demonstrated in GaAs quantun cascade structures using such high fields.

In our far-infrared structures, we observed an increase of the intersubband non-radiative lifetime of the upper state by applying a strong perpendicular magnetic field. This effect is accompanied by the decrease of the current (at a fixed voltage) with increasing magnetic field, as the transition occurs between Landau levels instead of subbands.

For vertical-transition based structures, the enhancement of the light intensity observed in magnetic field confirms this conclusion and indicates an increase of the radiative efficiency, if we assume that the radiative lifetime stays constant. We did not observe gain by measuring such vertical structures, embedded in a waveguide, at different injection currents in the FTIR (i.e. without applying a magnetic field). To see if there is gain in such structures – by measuring it in magnetic field, we did not directly observe lasing action, we need comparisons between measurements performed with grating- and waveguide- structures in magnetic field.

For diagonal transition-based structures, this increase of the non-radiative lifetime, up to a factor of four, is directly deduced from the magneto-transport measurements. Furthermore, as the photon-assisted tunneling transition is designed to favor population inversion, these structures are promising for a far-infrared quantum cascade laser. Electroluminescence spectra measurements of such structures in perpendicular magnetic field should allow a measure of a possible gain. The diagonal-based structures are more influenced by the interface roughness which plays a important role. In the presence of a parallel magnetic field, the luminescence of a photon-assisted tunneling transition-based structure decreases in the mid-infrared. This effect is precisely attributed to disorder. It is then also interesting to measure mid-infared QC structures based on vertical transitions in parallel magnetic field in order to investigate the exact role of interface roughness, and, as already mentioned, to explore the graded-interface concept.

In this work, we have shown that magneto-transport measurements are a powerful technique to confirm the electronic spectrum and to gain insight into the physics of intersubband transitions of far-infrared structures consisting of various active regions, i.e. based on vertical- and diagonal-transitions or even in transitions in superlattices.

As we know now that the quantum cascade technology, in particular the chirped superlattice design, can be used for laser action also in the far-infrared or terahertz range, and not only in the mid-infrared, the new challenge will be to find other better working designs.

Acknowledgements

First of all I would like to thank my thesis director, Prof. Jérôme Faist, for having given me the opportunity of doing this work, his continuous support and his all-day-enthusiasm, in particular in the beginning when the labs were practically empty, except the two optical tables. Jérôme is also a "100 ideas per day - man". That was really motivating during the years I spent in his research group.

I would like to thank Dr. Ulf Gennser (LPN-CNRS, Marcoussis, France), Dr. Romuald Houdré (EPF Lausanne) and Prof. Piero Martinoli (University of Neuchâtel) for critically reading the manuscript and for acting as co-examiners in the jury. Piero is also acknowledged for hosting me during my diploma work in his superconductivity group.

I want to thank warmly thank the "Docteur Professeur" Daniel "Tetris" Hofstetter for his help, his swiss-german language in the lab (!) and in particular for his careful reading of and remarks on this thesis. Not forgetting that Daniel is still first in the famous hall of fame of the linux computer of the third floor... The second post-doc of the group, Mattias "Tisi" Beck, has to be acknowledged both as grower and as colleague. Such a work can not be possible without excellent QC layers. I thank him also for his constant encouragement and enthusiasm.

My PhD colleague, Michel "Ça lase?" Rochat, who spent more than four years between labs, offices and conferences with me in good mood, deserves a full load of acknowledgments for the hours spent together and the numerous discussions about QC physics as well as about "les Arteplages"!

I thank the *new* PhD colleagues, "le PSIteux" Laurent Diehl and Lassaad Ajili for all their work accomplished during their diploma stage, Thierry R. "Marcello" Aellen, Harry

"Haraldino" Willenberg and "Il doctore" Giacomo "Jacques" Scalari. The members of Alpes Lasers, namely Antoine, Hege and Yargo, who shared the labs, are also thanked for their good collaboration.

Members of the different workshops of the IPH, namely the electronics and mechanics department, have all my gratitude for their technical support. Indeed we started from zero and they helped us in many different ways to build up the lab and made quickly pieces with often a delay "pour hier"!

Some of these people and other colleagues have to be acknowledged for the time we spent together outside the labs to drink a beer, "sorties", ski week-ends, conferences,... Thank you Mattias, Laurent, Thierry, Harry, Giacomo, Daniel, Michel, Marcella,...

Thanks also to my family for her generous support during my studies.

Last but not least, I would like to thank all friends with whom I spent a lot of time in holidays, partys, fun-days,... Thanks a lot to Isa, Sonia, Christelle, Cath, Fab, Greg, Vilouts, Christophe, Céline, Mouli, ...

This work was supported by the Swiss National Science Foundation.

Bibliography

[1] J. Faist, F. Capasso, D.L. Sivco, C. Sirtori, A.L. Hutchinson, and A.Y. Cho, "Quantum cascade laser", Science **264**, 553–556 (1994).

[2] J. Faist, F. Capasso, D.L. Sivco, A.L. Hutchinson, S. Chu, and A.Y. Cho, "Short wavelength ($\lambda \sim 3.4$ μm) quantum cascade laser based on strained compensated InGaAs/AlInAs", Appl. Phys. Lett. **72**, 680–682 (1998).

[3] M. Rochat, D. Hofstetter, M. Beck, and J. Faist, "Long wavelength ($\lambda \sim 16\mu$m), room-temperature, single frequency quantum-cascade lasers based on a bound-to-continuum transition", Appl. Phys. Lett. **79**, 4271–4273 (2001).

[4] R. Colombelli, F. Capasso, C. Gmachl, A.L. Hutchinson, D.L. Sivco, A. Tredicucci, M.C. Wanke, A.Michael Sergent, and A.Y. Cho, "Far-infrared surface-plasmon quantum-cascade lasers at 21.5 μm and 24 μm wavelengths", Appl. Phys. Lett. **78**, 2620–2622 (2001).

[5] F. Capasso, "Bandgap and interface engineering for advanced electronic an photonic devices", MRS Bulletin **16**, 23–29 (1991).

[6] A. Cho, *Molecular Beam Epitaxy*, AIP Press, Woodbury, NW, 1994.

[7] J. Faist, F. Capasso, C. Sirtori, D.L. Sivco, J.N. Baillargeon, A.L. Hutchinson, S. Chu, and A.Y. Cho, "High power mid-infrared ($\lambda \sim 5$ μm) quantum cascade lasers operating above room temperature", Appl. Phys. Lett. **68**, 3680–3682 (1996).

[8] N. Ulbrich, G. Scarpa, A. Sigl, J. Rosskopf, G. Böhm, G. Abstreiter, and M.C. Amann, "High-temperature ($T > 470$ K) pulsed operation of 5.5 μm quantum cascade lasers with high-reflection coating", IEE Elect. Lett. **37**, 1341–1342 (2001).

[9] C. Sirtori, P. Kruck, S. Barbieri, P. Collot, J. Nagle, M. Beck, J. Faist, and U. Oesterle, "GaAs/Al_xGa_{1-x}As quantum cascade lasers", Appl. Phys. Lett. **73**, 3486–3488 (1998).

[10] H. Page, C. Becker, A. Robertson, G. Glastre, V. Ortiz, and C. Sirtori, "300K operation of a GaAs-based quantum-cascade laser at $\lambda \sim 9\mu$m", Appl. Phys. Lett. **75**, 3529–3531 (2001).

[11] M. Beck, D. Hofstetter, T. Aellen, J. Faist, U. Oesterle, M. Ilegems, E. Gini, and H. Melchior, "*Continuous-wave operation of a mid-infrared semiconductor laser at room-temperature*", Science **295**, 301–305 (2002).

[12] M. Rochat, J. Faist, M. Beck, U. Oesterle, and M. Ilegems, "Far-Infrared ($\lambda = 88\ \mu m$) electroluminescence in a quantum cascade structure", Appl. Phys. Lett. **73**, 3724–3726 (1998).

[13] R. Köhler, A. Tredicucci, F. Beltram, H.E. Beere, E.H. Linfield, A.Giles Davies, D.A. Ritchie, R.C. Iotti, and F. Rossi, "Terahertz semiconductor-heterostructure laser", Nature **417**, 156–159 (2002).

[14] M. Rochat, L. Ajili, H. Willenberg, J. Faist, H. Beere, G. Davies, E. Linfield, and D. Ritchie, "Low threshold terahertz quantum cascade lasers", unpublished, 2002.

[15] G. Dehlinger, L. Diehl, U. Gennser, H. Sigg, J. Faist, K. Ensslin, D. Grützmacher, and E. Müller, "Intersubband electroluminescence from silicon-based quantum cascade structures", Science **290**, 2277–2280 (2000).

[16] M. Tacke, "Lead salt lasers", in *Long wavelength infrared emitters based on quantum wells and superlattices*, edited by Manfred Helm, volume 6, chapter 9, pages 347–396, Gordon and breach Science, Amsterdam, 2000.

[17] H.K. Choi and G.W. Turner, "Antimonide-based mid-infrared lasers", in *Long wavelength infrared emitters based on quantum wells and superlattices*, edited by Manfred Helm, volume 6, chapter 7, pages 225–305, Gordon and breach Science, Amsterdam, 2000.

[18] R.Q. Yang, "Infrared laser based on intersubband transitions in quantum wells", Superlatt. Microstruct. **17**, 77–77 (1995).

[19] R.Q. Yang, C.H. Lin, P.C. Chang, S.J. Murry, D. Zhang, S.S. Pei, S.R. Kurtz, A.N. Chu, and F. Ren, "Mir-IR interband cascade electroluminescence in type-II quantum wells", IEE Elect. Lett. **32**, 1621–1622 (1996).

[20] C. Lin, R.Q. Yang, D. Zhang, S.J. Murry, S.S. Pei, A.A. Allerman, and S.R. Kurtz, "Type-II interband quantum cascade laser at 3.8 μm", IEE Elect. Lett. **33**, 598–599 (1997).

[21] J.D. Bruno, J.L. Bradshaw, R.Q. Yang, J.T. Pham, and D.E. Wortman, "Low-threshold interband cascade lasers with power efficiency exceeding 9 %", Appl. Phys. Lett. **76**, 3167–3169 (2000).

[22] J.L. Bradshaw, R.Q. Yang, J.D. Bruno, J.T. Pham, and D.E. Wortman, "High-efficiency interband cascade lasers with peak power exceeding 4 W/facet", Appl. Phys. Lett. **75**, 2362–2364 (1999).

[23] O. Gauthier-Lafaye, P. Boucaud, F.H. Julien, S. Sauvage, S. Cabaret, J.M. Lourtioz, and R. Planel, "Long-wavelength (≈ 15.5μm) unipolar semiconductor laser in GaAs quantum wells", Appl. Phys. Lett. **71**, 3619-3621 (1997).

[24] O.Gauthier-Lafaye, F.H. Julien, S. Cabaret, J.M. Lourtioz, G. Strasser, E. Gornik, M. Helm, and P. Bois, "High-power GaAs/AlGaAs quantum fountain unipolar laser emitting at 14.5 μm with 2.5% tunability", Appl. Phys. Lett. **74**, 1537–1539 (1999).

[25] A.A. Andronov, I.V. Zverev, V.A. Kozlov, Y.N. Nozdrin, S.A. Pavlov, and V.N. Shastin, "Stimulated emission in the long-wavelength IR region from hot holes in Ge in crossed electric and magnetic fields", JETP Lett. **40**, 804–807 (1984).

[26] K. Unterrainer, C. Kremser, E. Gornik, C.R. Pidgeon, Y.L. Ivanov, and E.E. Haller, "Tunable cyclotron-resonance laser in germanium", Phys. Rev. Lett. **64**, 2277–2280 (1990).

[27] B.A. Paldus, T.G. Spence, R.N. Zare, J. Oomens, F. Harren, D.H. Parker, C. Gmachl, F. Capasso, D.L. Sivco, J.N. Baillargeon, A.L. Hutchinson, and A.Y. Cho, "Photoacoustic spectroscopy using quantum-cascade lasers", Opt. Lett. **24**. 178–180 (1999).

[28] D. Hofstetter, M. Beck, J. Faist, M. Nägele, and M.W. Sigrist, "Photoacoustic spectroscopy with quantum cascade distributed-feedback lasers", Opt. Lett. **26**, 887–889 (2001).

[29] A. Müller, M. Beck, J. Faist, R. Schindler, H. Ehmoser, and B. Lendl, "Novel quantum cascade laser based measurements of chemicals in liquid and gases with 50 fold improved signal to noise ratio", in *Proceedings of Sensors Expo*, pages 253–254, Cleveland (USA), 1999.

[30] S.W. Sharpe, J.F. Kelly, J.S. Hartmann, C. Gmachl, F. Capasso, D.L. Sivco, J.N. Baillargeon, and A.Y. Cho, "High-resolution (Doppler-limited) spectroscopy using quantum-cascade distributed-feedback lasers", Opt. Lett. **23**, 1396–1398 (1998).

[31] K. Namjou, S. Cai, E.A. Whittaker, J. Faist, C. Gmachl, F. Capasso, D.L. Sivco, and A.Y. Cho, "Sensitive absorption spectroscopy with a room-temperature distributed-feedback quantum-cascade laser", Opt. Lett. **23**, 219–221 (1998).

[32] B.A. Paldus, C.C. Harb, T.G. Spence, R.N. Zare, C. Gmachl, F. Capasso, D.L. Sivco, J.N. Baillargeon, A.L. Hutchinson, and A.Y. Cho, "Cavity ringdown spectroscopy using mid-infrared quantum-cascade lasers", Opt. Lett. **25**, 666–668 (2000).

[33] N. Mustafa, L. Pesquera, C. Cheung, and K.A. Stone, "Terahertz bandwidth prediction for amplitude modulation response of unipolar intersubband semiconductor lasers", IEEE Photon. Technol. Lett. **11**, 527–529 (1999).

[34] J. Faist, F. Capasso, C. Sirtori, D.L. Sivco, and A.Y. Cho, "Quantum cascade lasers", in *Intersubband transitions in quantum wells: Physics and device applications II*, edited by H.C. Liu and F. Capasso, volume 66, chapter 1, pages 1–83, Academic Press, 2000.

[35] R. Martini, C. Gmachl, J. Falciglia, F.G. Curti, C.G. Bethea, F. Capasso, E.A. Whittaker, R. Paiella, A. Tredicucci, A.L. Hutchinson, D.L. Sivco, and A.Y. Cho, "High-speed modulation and free-space optical audio/video transmission using quantum cascade lasers", IEE Elect. Lett. **37**, 102–103 (2001).

[36] S. Blaser, D. Hofstetter, M. Beck, and J. Faist, "Free-space optical data link using Peltier-cooled quantum cascade laser", IEE Elect. Lett. **37**, 778–780 (2001).

[37] L. Esaki and R. Tsu, "Superlattice and negative differential conductivity in semiconductors", IBM J. Res. Develop. **14**, 61–65 (1970).

[38] A.A. Ignatov and Y.A. Romanov, "Nonlinear electromagnetic properties of semiconductors with a superlattice", Phys. Stat. Sol. B **73**, 327–333 (1976).

[39] G.H. Wannier, "Dynamics of band electrons in electric and magnetic fields", Rev. Mod. Phys. **34**, 645-655 (1962).

[40] R.F. Kazarinov and R.A. Suris, "Possibility of the amplification of electromagnetic waves in a semiconductor with a superlattice", Sov. Phys. Semicond. **5**, 707–709 (1971).

[41] R.F. Kazarinov and R.A. Suris, "Electric and electromagnetic properties of semiconductors with a superlattice", Sov. Phys. Semicond. **6**, 120–131 (1972).

[42] F. Capasso, K. Mohammed, and A.Y. Cho, "Resonant tunneling through double barriers, perpendicular quantum transport phenomena in superlattices, and their device applications", IEEE J. Quantum Electron. **22**, 1853–1869 (1986).

[43] A. Sibille, J.F. Palmier, H. Wang, and F. Mollot, "Observation of Esaki-Tsu negative differential velocity in GaAs/AlAs superlattices", Phys. Rev. Lett. **64**, 52–55 (1990).

[44] E. Gornik and D.C. Tsui, "Voltage-tunable far-infrared emission from Si inversion layers", Phys. Rev. Lett. **37**, 1425-1428 (1976).

[45] L.C. West and S.J. Eglash, "First observation of an extremely large-dipole infrared transition within the conduction band of a GaAs quantum well", Appl. Phys. Lett. **46**, 1156–1158 (1985).

[46] M. Helm, P. England, E. Colas, F. DeRosa, and S. Allen, "Intersubband emission from semiconductor superlattices excited by sequential resonant tunneling", Phys. Rev. Lett. **63**, 74–77 (1989).

[47] G. Scamarcio, F. Capasso, A.L. Hutchinson, D.L. Sivco, and A.Y. Cho, "Midinfrared emission from coupled Wannier-Stark ladders in semiconductor superlattices", Phys. Rev. B **57**, R6811–6814 (1998).

[48] S.I. Borenstain and J. Katz, "Evaluation of the feasibility of a far-infrared laser based on intersubband transitions in GaAs quantum wells", Appl. Phys. Lett. **55**, 654–656 (1989).

[49] A. Kastalsky, V.J. Goldman, and J.H. Abeles, "Possibility of infrared laser in a resonant tunneling structure", Appl. Phys. Lett. **59**, 2636–2638 (1991).

[50] Q. Hu and S. Feng, "Feasibility of far-infrared lasers using multiple semiconductor quantum wells", Appl. Phys. Lett. **59**, 2923–2925 (1991).

[51] P.fei Yuh and K.L. Wang, "Novel infrared band-aligned superlattice laser", Appl. Phys. Lett. **51**, 1404–1406 (1987).

[52] G.N. Henderson, L.C. West, T.K. Gaylord, C.W. Roberts, E.N. Glytsis, and M.T. Asom, "Optical transitions to above-barrier quasibound states in asymmetric semiconductor heterostructures", Appl. Phys. Lett. **62**, 1432–1434 (1993).

[53] C. Gmachl, F. Capasso, A. Tredicucci, D.L. Sivco, R. Köhler, A.L. Hutchinson, and A.Y. Cho, "Dependence of the device performance on the number of stages in quantum-cascade lasers", IEEE J. Select. Topics Quantum Electron. **5**, 808–816 (1999).

[54] C. Gmachl, F. Capasso, A. Tredicucci, D.L. Sivco, A.L. Hutchinson, S.George Chu, and A.Y. Cho, "Noncascaded intersubband injection lasers at $\lambda = 7.7$ μm", Appl. Phys. Lett. **73**, 3830–3832 (1998).

[55] J. Faist, F. Capasso, C. Sirtori, D.L. Sivco, A.L. Hutchinson, S. Chu, and A.Y. Cho, "Narrowing of the intersubband electroluminescent spectrum in coupled-quantum well heterostructures", Appl. Phys. Lett. **65**, 94–96 (1994).

[56] H. Mathieu, *Physique des Semiconducteurs et des Composants Électroniques*, Masson, Paris, 4e edition, 1998.

[57] R. Ferreira and G. Bastard, "Evaluation of some scattering times for electrons in unbiased and biased single-and multiple-quantum-well structures", Phys. Rev. B **40**, 1074–1086 (1989).

[58] P.J. Price, "Two-dimensional electron transport in semiconductor layers I: phonon scattering", Ann. Phys. (San Diego) **133**, 217–239 (1981).

[59] P.J. Price, "Two-dimensional electron transport in semiconductor layers II: screening", J. Vac. Sci. Technol. **19**, 599–603 (1981).

[60] Pallab Bhattacharya, editor, *Properties of lattice-matched and strained Indium Gallium Arsenide*, INSPEC, the Institution of Electrical Engineers, London, 1993.

[61] M. Helm, "The basic physics of intersubband transitions", in *Intersubband transitions in quantum wells: Physics and device applications I*, edited by H.C. Liu and F. Capasso, volume 62, chapter 1, pages 1–99, Academic Press, 2000.

[62] S.C. Lee, I. Galbraith, and C.R. Pidgeon, "Influence of electron temperature and carrier concentration on electron-LO-phonon intersubband scattering in wide $GaAs/Al_xGa_{1-x}As$ quantum wells", Phys. Rev. B **52**, 1874–1881 (1995).

[63] M. Rochat, M. Beck, J. Faist, U. Oesterle, and M. Ilegems, "Electrically pumped terahertz quantum well sources", Physica E **7**, 44-47 (2000).

[64] K.D. Maranowski, *Parabolically graded semiconductor quantum wells for emisison of far-infrared radiation*, PhD thesis, University of California, Santa Barbara, 2000.

[65] J.H. Smet, C.G. Fonstad, and Q. Hu, "Intrawell and interwell intersubband transitions in multiple quantum wells for far-infrared sources", J. Appl. Phys. **79**, 9305-9320 (1996).

[66] M. Hartig, S. Haacke, P.E. Selbmann, B. Deveaud, R.A. Taylor, and L. Rota, "Efficient intersubband scattering via carrier-carrier interaction in quantum wells", Phys. Rev. Lett. **80**, 1940-1943 (1998).

[67] K. Donovan, P. Harrison, and R.W. Kelsall, "Comparison of the quantum efficiencies of interwell and intrawell radiative transitions in quantum cascade lasers", Appl. Phys. Lett. **75**, 1999-2001 (1999).

[68] J.B. Williams, M.S. Sherwin, K.D. Maranowski, and A.C. Gossard, "Dissipation of intersubband plasmons in wide quantum wells", Phys. Rev. Lett. **87**, 37401-1-37401-4 (2001).

[69] C.A. Ullrich and G. Vignale, "Theory of the linewidth of intersubband plasmons in quantum wells", Phys. Rev. Lett. **87**, 37402-1-37402-4 (2001).

[70] A. Yariv, *Quantum electronics*, John Wiley & Sons, New-York, 3^{rd} edition, 1989.

[71] J. Faist, F. Capasso, C. Sirtori, D.L. Sivco, A.L. Hutchinson, and A.Y. Cho, "Laser action by tuning the oscillator strength", Nature **387**, 777-782 (1997).

[72] J. Faist, F. Capasso, C. Sirtori, D.L. Sivco, A.L. Hutchinson, and A.Y. Cho, "Electric-field-tunable quantum cascade lasers by oscillator strength tuning", in *Long wavelength infrared emitters based on quantum wells and superlattices*, edited by Manfred Helm, volume 6, chapter 3, pages 65-87, Gordon and breach Science, Amsterdam, 2000.

[73] S. Blaser, L. Diehl, M. Beck, J. Faist, U. Oesterle, J. Xu, S. Barbieri, and F. Beltram, "Characterization and modeling of quantum cascade lasers based on photon-assisted tunneling transition", IEEE J. Quantum Electron. **37**, 448-455 (2001).

[74] A. Müller, M. Beck, J. Faist, and U. Oesterle, "Electrically tunable, room-temperature quantum-cascade lasers", Appl. Phys. Lett. **75**, 1509-1511 (1999).

[75] C. Sirtori, F. Capasso, J. Faist, A.L. Hutchinson, D.L. Sivco, and A.Y. Cho, "Resonant tunneling in quantum cascade lasers", IEEE J. Quantum Electron. **34**, 1722-1729 (1998).

[76] G. Bastard, *Wave mechanics applied to semiconductor heterostructures*, Les éditions de physique, Les Ulis, France, 1988.

[77] A.P. Heberle, W.W. Rühle, and K. Ploog, "Quantum beats of electron Larmor precession in GaAs wells", Phys. Rev. Lett. **72**, 3887–3890 (1994).

[78] A.A. Kiselev, E.L. Ivchenko, and U. Rössler, "Electron g factor in one- and zero-dimensional semiconductor nanostructures", Phys. Rev. B **58**, 16353–16359 (1998).

[79] C. Weisbuch and C. Hermann, "Optical detection of conduction-electron spin resonance in GaAs, $Ga_{1-x}In_xAs$, and $Ga_{1-x}Al_xAs$", Phys. Rev. B **15**, 816–822 (1977).

[80] M. Oestreich, S. Hallstein, A.P. Heberle, K. Eberl, E. Bauser, and W.W. Rühle, "Temperature and density dependence of the electron Landé g factor in semiconductors", Phys. Rev. B **53**, 7911–7916 (1996).

[81] A. Malinowski and R.T. Harley, "Anisotropy of the electron g factor in lattice-matched and strained-layer III-V quantum wells", Phys. Rev. B **62**, 2051–2056 (2000).

[82] B. Kowalski, P. Omling, B.K. Meyer, D.M. Hofmann, C. Wetzel, V. Härle, F. Scholz, and P. Sobkowicz, "Conduction-band spin splitting of type-I $Ga_xIn_{1-x}As/InP$ quantum wells", Phys. Rev. B **49**, 14786–14789 (1994).

[83] B. Kowalski, H. Linke, and P. Omling, "Spin-resonance determination of the electron effective g value of $In_{0.53}Ga_{0.47}As$", Phys. Rev. B **54**, 8551–8555 (1996).

[84] L. Landau and E. Lifchitz, *Mécanique quantique, théorie non relativiste*, Editions Mir, Moscou, 1967.

[85] T. Ando, "Subband structure of an accumulation layer under strong magnetic fields", J. Phys. Soc. Jpn **39**, 411–417 (1975).

[86] W. Beinvogl, A. Kamgar, and J.F. Koch, "Influence of a magnetic field on electron subbands in a surface space-charge layer", Phys. Rev. B **14**, 4274–4280 (1976).

[87] K.K. Choi, B.F. Levine, N. Jarosik, J. Walker, and R. Malik, "Anisotropic magnetotransport in weakly coupled GaAs-$Al_xGa_{1-x}As$ multiple quantum wells", Phys. Rev. B **38**, 12362–12368 (1988).

[88] W. Zawadzki, S. Klahn, and U. Merkt, "Inversion electrons on narrow-band-gap semiconductors in crossed electric and magnetic fields", Phys. Rev. B **33**, 6916–6928 (1986).

[89] W. Demmerle, J. Smoliner, G. Berthold, E. Gornik, G. Weimann, and W. Schlapp, "Tunneling spectroscopy in barrier-separated two-dimensional electron-gas systems", Phys. Rev. B **44**, 3090–3104 (1991).

[90] F. Stern and W.E. Howard, "Properties of semiconductor surface inversion layers in the electric quantum limit", Phys. Rev. **163**, 816–835 (1967).

[91] F. Stern, "Transverse Hall effect in the electric quantum limit", Phys. Rev. Lett. **21**, 1687–1690 (1968).

[92] E.H. Putley, "Far infra-red photoconductivity", phys. stat. sol. **6**, 571–614 (1964).

[93] E. Gornik, "Landau emission", in *Landau level spectroscopy*, edited by G. Landwehr and E. I. Rashba, chapter 16, pages 911–996, Elsevier Science Publishers, 1991.

[94] K.von Klitzing, G. Dorda, and M. Pepper, "New method for high-accuracy determination of the fine-structure constant based on quantized Hall resistance", Phys. Rev. Lett. **45**, 494–497 (1980).

[95] R.B. Laughlin, "Quantized Hall conductivity in two dimensions", Phys. Rev. B **23**, 5632–5633 (1981).

[96] D.C. Tsui and A.C. Gossard, "Resistance standard using quantization of the Hall resistance of GaAs-Al_xGa_{1-x}As heterostructures", Appl. Phys. Lett. **38**, 550–552 (1981).

[97] H.L. Stormer, Z. Schlesinger, A. Chang, D.C. Tsui, A.C. Gossard, and W. Wiegmann, "Energy structure and quantized Hall effect of two-dimensional holes", Phys. Rev. Lett. **51**, 126–129 (1983).

[98] B. Jensen, "Calculation of the refractive index of compound semiconductors below the band gap", in *Handbook of Optical Constants of Solids II*, edited by E. D. Palik, chapter 6, pages 125–149, Academic Press, Inc., San Diego, 1991.

[99] M. Beck, J. Faist, U. Oesterle, M. Ilegems, E. Gini, and H. Melchior, "Buried heterostructure quantum cascade lasers with a large optical cavity waveguide", IEEE Photon. Technol. Lett. **12**, 1450–1452 (2000).

[100] D. Hofstetter, M. Beck, T. Aellen, J. Faist, U. Oesterle, M. Ilegems, E. Gini, and H. Melchior, "Continuous wave operation of a 9.3 μm quantum cascade laser on a Peltier cooler", Appl. Phys. Lett. **78**, 1964–1966 (2001).

[101] C. Sirtori, C. Gmachl, F. Capasso, J. Faist, D.L. Sivco, A.L. Hutchinson, and A.Y. Cho, "Long-wavelength ($\lambda = 8$-11.5 μm) semiconductor lasers with waveguides based on surface plasmons", Opt. Lett. **23**, 1366–1368 (1998).

[102] M. Rochat, M. Beck, J. Faist, and U. Oesterle, "Measurement of far-infrared waveguide loss using a multisection single-pass technique", Appl. Phys. Lett. **78**, 1967–1969 (2001).

[103] M. Helm, E. Colas, P. England, F. DeRosa, and S.J. Allen, "Observation of grating-induced intersubband emission from GaAs/AlGaAs superlattices", Appl. Phys. Lett. **53**, 1714–1716 (1988).

[104] W.J. Li and B.D. McCombe, "Coupling efficiency of metallic gratings for excitation of intersubband transitions in quantum-well structures", J. Appl. Phys. **71**, 1038–1040 (1992).

[105] J. Faist, C. Sirtori, F. Capasso, D.L. Sivco, J.N. Baillargeon, A.L. Hutchinson, and A.Y. Cho, "High-power long-wavelength ($\lambda = 11.5$ μm) quantum cascade lasers operating above room temperature", IEEE Photon. Technol. Lett. **10**, 1100–1102 (1998).

[106] C. Sirtori, J. Faist, F. Capasso, and A.Y. Cho, 2000, private communication.

[107] R.M. Williams, J.F. Kelly, J.S. Hartman, S.W. Sharpe, M.S. Taubman, J.L. Hall, F. Capasso, C. Gmachl, D.L. Sivco, J.N. Baillargeon, and A.Y. Cho, "Kilohertz linewidth from frequency-stabilized mid-infrared quantum cascade lasers", Opt. Lett. **24**, 1844–1846 (1999).

[108] B.W. Hakki and T.L. Paoli, "Gain spectra in GaAs double-heterostructure injection lasers", J. Appl. Phys. **46**, 1299–1306 (1975).

[109] D. Hofstetter and J. Faist, "Measurement of semiconductor laser gain and dispersion curves utilizing Fourier transforms of the emission spectra", IEEE Photon. Technol. Lett. **11**, 1372–1374 (1999).

[110] C. Sirtori, J. Faist, F. Capasso, D.L. Sivco, A.L. Hutchinson, and A.Y. Cho, "Long wavelength infrared ($\lambda \sim 11$ μm) quantum cascade lasers", Appl. Phys. Lett. **69**, 2810–2812 (1996).

[111] C. Gmachl, A. Tredicucci, D.L. Sivco, A.L. Hutchinson, F. Capasso, and A.Y. Cho, "Bidirectional semiconductor laser", Science **286**, 749–752 (1999).

[112] J. Faist, F. Capasso, C. Sirtori, D.L. Sivco, A.L. Hutchinson, M.S. Hybertsen, and A.Y. Cho, "Quantum cascade lasers without intersubband population inversion", Phys. Rev. Lett. **76**, 411–414 (1996).

[113] J. Faist, D. Hofstetter, M. Beck, T. Aellen, M. Rochat, and S. Blaser, "Bound-to-continuum and two-phonon resonance quantum cascade lasers for high duty cycle, high temperature operation", IEEE J. Quantum Electron. **38**, – (2002), in press.

[114] J. Faist, M. Beck, T. Aellen, and E. Gini, "Quantum cascade lasers based on a bound-to-continuum transition", Appl. Phys. Lett. **78**, 147–149 (2001).

[115] D. Hofstetter, M. Beck, T. Aellen, and J. Faist, "High-temperature operation of distributed feedback quantum-cascade lasers at 5.3 μm", Appl. Phys. Lett. **86**, 396–398 (2001).

[116] S.A. Ktitorov, G.S. Simin, and V.Ya. Sindalovskii, "Bragg reflections and the high-frequency conductivity of an electronic solid-state plasma", Fiz. tverd. Tela. **13**, 2230–2233 (1971).

[117] K. Unterrainer, B.J. Keay, M.C. Wanke, S.J. Allen, D. Leonard, G. Medeiros-Ribeiro, U. Bhattacharya, and M. Rodwell, "Inverse Bloch oscillator: strong terahertz-photocurrent resonances at the Bloch frequency", Phys. Rev. Lett. **76**, 2973–2976 (1996).

[118] H. Willenberg, J. Faist, and G.H. Döhler, 2001, private communication.

[119] W. Zawadzki, "Hybrid magneto-electric quantisation in quasi-two-dimensional systems", Semicond. Sci. Technol. **2**, 550–553 (1987).

[120] G. Belle, J.C. Maan, and G. Weimann, "Measurement of the miniband width in a superlattice with interband absorption in a magnetic field parallel to the layers", Solid State Commun. **56**, 65–68 (1985).

[121] A.P. Heberle, M. Oestreich, S. Haacke, W.W. Rühle, J.C. Maan, and K. Köhler, "Direct observation of resonant tunneling dynamics in high magnetic fields", Phys. Rev. Lett. **72**, 1522-1525 (1994).

[122] C. Gauer, A. Wixforth, J.P. Kotthaus, M. Kubisa, W. Zawadzki, B. Brar, and H. Kroemer, "Magnetic-field-induced spin-conserving and spin-flip intersubband transitions in InAs quantum wells", Phys. Rev. Lett. **74**, 2772–2775 (1995).

[123] V.M. Apalkov and T. Chakraborty, "Magnetic field induced luminescence spectra in a quantum cascade laser", Appl. Phys. Lett. **78**, 1973–1975 (2001).

[124] V.M. Apalkov and T. Chakraborty, "Influence of disorder and a parallel magnetic field on a quantum cascade laser", Appl. Phys. Lett. **78**, 697-699 (2001).

[125] T. Aellen, J. Faist, D. Hofstetter, A. Müller, and M. Beck, "Graded interface 9.3μm quantum cascade lasers", 31. IR-Kolloquium, Frauenhofer-Institut, Freiburg i. Br. (Germany), 2001.

[126] D. Hofstetter, J. Faist, M. Beck, A. Müller, and U. Oesterle, "Demonstration of high-performance 10.16 μm quantum cascade distributed feedback lasers fabricated without epitaxial regrowth", Appl. Phys. Lett. **75**, 665–667 (1999).

[127] C.F. Hsu, J.S. O, P.S. Zory, and D. Botez, "Intersubband laser design using a quantum box array", SPIE Proceedings **3001**, 271–281 (1997).

[128] S.J. Lee and J.B. Khurgin, "Novel quantum box intersubband lasing mechanism based on image charges", Appl. Phys. Lett. **69**, 1038–1040 (1996).

[129] C.Fu Hsu, J.Seok O, P. Zory, and D. Botez, "Intersubband quantum-box semiconductor lasers", IEEE J. Select. Topics Quantum Electron. **6**, 491–503 (2000).

[130] A. Kastalsky and A.L. Efros, "Magnetic field-induced suppression of acoustic phonon emission in a superlattice", J. Appl. Phys. **69**, 841–845 (1991).

[131] T. Berendschot, H. Reinen, H. Bluyssen, C. Harder, and H.P. Meier, "Wavelength and threshold current of a quantum well laser in a strong magnetic field", Appl. Phys. Lett. **54**, *1827-1829 (1989)*.

[132] A. Blank and S. Feng, "Suppression of intersubband nonradiative transitions by magnetic field in quantum well laser devices", J. Appl. Phys. **74**, 4795–4797 (1993).

[133] P. Hyldgaard and J.W. Wilkins, "Electron-electron scattering in far-infrared quantum cascade lasers", Phys. Rev. B **53**, 6889–6892 (1996).

[134] J. Ulrich, R. Zobl, K. Unterrainer, G. Strasser, and E. Gornik, "Magnetic-field-enhanced quantum-cascade emission", Appl. Phys. Lett. **76**, 19–21 (2000).

[135] B. Murdin, A. Hollingworth, M.Kamal-Saadi, R. Kotitschke, C. Ciesla, C. Pidgeon, P. Findlay, H. Pellemans, C. Langerak, A. Rowe, R. Stradling, and E. Gornik, "Suppression of LO phonon scattering in Landau quantized quantum dots", Phys. Rev. B **59**, 7817–7820 (1999).

[136] Y. Ji, Y. Chen, K. Luo, H. Zheng, Y. Li, C. Li, W. Cheng, and F. Yang, "Suppression of sequential tunneling current by a perpendicular magnetic field in a three-barrier, two-well heterostructure", Appl. Phys. Lett. **72**, 3309–3311 (1998).

[137] R. Ferreira, "Resonances in the hopping probability between flexible quantum dots: the case of superlattices under parallel electric and magnetic field", Phys. Rev. B **43**, 9336–9338 (1991).

[138] Y.Lyanda-Geller and J.P. Leburton, "Antiresonant hopping conductance and negative magnetoresistance in quantum-box superlattices", Phys. Rev. B **52**, 2779–2783 (1995).

[139] Y.Lyanda-Geller and J.P. Leburton, "Oscillatory level broadening in superlattice magnetotransport", Solid State Commun. **106**, 31–34 (1998).

[140] L. Canali, M. Lazzarino, L. Sorba, and F. Beltram, "Stark-cyclotron resonance in a semiconductor superlattice", Phys. Rev. Lett. **76**, 3618–3621 (1996).

[141] L. Canali, F. Beltram, M. Lazzarino, and L. Sorba, "High-field transport in superlattices: observation of the Stark-cyclotron resonance", Superlatt. Microstruct. **22**, 155–159 (1997).

[142] J. Liu, E. Gornik, S. Xu, and H. Zheng, "Sequential resonant tunneling through Landau levels in GaAs/AlAs superlattices", Semicond. Sci. Technol. **12**, 1422–1424 (1997).

[143] A. Tredicucci, C. Gmachl, M.C. Wanke, F. Capasso, A.L. Hutchinson, D.L. Sivco, S. Chu, and A.Y. Cho, "Surface plasmon quantum cascade lasers at $\lambda \sim 19\mu$m", Appl. Phys. Lett. **77**, 2286–2288 (2000).

[144] J. Ulrich, R. Zobl, N. Finger, K. Unterrainer, G. Strasser, and E. Gornik, "Terahertz-electroluminescence in a quantum cascade structure", Physica B **272**, 216–218 (1999).

[145] L. Ajili, "Emission dans l'infrarouge lointain et étude des transitions intersousbandes en présence d'un champ magnétique", Master's thesis, Université de Neuchâtel, 2001.

[146] C. Sirtori, 2001, private communication.

[147] D. Smirnov, O. Drachenko, J. Leotin, H. Page, C. Becker, C. Sirtori, V. Apalkov, and T. Chakraborty, "Intersubband magnetophonon resonances in quantum cascade structures", unpublished, 2001.

[148] C. Sirtori, F. Capasso, J. Faist, and S. Scandolo, "Nonparabolicity and a sum rule associated with bound-to-bound and bound-to-continuum intersubband transitions in quantum wells", Phys. Rev. B **50**, 8663–8674 (1994).

[149] D.F. Nelson, R.C. Miller, and D.A. Kleinman, "Band nonparabolicity effects in semiconductor quantum wells", Phys. Rev. B **35**, 7770–7773 (1987).

[150] C. Gmachl, F. Capasso, A. Tredicucci, D.L. Sivco, A.L. Hutchinson, and A.Y. Cho, "Long wavelength ($\lambda \simeq 13\mu m$) quantum cascade lasers", IEE Elect. Lett. **34**, 1103–1104 (1998).

[151] C. Gmachl, A. Tredicucci, F. Capasso, A.L. Hutchinson, D.L. Sivco, J.N. Baillargeon, and A.Y. Cho, "High-power $\lambda \sim 8$ μm quantum cascade laser with near optimum performance", Appl. Phys. Lett. **72**, 3130-3132 (1998).

[152] R. Köhler, C. Gmachl, A. Tredicucci, F. Capasso, D.L. Sivco, S. Chu, and A.Y. Cho, "Single-mode tunable pulsed, and continuous wave quantum-cascade distributed feedback lasers at $\lambda \sim 4.6$ - 4.7 μm", Appl. Phys. Lett. **76**, 1092–1094 (2000).

[153] S. Barbieri, C. Sirtori, H. Page, M. Beck, J. Faist, and J. Nagle, "Gain measurements on GaAs-based quantum cascade lasers using a two-section cavity technique", IEEE J. Quantum Electron. **36**, 736–741 (2000).

[154] W. Schrenk, N. Finger, S. Gianordoli, L. Hvozdara, G. Strasser, and E. Gornik, "GaAs/AlGaAs distributed feedback quantum cascade lasers", Appl. Phys. Lett. **76**, 253–255 (2000).

[155] J. Faist, F. Capasso, C. Sirtori, D.L. Sivco, A.L. Hutchinson, and A.Y. Cho, "Vertical transition quantum cascade laser with Bragg confined excited state", Appl. Phys. Lett. **66**, 538–540 (1995).

[156] C. Sirtori, J. Faist, F. Capasso, D.L. Sivco, A.L. Hutchinson, S. Chu, and A.Y. Cho, "Continuous wave operation of mid-infrared (7.4 - 8.6 μm) quantum cascade lasers up to 110K temperature", Appl. Phys. Lett. **68**, 1745–1747 (1996).

[157] C. Sirtori, J. Faist, F. Capasso, D.L. Sivco, A.L. Hutchinson, and A.Y. Cho, "Mid-infrared (8.5 μm) semiconductor lasers operating at room temperature", IEEE Photon. Technol. Lett. **9**, 294–296 (1997).

[158] G. Scamarcio, F. Capasso, C. Sirtori, J. Faist, A.L. Hutchinson, D.L. Sivco, and A.Y. Cho, "High-power infrared (8 - micrometer wavelength) superlattice lasers", Science **276**, 773–776 (1997).

[159] A. Tredicucci, F. Capasso, C. Gmachl, D.L. Sivco, A.L. Hutchinson, and A.Y. Cho, "High performance interminiband quantum cascade lasers with graded superlattices", Appl. Phys. Lett. **73**, 2101–2103 (1998).

[160] A. Tredicucci, F. Capasso, C. Gmachl, D.L. Sivco, A.L. Hutchinson, and A.Y. Cho, "High-performance quantum cascade lasers with electric-field-free undoped superlattice", IEEE Photon. Technol. Lett. **12**, 260–262 (2000).

[161] A. Tahraoui, A. Matlis, S. Slivken, J. Diaz, and M. Razeghi, "High-performance quantum cascade lasers ($\lambda \sim 11 \mu m$) operating at high temperature ($T \geq 425$ K)", Appl. Phys. Lett. **78**, 416–418 (2001).

[162] W. Schrenk, N. Finger, S. Gianordoli, E. Gornik, and G. Strasser, "Continuous-wave operation of distributed feedback AlAs/GaAs superlattice quantum-cascade lasers", Appl. Phys. Lett. **77**, 3328–3330 (2000).

Appendix A

Samples parameters

The layer sequence of one period of the different mid-infrared (Tables A.2 and A.1) and far-infrared (Tables A.4 and A.3) samples measured during this thesis are given in the following tables, starting from the injection barrier. Also indicated are the doping levels, the nominal sheet density n_s induced by this doping and the number of periods N_p. The doped layers are underlined and the thickness of the barriers are in bold. The details concernig the processing of the mid-infrared and far-infared structures are discussed in Sec. 3.5.1 and Sec. 3.5.2 respectively.

A.1 Mid-infrared samples

Sample	Layer sequence of one period, thickness in nm. AlGaAs barriers are in bold, n-doped layers are underlined.	n [cm^{-3}]	n_s [cm^{-2}]	N_p
S1543	**5.8**/1.5/**2.0**/4.9/**1.7**/4.0/**3.4**/3.2/**2.0**/2.8/<u>**2.3**/2.3/**2.5**/2.3/</u> **2.5**/2.1	$4 \cdot 10^{17}$	$3.76 \cdot 10^{11}$	36

Table A.1: Layer sequence of the mid-infrared sample based on GaAs/$Al_{0.33}Ga_{0.67}As$ material system.

Sample	Layer sequence of one period, thickness in nm. InAlAs barriers are in bold, n-doped layers are underlined.	n [cm^{-3}]	n_s [cm^{-2}]	N_p
D2065	6.8/4.8/3.5/2.3/1.9/2.2/2.2/2.1/2.1/2.0/2.0/1.8/1.8/ 1.7/2.0/1.6/2.2/1.6/2.4/1.4	$3 \cdot 10^{17}$	$3.8 \cdot 10^{11}$	25
D2075	6.8/4.8/2.8/3.9/2.7/2.2/2.2/2.1/2.1/2.0/2.0/1.8/1.8/ 1.7/2.0/1.6/2.2/1.6/2.4/1.4	$3 \cdot 10^{17}$	$3.8 \cdot 10^{11}$	25
D2122	5.0/0.9/1.5/4.7/2.2/4.0/3.0/2.3/2.3/2.2/2.2/2.0/2.0/ 2.0/2.3/1.9/2.8/1.9	$2 \cdot 10^{17}$	$1.24 \cdot 10^{11}$	25
D2160	5.0/0.9/1.5/4.7/2.2/4.0/3.0/2.3/2.3/2.2/2.2/2.0/2.0/ 2.0/2.3/1.9/2.8/1.9	$2 \cdot 10^{17}$	$1.24 \cdot 10^{11}$	25
S1384	3.5/4.4/3.3/3.5/2.3/2.6/2.2/2.0/2.0/2.0/2.5/1.8/2.7/1.9	$4 \cdot 10^{17}$	$3.52 \cdot 10^{11}$	35
S1390	3.2/2.5,3.0,2.5	$1 \cdot 10^{18}$	$3 \cdot 10^{11}$	120
S1397	4.2/3.1/0.9/6.4/1.0/6.0/2.8/3.9/1.0/3.8/1.2/3.7/1.5/ 3.9/1.7/4.0	$2.5 \cdot 10^{17}$	$2.55 \cdot 10^{11}$	35
S1548	2.5/7.4/2.5/5.5/2.5/4.6/2.4/4.2	$9.2 \cdot 10^{17}$	$2.3 \cdot 10^{11}$	50
S1672	2.5/7.4/2.5/5.5/2.5/4.6/2.4/4.2	$2 \cdot 10^{17}$	$5 \cdot 10^{10}$	50
S2007	2.4/4.8/2.3/3.8/3.1/3.1/2.8/2.9/	$7.4 \cdot 10^{17}$	$2.3 \cdot 10^{11}$	50

Table A.2: Layer sequence of mid-infrared samples based on $In_{0.53}Ga_{0.47}As/In_{0.52}Al_{0.48}As$ material system.

A.2 Far-infrared samples

Sample	Layer sequence of one period, thickness in nm. AlGaAs barriers are in bold, n-doped layers are underlined.	n [cm^{-3}]	n_s [cm^{-2}]	N_p
S1351	**3.0**/18.5/**3.5**/14.5/**3.5**/13.5	$3 \cdot 10^{16}$	$4.35 \cdot 10^{10}$	50
S1443	**3.0**/18.5/**3.5**/14.5/**3.5**/13.5	$6 \cdot 10^{15}$	$8.7 \cdot 10^{9}$	50
S1774	**6.0**/28.0/**2.5**/18.0/**4.0**/16.0/**2.5**/15.5	$2.4 \cdot 10^{16}$	$3.84 \cdot 10^{10}$	35
A2429	**3.1**/13.8/**3.8**/12.2/**3.6**/10.2/**4.2**/10.0/**4.1**/9.4	$2 \cdot 10^{16}$	$2 \cdot 10^{10}$	45
A2433	**4.0**/18.6/**0.8**/15.4/**0.6**/13.6/**2.3**/12.8/**1.8**/11.8/**2.3**/10.8/**3.2**/10.4	$1 \cdot 10^{16}$	$2.49 \cdot 10^{10}$	120

Table A.3: Layer sequence of far-infrared samples based on $GaAs/Al_{0.15}Ga_{0.85}As$ material system.

Sample	Layer sequence of one period, thickness in nm. InAlAs barriers are in bold, n-doped layers are underlined.	n [cm^{-3}]	n_s [cm^{-2}]	N_p
S1431	**3.5**/38.0/**1.4**/25.5/**2.3**/22.5/**1.4**/22.3	$5 \cdot 10^{15}$	$1.12 \cdot 10^{10}$	35

Table A.4: Layer sequence of the far-infrared sample based on $In_{0.53}Ga_{0.47}As/In_{0.52}Al_{0.48}As$ material system.

Appendix B

Electronic states in quantum heterostructures

B.1 Band structure calculations

The electronic states (more specifically the energy eigenvalues and the wavefunctions of the states) of the heterostuctures studied in this thesis were computed numerically in a two-band model. Unfortunately the parabolic approximation for the band structure is valid only at low energies, close to the relevant conduction band minimum. At higher energies the coupling, in particular to the valence band, plays an important role and the effective mass becomes energy-dependent: this is the non-parabolicity effect. To take into account the non-parabolicity, the standard theoretical approach considers the envelope-function Hamiltonian in the Kane approximation (with the in-plane wavevector $\vec{k}_\perp$ of the carrier being zero) [76]. In this formalism, one obtains a Schrödinger equation for the envelope function of the conduction band $\phi_c(z)$:

$$\left[P_z \frac{1}{2\mu(E,z)} P_z + E_c(z)\right] \phi_c(z) = E\phi_c(z) \tag{B.1.1}$$

with an energy- and position-dependent effective mass

$$\frac{1}{\mu(E,z)} = \frac{E_p}{3m_0}\left[\frac{2}{E - E_{lh}(z)} + \frac{1}{E - E_{so}(z)}\right] \tag{B.1.2}$$

where E_c, E_{lh} and E_{so} are respectively the conduction, light-hole and split-off position-dependent band energies, E_p is the Kane energy ($\sim$ 20eV in III-V semiconductors) and $P_z = -i\hbar\frac{\partial}{\partial z}$ is the momentum operator. One has to apply then the continuity at the interfaces of ϕ_c and of $\frac{1}{\mu(E,z)}\frac{\partial\phi_c}{\partial z}$ [76]. This three-band model can be simplified through a unitary transformation which allows one to replace light-hole and split-off bands with an *effective* valence band v [148], leading to an effective two-band model. In this case, the energy-dependent effective mass is given by

$$\frac{1}{\mu(E,z)} = \frac{1}{m_0}\left[\frac{E_p}{E - E_v(z)}\right] \quad . \tag{B.1.3}$$

The parameters $E_c - E_v$ and E_p are determined from the measured values of $m^* = \mu(E = E_c)$ of the material and from the non-parabolicity coefficient γ [149] defined as

$$\gamma^{-1} = 2m^*|E_c - E_v|/\hbar^2 \quad . \tag{B.1.4}$$

For typical InGaAs wells, with values of $m^* = 0.043m_0$ and $\gamma = 1.13\cdot10^{-14}$ cm^2, and InAlAs barriers with $m^* = 0.072m_0$, one obtains a Kane energy of $E_p = 18.3$ eV and an effective energy gap $|E_c - E_v| = 0.79$ eV.

This model predicts the correct energies with an accuracy of a few meV. The only problem is that the wavefunctions computed with this approach are not orthogonal, because one solves a one-band Schrödinger equation with an energy-dependent effective mass. So the dipole matrix element $z_{ij} = \left\langle \phi_c^{(i)} |Z| \phi_c^{(j)} \right\rangle$ between the state i and j is ill-defined. To overcome this problem, one has to use the two-band model and compute the dipole matrix element including the valence band. One obtains [148]

$$z_{ij} = \frac{\hbar}{2(E_j - E_i)}\left\langle \phi_c^{(i)} \left| P_z\frac{1}{m^*(E_i,z)} + \frac{1}{m^*(E_j,z)}P_z \right| \phi_c^{(j)} \right\rangle \quad . \tag{B.1.5}$$

The conduction band components $\phi_c^{(i)}$ and $\phi_c^{(j)}$ must then be normalized to account for the underlying valence band in such a way that

$$\left\langle \phi_c^{(i)} \left| 1 + \frac{E - E_c(z)}{E - E_v(z)} \right| \phi_c^{(j)} \right\rangle = 1 \quad . \tag{B.1.6}$$

The effect of the applied electric field on the heterostructure is taken into account in the program by dividing the potential in very thin steps and enclosing the whole structure in a large box. The doping is taken into account by a self-consistent calculation of Poisson's and Schrödinger's equations as described in Sec. 2.5.2.

B.2 Oscillator strength

Instead of a dipole matrix element, the optical transitions between states are commonly described in terms of a dimensionless oscillator strength f defined by

$$f_{ij} = \frac{2m_0}{\hbar^2}(E_j - E_i)\langle \phi_i \,|Z|\, \phi_j \rangle^2 = \frac{2m_0}{\hbar^2}(E_j - E_i) z_{ij}^2 \quad . \tag{B.2.7}$$

This definition of the oscillator strength allows the comparison with different systems, because it obeys the sum rule $\sum_j f_{ij} = 1$. For an infinite quantum well, the oscillator strength between the two first confined states is inversely proportional to the effective mass m^* and is $f_{12} = 0.96\frac{m_0}{m^*}$ [45]. One sees then the advantage of using a material with a small effective mass.

Appendix C

Population inversion engineering

C.1 Character of the transition

As mentioned in the text, there are many different ways to achieve a population inversion between subbands. In fact, we can distinguish the quantum cascade structures by the character of their 3-2 transition (see Fig. 2.3 b). The magnitude of the overlap between the two wave functions of states $n = 3$ and $n = 2$ can be strongly changed by design and the character of the transition changes then from *vertical* to *diagonal* (without taking into account the superlattice active regions). The advantages of a vertical transition (with the initial and final states centered in the same well) are its large oscillator strength between the two states involved in the transition and the fact that the broadening of the intersubband electroluminescence is relatively small. Nevertheless the main disadvantage is the short lifetime τ_{32}, where τ_{32}^{-1} is the non-radiative scattering rate from level 3 to level 2. As the population inversion condition is given by $\tau_{32} > \tau_2$, that leads to a unfavorable ratio of the lifetimes between the upper and lower states of the transitions. Furthermore this condition is less stringent than the condition $\tau_3 > \tau_2$ between the total lifetime of state 3 and 2, taking into account the non-radiative channel 3-1 which is non-negligible in such structures.

Let us now consider a three-quantum-well active region. In such a design, there is a thin well coupled to a thicker well in which the electronic transition takes place. This situation is schematically shown in Fig. C.1 b). As will be discussed in the next paragraph, the two lower states of the three-quantum well design are separated by one optical phonon energy. We refer to this design as *anticrossed* because the bound state of the thin well and the upper laser level are anti-crossed. Besides the good injection efficiency, the advantage of this approach is a higher upper state lifetime, however at the cost of a reduced oscillator strength between the two states. In the case of a purely diagonal transition, as shown in Fig. C.1 c), which was described in details in the Sec. 2.6 and Sec. 4.1 about the photon-assisted tunneling transition, the ground state of the thinner well lies between the two first states of the thicker well. By increasing the thickness of the coupling barrier, we can obtain an even larger population inversion, but again with a smaller oscillator strength. Fig. C.1 shows schematically the change of the transition character between a) vertical, b) anticrossed and c) diagonal.

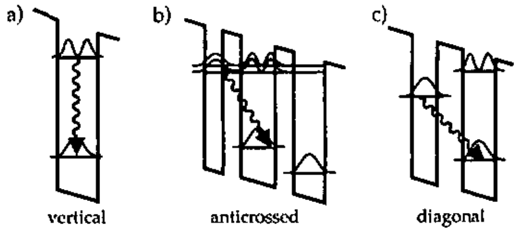

Figure C.1: Schemes of the change of the character of the transition between a) vertical, b) anticrossed and c) diagonal.

As mentioned in the text, the diagonal transitions are more sensitive to interface roughness than vertical ones and therefore have larger emission peaks. For the active region of a diagonal transition at about 10 μm (typically the structure S1548), the transition energy for an electric field of 55 kV/cm is 122.9 meV. By changing the thickness of the narrower well by one monolayer (about 3 Å), the transition energy changes to 112.8 meV (plus 3 Å) or 134 meV (minus 3 Å). That gives a broadening of the transition of about 21 meV. However, for a vertical transition in a quantum well of 10.5 nm and at the same energy, the broadening induced by the change of the thickness by also plus or minus 3 Å is only about 9 meV (between 118.3 and 127.2 meV).

The same calculations can be done in the far-infrared. There, the effect is less pronounced, for the wells are broader and the interface roughness plays therefore a less important role. We obtained a broadening of about 2.5 meV and 0.7 meV for diagonal and vertical transitions, respectively.

C.2 Optical phonon resonance-based population inversion

The first demonstration of quantum cascade laser has been performed with the so-called three-quantum well active region [1] using an optical phonon resonance between the two lowest states and the so-called anticrossed-transition between the upper laser state with the bound state of a thin adjacent well to maintain the population inversion, as schematically shown in Fig. C.3 a). This design has been studied in detail these last years in InGaAs/InAlAs material system [2, 150, 105, 151, 75, 126, 152, 115] as well in GaAs/AlGaAs material system [9, 153, 154, 10].

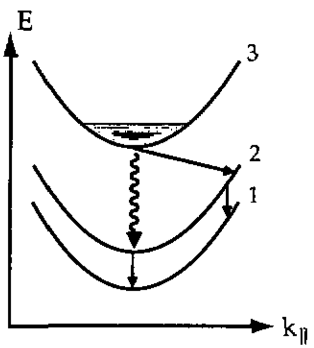

Figure C.2: Dispersion relation parallel to the layers of a three-level structure. The wavy arrow represents the radiative transition between states 3 and 2. The straight arrows represent the possible intersubband optical phonon processes. The energy separation between states 2 and 1 is equal to the optical phonon energy.

Quantum mechanically speaking, the discrete electronic states in quantum wells are created by the quantum confinement in the growth direction (usually labelled z-axis). However, these states have plane waves-like energy dispersion in the plane of the layers. Figure C.2 shows such a dispersion for a three-level structure. Under suitable applied bias, the energy separation between states $n = 1$ and $n = 2$ is then designed to be equal to the optical phonon energy (34 meV in InGaAs and 36 meV in GaAs) to maintain population inversion. In such a configuration the optical phonon scattering rate is enhanced (see Sec. 2.5.3) and the scattering time from level 2 is very short (on the order of 0.2 ps). In contrast, the scattering time of the optical phonon between states $n = 3$ and $n = 2$ is much longer due to the fact that this scattering is associated with a much larger wavevector transfer [110].

This extraction technique from the lower state of the transition based on optical phonon resonance was also used for active regions based on two quantum wells with a vertical transition [155, 156, 157], as schematically shown in Fig. C.3 b).

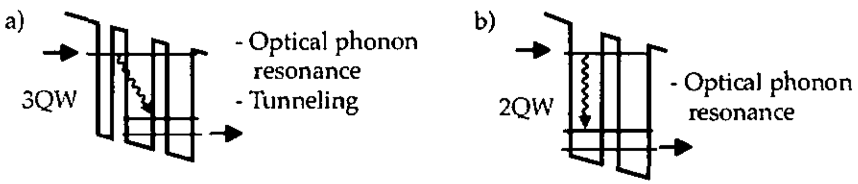

Figure C.3: a) Three quantum well and b) two quantum well active regions based on optical phonon resonance extraction of the lower state of the transition

C.3 Other lasing schemes

Nowadays several designs based on other active regions, without optical phonon resonance, have been demonstrated using the flexibility of intersubband transition engineering. These active regions were based on:

1. one quantum well, with the population inversion created by the tunneling from the ground state of the quantum well and by the non-parabolicity [112] (see Fig. C.4 a))

2. photon-assisted tunneling (*diagonal*) transition described in details in the text (see Fig. C.4 b))

3. interminiband transitions in a doped superlattice active region. In this case, the population inversion is automatically ensured because the electron lifetime at the top of the lower miniband ($\tau_1 \sim 0.1$ ps) is negligible with respect to the electron scattering time ($\tau_{21} \sim 10$ ps) by optical phonon emission from the bottom of the upper miniband to the lower miniband [158] (see Fig. C.4 c)).

4. chirped superlattices (superlattices of coupled quantum wells), without injector, with the population inversion also relied to phase space argument [159, 160, 161, 162, 4] (see Fig. C.4 d)).

All these designs have allowed to obtain laser action up to room temperature, except the single quantum well active region design.

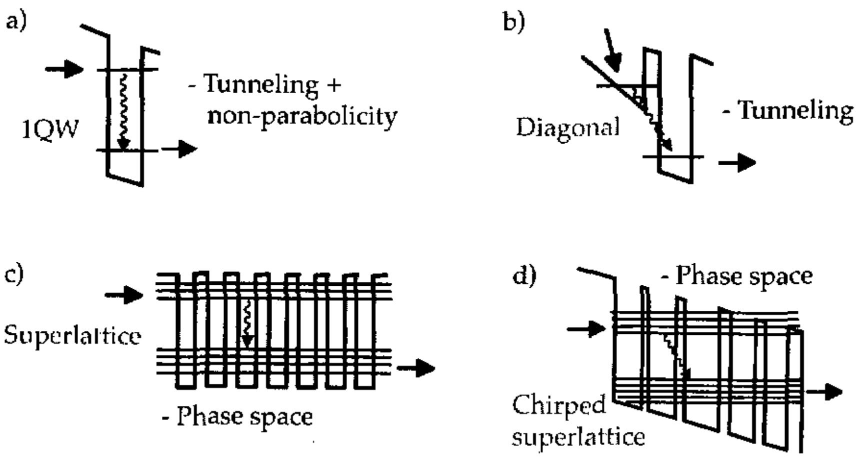

Figure C.4: Other active regions which have demonstrated laser action, without using optical phonon resonances. They are based on a) one quantum well, b) photon-assisted tunneling (diagonal) transition, c) doped superlattices and d) chirped superlattices active regions.

Appendix D

Properties of the InSb detector

The InSb detector used for far-infrared electroluminescence measurement is a photoconductive detector which operates absorbing far-infrared light at the cyclotron resonance frequency. These InSb detectors have been originally studied by Putley [92]. A review of Landau emission / detection can be found in [93].

Our detector is an off InSb hot electron bolometer type QFI/X provided by QMC Instruments Ltd [1]. The voltage-current characteristics at 3 K (temperature used during the measurements) are shown in Fig. D.1 for different applied magnetic fields between 0 and 2.52 T. The resistance of the InSb detector near zero bias is about 43 Ω at 0 T and about 30 kΩ at 2.52 T (maximum magnetic field reachable under warranty for our small coil). The resistance of the detector increases then quickly with increasing magnetic field. Comparing these values with the one at 4.2 K (about 35 Ω at 0 T and 5 kΩ at 2.52 T), the resistance of the detector increases therefore also with decreasing the temperature.

The detector works ideally in the curvature of its V-I characteristic. That is why we decided to use a battery as a current source with a serial resistance of $R = 10$ kΩ. Thus the current in the detector is about 150 μA at zero T and about 44 μA at 2.5 T, as shown by the dashed curve in Fig. D.1.

The intrinsic linewidth of the InSb detector is on the order of 2.8 meV, directly deduced by

[1]QMC Instruments Lts, Department of Physics, Queen Mary and Westfield College, mile End Road, London E1 4NS, UK.

measuring an intersubband terahertz laser [14]. Fig. D.2 shows such a laser spectrum with a lorentzian fit (grey curve) allowing to determine the full width at half maximum (FWHM) of the emission peak.

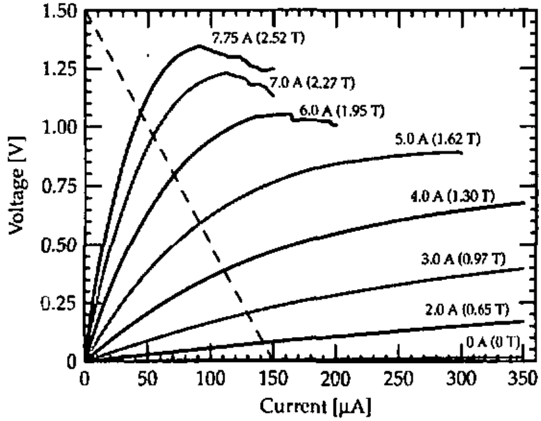

Figure D.1: V-I curves of the InSb detector at 3 K for different applied currents on the small coil between 0 and 7.75 A, corresponding to magnetic fields up to 2.52 T.

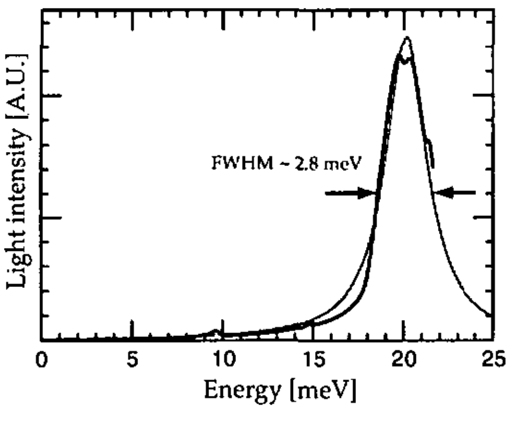

Figure D.2: Terahertz laser spectrum using the InSb detector for the determination of the linewidth of this detector. The grey curve is a lorentzian fit of the spectrum.

Published work

- J. Faist, A. Müller, M. Beck, D. Hofstetter, S. Blaser, U. Oesterle, and M. Ilegems, A quantum cascade laser based on a n-i-p-i superlattice, IEEE Photon. Technol. Lett. **12**, 263–265 (2000).
- M. Calame, S. Blaser, C. Leemann, and P. Martinoli, Dimensional crossover of the vortex matter in $YBa_2Cu_3O_7$ films, Physica B **284-288**, 891–892 (2000).
- S. Blaser, L. Diehl, M. Beck, and J. Faist, Long-wavelength ($\lambda \sim 10.5$ μm) quantum cascade lasers based on a photon-assisted tunneling transition in strong magnetic field, Physica E **7**, 33–36 (2000).
- S. Blaser, M. Rochat, M. Beck, J. Faist, and U. Oesterle, Far-infrared emission and Stark-cyclotron resonances in a quantum cascade structure based on photon-assisted tunneling transition, Phys. Rev. B **61**, 8369–8374 (2000).
- S. Blaser, D. Hofstetter, M. Beck, and J. Faist, Free-space optical data link using Peltier-cooled quantum cascade laser, IEE Elect. Lett. **37**, 778–780 (2001).
- S. Blaser, L. Diehl, M. Beck, J. Faist, U. Oesterle, J. Xu, S. Barbieri, and F. Beltram, Characterization and modeling of quantum cascade lasers based on photon-assisted tunneling transition, IEEE J. Quantum Electron. **37**, 448–455 (2001).
- S. Blaser, M. Rochat, L. Ajili, M. Beck, J. Faist, H. Beere, A. Davies, E. Linfield, and D. Ritchie, Terahertz interminiband emission and magneto-transport measurements from a quantum cascade chirped superlattice, Physica E **13**, 854–857 (2002).
- J. Faist, D. Hofstetter, M. Beck, T. Aellen, M. Rochat, and S. Blaser, "Bound-to-continuum and two-phonon resonance quantum cascade lasers for high duty cycle, high temperature operation", IEEE J. Quantum Electron. **38**, – (2002), in press.
- S. Blaser, M. Rochat, M. Beck, D. Hofstetter, and J. Faist, "Terahertz intersubband emission in strong magnetic fields", Appl. Phys. Lett. **81**, – (2002), in press.